

“(Na,K) Aluminosilicate Hollandites: Structures, Crystal Chemistry, and High-pressure Behaviour”

Von der Fakultät für Biologie, Chemie und Geowissenschaften der Universität Bayreuth

Zur Erlangung des akademischen Grades
Doctor der Naturwissenschaften
-Dr. rer. nat.-

genehmigte Dissertation

vorgelegt von

Jun Liu

Bayreuth, 2007

Table of contents

Summary	1
Zusammenfassung	5
1. Introduction	10
1.1 The importance of potassium and sodium in the deep Earth.....	10
1.1.1 Potassium-40 and the Earth's core.....	11
1.1.2 Importance of potassium and sodium in the lower mantle.....	11
1.2 K-Na aluminosilicate hollandite: possible host mineral for K and Na in the Earth's mantle.....	13
1.2.1 The hollandite structure.....	13
1.2.2 The (K,Na)AlSi ₃ O ₈ hollandite solid solution.....	15
1.2.3 The experimental stability field of (K,Na)AlSi ₃ O ₈ hollandite.....	16
1.2.4 The natural occurrence of (K, Na) aluminosilicate hollandite: hollandite in meteorites.....	18
1.3 Previous study.....	19
1.3.1 High-pressure study of the KAlSi ₃ O ₈ hollandite.....	19
1.3.2 Study of the KAlSi ₃ O ₈ - NaAlSi ₃ O ₈ hollandite solid solution.....	21
1.4 Aim of this research.....	23
2. Experimental techniques and sample characterization	24
2.1 Samples.....	24
2.1.1 Starting materials.....	24
2.1.2 Multi anvil technique.....	26
2.1.3. Characterisation of the run products.....	30
2.1.3.1 Chemical analysis.....	30
2.1.3.2 X-ray powder diffraction.....	32
2.1.3.3 X-ray single-crystal diffraction.....	33
2.2 High-pressure and high-temperature techniques.....	36

2.2.1 Diamond anvil cells.....	36
2.2.2 Raman experiments.....	39
2.2.3 High pressure X-ray powder diffraction experiments.....	40
2.2.3.1 High-pressure X-ray experiments at the BGI.....	40
2.2.3.2 Synchrotron radiation X-ray powder diffraction.....	41
3. Results	43
3.1 (K,Na)AlSi ₃ O ₈ hollandite solid solution.....	43
3.1.1 Chemical composition.....	43
3.1.2 X-ray powder diffraction.....	46
3.1.3 Raman spectra.....	50
3.1.4 Crystal structure.....	53
3.2 High pressure and high temperature behaviour of LiF.....	57
3.3 High pressure behaviour of Na ₂ K ₈ AlSi ₃ O ₈ hollandite in helium as pressure transmitting medium.....	58
3.3.1 Unit-cell lattice parameter determination at room T	58
3.3.2 Equation of state.....	63
3.3.2.1 The f - F plot.....	65
3.3.3 Spontaneous strain:.....	67
3.4 High pressure behaviour of K _{0.5} Na _{0.5} AlSi ₃ O ₈ hollandite in helium as pressure transmitting medium	72
3.4.1. The equation of state.....	73
3.5 High pressure behaviour of K _{0.8} Na _{0.2} AlSi ₃ O ₈ hollandite in lithium fluoride as pressure transmitting medium	73
3.5.1 The Equation of state.....	74
3.6 High pressure behaviour of K _{0.6} Na _{0.4} AlSi ₃ O ₈ hollandite in lithium fluoride as pressure transmitting medium	74
3.6.1 The Equation of state.....	76
3.7 High pressure high-temperature behaviour of K _{0.5} Na _{0.5} AlSi ₃ O ₈ hollandite in lithium fluoride as pressure transmitting medium.....	79
3.8 High pressure Raman experiments.....	84

3.8.1 High pressure Raman experiments of KAlSi_3O_8 hollandite in argon as pressure transmitting medium.....	84
3.8.2 High pressure Raman experiment of $\text{K}_{0.6}\text{Na}_{0.4}\text{AlSi}_3\text{O}_8$ hollandite in lithium fluoride as pressure transmitting medium	89
4. Discussion	93
4.1 The $(\text{Na},\text{K})\text{AlSi}_3\text{O}_8$ hollandite solid solution.....	93
4.1.1 Solid solution behaviour.....	93
4.1.2 The $\text{NaAlSi}_3\text{O}_8$ hollandite.....	95
4.1.3 The symmetry in $(\text{K},\text{Na})\text{AlSi}_3\text{O}_8$ hollandite: tetragonal vs. monoclini.....	96
4.2 High pressure and high temperature behaviour of $(\text{Na}, \text{K}) \text{h.}$	102
4.2.2 The Spontaneous strain behaviour of the tetragonal to monoclinic high-pressure phase transition in hollandite.....	103
4.2.2.1. Spontaneous strain behaviour under hydrostatic condition.....	103
4.2.2.2. Spontaneous strain behaviour in lithium fluoride.....	104
5. Conclusions	107
References	109
Appendix	127
Appendix 1: Indexed peaks in lattice parameter refinement.....	127
Appendix 2: Rietveld Refinement Patterns from high pressure experiment of $\text{K}_{0.8}\text{Na}_{0.2}\text{AlSi}_3\text{O}_8$ hollandite in helium.....	136
Erklärung	148

Acknowledgements

There are many people I wish to thank for their help and support. First of all, I want to thank Tiziana Boffa-Ballaran, the person I owe most to at Bayerisches Geoinstitut. I am so grateful to her, for all her help, suggestions and support, which made completion of this work possible. Tiziana, thank you so much! Both of my supervisors Tiziana and Leonid Dubrovinsky have been very supportive and very patient with me, and have given me the most help. I thank Leonid for all the helps, great suggestions, and all the work you have put into being my supervisor!

I thank Dan Frost for all his help in multi-anvil lab, and for giving me important suggestions and helps during my study. Thank you Florian Heidelbach for the help and effort you've done for my thesis. Thank you Fritz Seifert for all the kind help and support you've given me. Thank you Detlef Krausse and Anke Potzel for giving me lots of help in the probe lab, and Detlef also fixed all my computer problems. Thank you Stefan Keyssner for the help and making me feel at home here. Thank you Innokenty Kantor and Alexander Kurnosov for all your helps in Raman labs. I thank Ahmed El Goresy for all his help and suggestions. Thank you Nobuyoshi Miyajima for all the help. I thank Gerd Steinle-Neumann for all the help and knowledge I learned here!

I am also grateful to Andreas Audétat, Xin Nie, and Zhengning Tang for all your support and encouragement during the writing of this thesis. Thank you Ute Mann, Anastasia Kantor, Innokenty Kantor, and Ashima Saikia for all your helps during my study and during my writing of the thesis. And thank Enikő Bali, Gudmundur Gudfinnsson, Lora Armstrong, and Shantanu Keshav for being there and cheering me up!

Special thanks to our great Secretaries, Petra Buchert and Lydia Kison-Herzing for all the important help you've given me. Especially Petra, always so nicely and efficiently dealing with all kinds of my problems and requests, I would have been in much more trouble without your help!

The last and the most important one, I thank Mike Terry for all his help, suggestions, support, encouragement and everything else... This work was done for both you and me.

Vollständiger Abdruck der von der Fakultät für Biologie, Chemie und Geowissenschaften der Universität Bayreuth genehmigten Dissertation, zur Erlangung des akademischen Grades Doktors der Naturwissenschaften (Dr. Rer. Nat.).

Prüfungsausschuß:

Prof. S. Peiffer, Universität Bayreuth	(Vorsitzender)
PD. Dr. L. Dubrovinsky, Universität Bayreuth	(1. Gutachter)
Prof. F. Langenhorst, Universität Jena	(2. Gutachter)
Prof. D. Rubie, Universität Bayreuth	
Prof. J. Breu, Universität Bayreuth	

Datum der Einreichung der Dissertation:	23. Mai 2007
Datum des Wissenschaftlichen Kolloquiums:	23. Juli 2007

Summary

Aluminosilicates with the composition $(\text{Na,K})\text{AlSi}_3\text{O}_8$ and the dense hollandite-type structure, in which all Si and Al are in six-fold coordination, are considered as a possible repository of potassium and sodium in the Earth's mantle. Behaviour of Na and K in the deep mantle are of considerable interest from geophysical and geochemical points of view, because ^{40}K is one of the important heat sources during the evolution of the Earth, and alkali elements play an important role in stabilizing a variety of Al-rich phases in the lower mantle. In previous study of the phase relations in the system KAlSi_3O_8 - $\text{NaAlSi}_3\text{O}_8$, the maximum solubility of $\text{NaAlSi}_3\text{O}_8$ component into KAlSi_3O_8 hollandite-type structure was found to be 40 – 51 mol% (Yagi et al., 1994; Liu, 2006). For higher Na content the high-pressure phase appears to be that of the calcium-ferrite type structure. However, natural occurrences of $\text{NaAlSi}_3\text{O}_8$ hollandite have been reported in shock-induced melt veins of chondrite. In recent high-pressure studies of KAlSi_3O_8 hollandite, a phase transformation from tetragonal to monoclinic structure at about 20 GPa has been reported (Ferroir et al., 2006). Until now there has been no report on high-pressure behavior of mixed compositions in the system KAlSi_3O_8 - $\text{NaAlSi}_3\text{O}_8$. The aim of this research is to explore the phase relation of the K-Na system at different temperatures and pressures, and to determine the physical-chemical properties and high-pressure behaviour of silicate hollandite-type structures containing K and Na in different concentrations.

The $(\text{Na,K})\text{AlSi}_3\text{O}_8$ hollandite solid solution has been synthesised using multi-anvil apparatus in the pressure range between 13 and 26 GPa and temperatures between 1500 and 2200 °C, using $(\text{Na}_{0.0.6}, \text{K}_{1-0.4})\text{AlSi}_3\text{O}_8$ glasses, $\text{NaAlSi}_3\text{O}_8$ glass, and $\text{Na}_{0.75}\text{K}_{0.05}\text{Ca}_{0.1}\text{AlSi}_3\text{O}_8$ glass as starting materials. With increasing pressure, the solubility of Na component into the KAlSi_3O_8 hollandite end-member increases. Also by increasing temperature, the stability field of $(\text{Na,K})\text{AlSi}_3\text{O}_8$ hollandite becomes larger. Homogeneous assemblages with a pure hollandite phase (and maximum 1-2% of stishovite) were synthesized at temperature of 1700 °C and different pressures with 0%, 10%, 30%, 40%, 50% of $\text{NaAlSi}_3\text{O}_8$ component. Further pressure and temperature increases had no effect on increasing the Na solubility. No pure $\text{NaAlSi}_3\text{O}_8$ hollandite end-member was successfully synthesized. In experiments with $\text{Na}_{0.75}\text{K}_{0.05}\text{Ca}_{0.1}\text{AlSi}_3\text{O}_8$ glass as starting material used to simulate the composition of natural

occurring NaAlSi₃O₈ hollandite in shock induced melt veins in meteorites, a complex mixture of phases, among which a hollandite with composition K_{0.26}Na_{0.53}Ca_{0.16}Al_{1.15}Si_{2.86}O₈ was synthesized at 22 GPa and 1900 °C. Although the Na component in this hollandite is still not higher than 53 mol%, the ratio Na/(Na+K+Ca) = 0.56 is greater than the Na/(Na+K) ratio obtained from any other experiments performed in this study. Considering the difference in heat dissipation between the shock events in meteorites and the multi-anvil presses, it appears likely that NaAlSi₃O₈ hollandite forms as a result of local high pressure and high temperature conditions and really fast quenching under non-equilibrium conditions.

All synthesized hollandite samples have tetragonal *I4/m* symmetry at ambient conditions. The unit-cell volume and lattice parameters of the (Na,K)AlSi₃O₈ hollandite decreases linearly with increasing Na content. The *a* cell parameter decreases more rapidly than the *c* cell parameter, suggesting that changing the cation size in the tunnels of the hollandite structure affects more the *a* axis than the *c* axis, probably because the *c* axis length depends mostly on the cation to cation repulsion across the shared octahedral edges of the octahedral double chains, and only in a minor way on the size of the tunnel cations. Structural refinements of single-crystal data collected for KAlSi₃O₈ and K_{0.8}Na_{0.2}AlSi₃O₈ hollandites are consistent with Si and Al disorder among the octahedral sites. The major difference between the KAlSi₃O₈ hollandite end-member and the K_{0.8}Na_{0.2}AlSi₃O₈ sample is the presence in the latter of a split site away from the 4th-fold axis. This position, occupied by ~ 75% of the total Na content, is closer to the framework walls and has a very distorted coordination polyhedron with only 5 Na1-O bond distances between 2.4 and 2.6 Å whereas all other Na1-O bond distances are larger than 3 Å. The Si(Al)O₆ octahedra in KAlSi₃O₈ and K_{0.8}Na_{0.2}AlSi₃O₈ hollandite are more distorted with respect to those in stishovite, and the O1b-Si(Al)-O2b angle subtended by the shared horizontal edge is larger than the corresponding angle in stishovite, probably due to the substitution of Al³⁺ for Si⁴⁺.

The high pressure behaviour of hollandite samples with compositions of KAlSi₃O₈, K_{0.8}Na_{0.2}AlSi₃O₈, K_{0.6}Na_{0.4}AlSi₃O₈, and K_{0.5}Na_{0.5}AlSi₃O₈ have been studied using diamond anvil cells and different pressure transmitting media, by means of X-ray powder diffraction and Raman spectroscopy. High temperature behaviour of K_{0.5}Na_{0.5}AlSi₃O₈ hollandite at high

pressures has also been explored by means of X-ray powder diffraction. At high pressures, all tetragonal hollandite samples transform to a monoclinic (hollandite II) structure with space group $I2/m$. The transition pressure decreases with increasing Na component. Na substitution, thus, stabilizes the monoclinic phase, likely because the framework walls are more distorted than in the tetragonal phase and therefore more apt to accommodate the smaller Na atom. Second order Birch- Murnaghan equations of state were calculated for the tetragonal and monoclinic phases. The bulk moduli obtained for the tetragonal phases from fitting of the data collected using LiF as pressure transmitting medium are very large (up to values obtained for stishovite (Ross et al. 1990)). However, if only experiments using He as pressure transmitting medium are compared, it appears that Na has little effect on the bulk modulus value of the tetragonal aluminosilicate hollandite. Monoclinic hollandites are more compressible, and are stable up to the highest pressures reached during the experiments, suggesting that they may be possible host minerals for Na and K in transition zone and even down to the Earth's lower mantle, if continental crust is subducted to those depths. The high temperature and high pressure behaviour of $K_{0.5}Na_{0.5}AlSi_3O_8$ hollandite indicates qualitatively a positive Clapeyron slope for the tetragonal to monoclinic high-pressure transition. A simple extrapolation of a linear fit through the transition pressures of $KAlSi_3O_8$ and $K_{0.8}Na_{0.2}AlSi_3O_8$ hollandite indicates that the phase transition pressure of $NaAlSi_3O_8$ hollandite may be at ~ 7.5 GPa at room temperature.

The lattice strains associated with the tetragonal $I4/m$ to monoclinic $I2/m$ transition have been determined. The phase transition is proper ferroelastic with negligible volume strain. The symmetry breaking strains $e_1 - e_2 = \frac{a-b}{a_0}$ and $e_6 = \frac{a}{a_0} \cos \gamma$ are proportional to the order parameter Q associated with the transition and their squared values vary linearly with pressure indicating that the transition is second-order in character. The variation with pressure of the symmetry breaking strains is similar in $K_{0.8}Na_{0.2}AlSi_3O_8$ and $KAlSi_3O_8$ hollandites, suggesting that Na substitution mainly affects the transition pressure but not the transition mechanism.

Results from the high pressure experiments show that the tetragonal to monoclinic phase transition is very sensitive to deviatoric stresses present during the experiments due to the

pressure transmitting medium. Three different compounds: helium, argon and lithium fluoride were used as pressure transmitting media in this study. Helium seemed to provide ideal hydrostaticity and the tetragonal to monoclinic transition was quantitatively described following a second order Landau excess free-energy expansion. Argon has been reported to maintain quasi-hydrostaticity up to 9 GPa, and in high-pressure Raman experiments conducted on KAlSi_3O_8 hollandite end-member a change in slope of the vibrational modes was observed at about 15 GPa (~5 GPa lower than expected). Experiments using LiF have more stressed environments. The observed transition pressures (i.e. observation of splitting of diffraction lines indicating the transition to the monoclinic structure) in LiF are much lower than those observed in hydrostatic condition and are not consistent among different experiments. A stress term, hQ , added to the Landau excess free-energy expansion shows that, even for “mild” stresses created in a soft medium such as LiF, the monoclinic structure is stable at any pressure, preventing a quantitative characterization of the transition. These results might also give an indication of the possible effects arising from stresses on the mineral transitions in the Earth’s mantle.

Zusammenfassung

Aluminosilikate mit der Zusammensetzung $(\text{Na,K})\text{AlSi}_3\text{O}_8$ und der dichten Hollandit-Struktur, in der alle Si- und Al-Ionen sechsfach koordiniert auftreten, werden als mögliche Wirtsminerale für Kalium und Natrium im Erdmantel betrachtet. Das Verhalten von K und Na im tiefen Erdmantel ist von grossem geophysikalischem und geochemischem Interesse, da ^{40}K durch seinen radioaktiven Zerfall eine der wichtigen Wärmequellen während der Erdentwicklung darstellt, und da Alkalielemente generell eine wichtige Rolle bei der Stabilisierung verschiedener Al-reicher Phasen im unteren Erdmantel spielen. In einer vorhergehenden Arbeit über die Phasenbeziehungen im System $\text{NaAlSi}_3\text{O}_8$ - KAlSi_3O_8 wurde die maximale Löslichkeit der $\text{NaAlSi}_3\text{O}_8$ Komponente in der KAlSi_3O_8 Hollandit-Struktur mit 40 – 51 mol% bestimmt. Bei höheren Na-Gehalten scheint die Kalziumferritstruktur die Hochdruckphase zu bilden. In schock-induzierten Schmelzadern in chondritischen Meteoriten finden sich jedoch natürliche Vorkommen von $\text{NaAlSi}_3\text{O}_8$ Hollanditen. In neuen Hochdruckuntersuchungen von KAlSi_3O_8 Hollandit wurde ein Phasenübergang von der tetragonalen zur monoklinen Struktur bei ca. 20 GPa beobachtet. Bis jetzt gibt es aber keine Arbeit über das Verhalten der Mischreihe $\text{NaAlSi}_3\text{O}_8$ - KAlSi_3O_8 bei hohen Drucken. Das Ziel der vorliegenden Arbeit ist es daher, die Phasenbeziehungen im System $\text{NaAlSi}_3\text{O}_8$ - KAlSi_3O_8 bei unterschiedlichen Drucken und Temperaturen zu untersuchen, und die physikalisch-chemischen Eigenschaften sowie das Hochdruckverhalten von silikatischen Hollandit-Strukturen in Abhängigkeit von der Na- und K-Konzentration zu bestimmen.

Die $(\text{Na,K})\text{AlSi}_3\text{O}_8$ Hollandit-Mischkristallreihe wurde in einer Vielstempelpresse im Druck- und Temperaturbereich von 13 bis 26 GPa und 1500 bis 2200°C aus Gläsern der Zusammensetzungen $(\text{Na}_{0-0.6}, \text{K}_{1-0.4})\text{AlSi}_3\text{O}_8$, $\text{NaAlSi}_3\text{O}_8$ and $\text{Na}_{0.75}\text{K}_{0.05}\text{Ca}_{0.1}\text{AlSi}_3\text{O}_8$ synthetisiert. Mit ansteigenden Druck steigt die Löslichkeit der Na-Komponente in der KAlSi_3O_8 Hollandit-Struktur. Ebenso wird das Stabilitätsfeld von $(\text{Na,K})\text{AlSi}_3\text{O}_8$ mit ansteigender Temperatur grösser. Homogene Aggregate einer reinen Hollanditphase (mit maximal 1 bis 2% Stishovit) wurden bei einer Temperatur von 1700°C und unterschiedlichen Drucken mit 0, 10, 30, 40 und 50 mol% der $\text{NaAlSi}_3\text{O}_8$ Komponente erzeugt. Der maximale in der KAlSi_3O_8 Hollandit-Struktur gelöste Na-Gehalt betrug ~ 53 mol %. Weitere Druck- und Temperaturerhöhungen führten zu keiner Erhöhung der Na-Löslichkeit. Das reine $\text{NaAlSi}_3\text{O}_8$ -

Endglied mit der Hollandit-Struktur konnte nicht synthetisiert werden. Um die Zusammensetzung von natürlichen $\text{NaAlSi}_3\text{O}_8$ Hollanditen aus Schmelzadern in Chondriten zu simulieren, wurden Experimente mit $\text{Na}_{0.75}\text{K}_{0.05}\text{Ca}_{0.1}\text{AlSi}_3\text{O}_8$ Glas als Ausgangsmaterial bei 22 GPa und 1900°C durchgeführt, die ein Gemisch aus mehreren Phasen ergaben, unter denen sich auch Hollandite mit der Zusammensetzung $\text{K}_{0.26}\text{Na}_{0.53}\text{Ca}_{0.16}\text{Al}_{1.15}\text{Si}_{2.86}\text{O}_8$ befanden. Obwohl die Na-Komponente in diesem Hollandit nicht höher als 53 mol % ist, so ist doch das Verhältnis $\text{Na}/(\text{K}+\text{Ca}) = 1.3$ höher als in jedem anderen Experiment in der vorliegenden Untersuchung. Zieht man den unterschiedlichen Wärmeverlust in einem Vielstempelpressenexperiment und einem schock-induziertem Schmelzvorgang in einem Meteoriten in Betracht, so ist es wahrscheinlich, dass sich der $\text{NaAlSi}_3\text{O}_8$ Hollandit in Meteoriten bei lokal sehr hohen Drucken und Temperaturen sowie extrem schneller Abkühlung unter Ungleichgewichtsbedingungen bildet.

Alle synthetisierten Hollanditproben haben tetragonale $I4/m$ Symmetrie. Das Volumen und die Gitterparameter der Einheitszelle der $(\text{Na},\text{K})\text{AlSi}_3\text{O}_8$ Mischkristalle nehmen linear mit dem ansteigenden Na-Gehalt ab. Der Gitterparameter a nimmt stärker als der Gitterparameter c ab, was bedeutet, dass die sich ändernde durchschnittliche Kationengrösse in den Tunneln der Hollandit-Struktur die a Achse stärker als die c Achse beeinflusst. Die Länge der c Achse hängt mehr von der Abstossung der Kationen über die gemeinsamen Oktaederkanten der Oktaeder-Doppelketten ab, und weniger von der Grösse der Kationen in den Tunneln der Hollandit-Struktur. Strukturverfeinerungen von Einkristalldaten von KAlSi_3O_8 und $\text{K}_{0.8}\text{Na}_{0.2}\text{AlSi}_3\text{O}_8$ Hollandit sind konsistent mit einer ungeordneten Verteilung von Si und Al auf den verschiedenen Oktaederpositionen. Der Hauptunterschied zwischen der Struktur des KAlSi_3O_8 Endgliedes und der $\text{K}_{0.8}\text{Na}_{0.2}\text{AlSi}_3\text{O}_8$ Probe ist das Vorhandensein eines gesplitteten Gitterplatzes abseits der 4-fachen Rotationsachse in der Mischkristallprobe. Dieser Gitterplatz, der von ca. 75% des gesamten Na-Gehalts eingenommen wird, ist näher an den Wänden der Gerüststruktur und hat einen stark verformten Koordinationspolyeder mit nur 5 Na1-O Bindungsabständen zwischen 2.4 und 2.6 Å, während alle anderen Na1-O Bindungsabstände grösser als 3 Å sind. Die $\text{Si}(\text{Al})\text{O}_6$ Oktaeder in KAlSi_3O_8 und $\text{K}_{0.8}\text{Na}_{0.2}\text{AlSi}_3\text{O}_8$ Hollandit sind stärker verformt relativ zu denen in Stishovit, und der durch die gemeinsame horizontale Kante aufgespannte Winkel O1b-Si(Al)-O2b ist grösser als der korrespondierende Winkel in

der Stishovit-Struktur, was vermutlich durch die schwächere Kation-Kation Abstossung über die gemeinsame Kante durch den teilweisen Ersatz von Si^{4+} durch Al^{3+} in der Hollandit-Struktur verursacht wird.

Das Hochdruckverhalten der Hollanditproben mit den Zusammensetzungen KAlSi_3O_8 , $\text{K}_{0.8}\text{Na}_{0.2}\text{AlSi}_3\text{O}_8$, $\text{K}_{0.6}\text{Na}_{0.4}\text{AlSi}_3\text{O}_8$, und $\text{K}_{0.5}\text{Na}_{0.5}\text{AlSi}_3\text{O}_8$ wurde mithilfe von Röntgendiffraktometrie und Ramanspektroskopie in Diamantstempelpressen unter Verwendung verschiedener Druckmedien untersucht. Das Hochtemperaturverhalten von $\text{K}_{0.5}\text{Na}_{0.5}\text{AlSi}_3\text{O}_8$ wurde zusätzlich unter hohen Drucken mit Röntgendiffraktometrie charakterisiert. Bei hohen Drucken wandeln sich alle tetragonalen Hollandite in eine monokline Form mit der Raumgruppe $I2/m$ um (Hollandit II). Der Übergangsdruck vermindert sich mit ansteigendem Na-Gehalt. Die Substituierung von K durch Na stabilisiert daher die monokline Phase, was wahrscheinlich durch die stärker verformten Wände der Gerüststruktur in der monoklinen Phase erklärt werden kann, die die kleineren Na Ionen besser aufnehmen können. Die Birch-Murnaghan Zustandsgleichungen 2. Ordnung wurden für die tetragonalen und monoklinen Phasen berechnet. Die Kompressionsmodule, die für die tetragonalen Phasen aus Experimenten mit LiF als Druckmedium abgeleitet wurden, waren sehr hoch (bis zu Werten wie sie für Stishovit ermittelt wurden (Ross et al. (1990))). Wenn allerdings nur Experimente mit He als Druckmedium herangezogen werden, ergibt sich, dass Na nur einen kleinen Effekt auf den Kompressionsmodul der tetragonalen Hollandite hat. Monokline Hollandite sind am stärksten kompressibel, und sie sind bis zu den höchsten experimentell erreichten Drucken stabil, was sie zu möglichen Wirtsmineralen für K und Na bis zur Übergangszone des Erdmantels und sogar bis in den unteren Erdmantel macht, falls kontinentales Krustenmaterial bis in solche Tiefen subduziert wird. Das Hochtemperatur- und Hochdruckverhalten von $\text{K}_{0.5}\text{Na}_{0.5}\text{AlSi}_3\text{O}_8$ Hollandit folgt einer positiven Clapeyron-Steigung beim Übergang von der tetragonalen zur monoklinen Struktur. Eine einfache Extrapolation einer linearen Anpassung an die Übergangsdrucke von KAlSi_3O_8 und $\text{K}_{0.8}\text{Na}_{0.2}\text{AlSi}_3\text{O}_8$ Hollandit ergibt einen Phasenübergangsdruck von ca. 7.5 GPa für den reinen $\text{NaAlSi}_3\text{O}_8$ Hollandit bei Zimmertemperatur.

Die mit dem Phasenübergang von tetragonaler $I4/m$ zu monokliner $I2/m$ Symmetrie verbundenen Gitterdeformationen wurden quantitativ bestimmt. Der Phasenübergang ist ferroelastisch mit zu vernachlässigender volumetrischer Deformation. Die die Symmetrie brechenden Deformationen $e_1 - e_2 = \frac{a-b}{a_0}$ und $e_6 = \frac{a}{a_0} \cos \gamma$ sind proportional zum mit dem Übergang assoziierten Ordnungsparameter Q und ihre Quadrate ändern sich linear mit dem Druck, was typisch für einen Phasenübergang zweiter Ordnung ist. Die Änderung der Symmetrie brechenden Deformationen sind für $K_{0.8}Na_{0.2}AlSi_3O_8$ und $KAlSi_3O_8$ Hollandit sehr ähnlich, so dass die Na Substituierung offenbar hauptsächlich den Übergangsdruck beeinflusst, und nicht den Übergangsmechanismus.

Die Resultate der Hochdruckexperimente zeigen, dass der Phasenübergang von tetragonal nach monoklin sehr stark von deviatorischen Spannungen beeinflusst wird, die während des Experiments durch das Druckmedium erzeugt werden. Drei verschiedene Druckmedien - Helium, Argon und Lithiumfluorid - wurden in der vorliegenden Arbeit verwendet. Helium scheint ideale hydrostatische Druckverhältnisse in der Diamantstempelpresse zu liefern, und mithilfe dieser Experimente konnte der tetragonal-monokline Phasenübergang quantitativ mithilfe einer Landau Entwicklung zweiter Ordnung über die überschüssige freie Energie beschrieben werden. Argon erzeugt quasi-hydrostatische Bedingungen in Experimenten mit Diamantstempelpressen nur bis zu 9 GPa, und entsprechend wurde in mit Ramanspektroskopie kombinierten Hochdruckexperimenten mit $KAlSi_3O_8$ Hollandit eine Änderung des Gefälles der Vibrationsbanden schon bei ca. 15 GPa (~ 5 GPa niedriger als erwartet) beobachtet. In Experimenten mit LiF als Druckmedium treten die höchsten deviatorischen Spannungen auf. Die beobachteten Übergangsdrucke (d.h. das Auftreten von gespaltenen Beugungslinien, das das Erscheinen der monoklinen Phase signalisiert) in LiF sind deutlich niedriger als in hydrostatischen Druckmedien und sind nicht konsistent in verschiedenen Experimenten. Ein Spannungsterm, hQ , der in die Landau Entwicklung über die überschüssige freie Energie eingefügt werden kann, zeigt, dass selbst für geringe Spannungen, wie sie in einem weichen Medium wie LiF auftreten, die monokline Struktur über den gesamten Druckbereich stabil ist und so keine quantitative Charakterisierung des Phasenübergangs erfolgen kann. Die Resultate

dieser Experimente geben möglicherweise einen Hinweis darauf, welche Wirkungen deviatorische Spannungen auf Phasenübergänge im Erdmantel haben können.

1. Introduction

In geology textbooks it is normally assumed that continental crust cannot be subducted deeply into the Earth's mantle due to its low density ($\sim 2.7 \text{ g cm}^{-3}$) compared to the denser rock of the upper mantle ($\sim 3.4 \text{ g cm}^{-3}$) (e.g. Ringwood, 1991). The discovery of metamorphic rocks of continental affinities containing coesite, diamond, relics of former majoritic garnets (Chopin 1984; Smith, 1984, van Roermund et al., 2002; Perraki et al., 2006; Spengler et al., 2006; and references therein) suggested that these rocks were subjected to recrystallization at high-pressures and temperatures requiring a depth of more than 100 – 250 km. The occurrences of ultra-high pressure metamorphic (UHPM) rocks within continental collision zones corroborate the fact that light material of the continental crust, despite its buoyancy, has been subducted at least to the upper mantle, perhaps even to the mantle transition zone, and that some of it has been exhumed to the surface from those depths.

One of the most abundant minerals in the Earth's crust is the alkali feldspar in the system $\text{KAlSi}_3\text{O}_8 - \text{NaAlSi}_3\text{O}_8$ (Deer et al. 1966), which, if subducted to great depths, will transform to high-pressure isochemical phases or decompose to give other more stable high-pressure phases. Moreover, the behaviour of K in the deep mantle is of considerable interest from geophysical and geochemical points of view, because ^{40}K is considered one of the important heat sources during the evolution of the Earth. $(\text{Na}, \text{K})\text{AlSi}_3\text{O}_8$ aluminosilicate hollandite-type materials with their dense structure, in which all Si and Al are in six-fold coordination, are considered as a possible repository of potassium and sodium in the Earth's mantle. The aim of our research is to explore the phase relations of the K-Na system at different temperatures and pressures and to determine the physical-chemical properties and high-pressure and high temperature behaviour of aluminosilicate hollandite-type structures containing K and Na in different concentrations.

1.1 The importance of potassium and sodium in the deep Earth

1.1.1 Potassium-40 and the Earth's core

The possible host phases of potassium in the deep mantle have been of great interest to many scientists, since ^{40}K is important for heat generation in the Earth's interior and it has potentially large influence in thermal evolution of the Earth (Wasserburg *et al.*, 1964; Yukutake, 2000; Murthy *et al.*, 2003). The hypothesis that ^{40}K may be a significant radioactive heat source in the Earth's core was proposed on theoretical grounds (Lewis, 1971; Hall *et al.*, 1971) over three decades ago, and a recent study employing high-pressure and high-temperature experiments by Murthy *et al.* (2003) shows that potassium enters iron sulphide melts in a strongly temperature-dependent fashion and that ^{40}K can serve as a substantial heat source in the cores of Earth and Mars.

Potassium-40, which has a radioactive half-life of about 1.2 billion years, could be an important source of heat in the Earth's core but this has never been unambiguously confirmed in an experiment. Murthy *et al.* (2003) used an iron and iron-sulphur mixture to represent the Earth's core and potassium silicate glass to represent the mantle. They measured the partition coefficient - the concentration of potassium in the sulphur mix divided by its concentration in the silicate at temperatures and pressures approaching those found deep in the Earth's mantle. They found that the logarithm of the partition coefficient is inversely proportional to temperature. The results suggest that potassium-40 can move from the silicate 'mantle' to the iron-sulphur 'core' and that it would be possible for a high enough concentration of potassium-40 to build up in the core. They calculated a core potassium-40 content of between 60 and 130 ppm, which produces between 0.4 and 0.8 TW of heat. Estimates of the core-mantle boundary heat flux are between 8 and 10 TW, so the heat produced by potassium-40 could significantly contribute to the heat flux at the boundary. Recent studies have shown that the present level of heat flux would have been insufficient to sustain the Earth's magnetic field for the past 3.5 billion years. This 'extra' radioactive heat could thus have allowed the field to exist.

1.1.2 Importance of potassium and sodium in the lower mantle

Alkali and alkali-earth elements play an important role in stabilizing a variety of Al-rich phases in the lower mantle. The physical and chemical properties of possible (Na, K) bearing phases including hollandite need to be known, in order to constrain the dynamics and chemical evolution of subducting slabs in the Earth's lower mantle.

Recent information about the Earth's lower mantle obtained from seismic data and laboratory experiments at high pressure are consistent with the mineralogy of the lower mantle being simpler in composition than that of the crust and upper mantle, and consisting of (Mg, Fe)SiO₃-Al₂O₃ orthorhombic perovskite, CaSiO₃ cubic perovskite, and (Mg,Fe)O magnesiowüstite. No Al-rich phases, except for perovskite, are considered to exist in the main part of the lower mantle (Irifune 1994; Kesson *et al.* 1998). However, high-pressure laboratory experiments on constituent materials of subducting slabs (e.g., mid-ocean ridge basalts, continental crust and related minerals), together with petrographic information obtained from inclusions in diamond and xenoliths that originated in the lower mantle, indicate that various Al-rich phases can form under lower mantle conditions (Madon *et al.* 1989; Ahmed-Zaïd and Madon 1991; Irifune *et al.* 1991; Ahmed-Zaid and Madon 1995; Irifune *et al.* 1996; Gautron *et al.* 1997; Harris *et al.* 1997; Funamori *et al.* 1998; Kondo and Yagi 1998; Miyajima *et al.* 1999; Wang and Takahashi 1999; Collerson *et al.* 2000; Qguri *et al.* 2000).

No systematic interpretation, however, has yet been made on what controls the occurrence of such Al-rich phases which may contain alkali elements and therefore control the behaviour of sodium and potassium in the lower mantle (Akaogi 2000; Wang and Takahashi 2000; Gasparik *et al.* 2000). Thus, phase transformations in mid-ocean ridge basalts (MORB) containing Na and K are the key to clarify the behaviour of aluminum and alkali elements under conditions of the lower mantle. For example, the study reported by Miyajima *et al.* (2001) shows that the (Na, K)₂O-rich bulk compositions of MORB and continental crust stabilize Al-rich phases other than perovskite in order to maintain the mass balance of the bulk composition, among which K-Na aluminosilicate hollandite.

Given that the mineral composition of the Earth's lower mantle might be more complex than the simplified system based on a simple pyrolitic composition, it is clear that the physical and chemical properties of possible (Na, K) bearing phases, including hollandite, may also be important to determine the dynamics and chemical evolution of subducting slabs in the Earth's lower mantle.

1.2 K-Na aluminosilicate hollandite: possible host mineral for K and Na in the Earth's mantle

Hollandite-type aluminosilicates with all Si and Al in six-fold co-ordination are some of the few high-pressure dense structures consistent with the Earth's lower mantle conditions (Finger and Hazen, 1991). The large squared tunnels formed by four double chains of edge-sharing octahedra in the hollandite-type structure (Yamada et al., 1984) provide a possible site for geochemically important large elements such as K, Na, Ba, Sr and Pb (Ringwood et al. 1967; Reid and Ringwood 1969; Liu 1978; Downs et al. 1995). Moreover a high pressure study on KAlSi_3O_8 hollandite has shown that this structure is stable over a large range of pressures and temperature and can therefore be considered as a possible repository of large alkali elements in the Earth's lower mantle (Tutti et al. 2001).

The recent discoveries of natural (Na, K) AlSi_3O_8 hollandite-type structure in shocked melt veins of chondrite also supports the suggestion that these minerals are possible hosts of K and Na in the Earth's mantle (Mori 1990 and 1994; Gillet et al. 2000; Kimura et al. 2000; Langenhorst and Poirier, 2000; Tomioka et al. 2000; Xie et al. 2001; Kimura et al. 2003; Ohtani et al. 2004).

1.2.1 The hollandite structure

Hollandite-type materials have the general formula $\text{A}_{0-2}\text{B}_8\text{O}_{16}$. Their structure consists of double chains of edge-sharing BO_6 octahedra that are corner-sharing with other double chains to form a framework containing large tunnels. The octahedral sites are occupied by a combination of tetravalent and lower-charged B cations (i.e. Mn^{4+} , Ti^{4+} , Mn^{3+} , Al^{3+} , Fe^{3+} , Mg^{2+} etc.), whereas the tunnels are partially or totally filled with large monovalent or divalent A cations (i.e. Ba^{2+} , Sr^{2+} , Pb^{2+} , K^+). The lower-charged B cations (valence $< +4$) are essential to balance the positive charge of the A cations. In minerals with the hollandite structure the B cations are mainly Mn^{4+} or Ti^{4+} as the major B cation. These include criptomelane ($\text{K}_{2-x}\text{Mn}_8\text{O}_{16}$), hollandite ($\text{Ba}_{2-x}\text{Mn}_8\text{O}_{16}$), coronadite ($\text{Pb}_{2-x}\text{Mn}_8\text{O}_{16}$) and manjiroite ($\text{Na}_{2-x}\text{Mn}_8\text{O}_{16}$), and priderite ($(\text{K,Ba})_{2-x}(\text{Ti,Fe})_8\text{O}_{16}$). All these minerals present various cation substitutions and also there exist a large number of synthetic hollandite-type compounds having a variety of compositions. Hollandite-type structures can be tetragonal $I4/m$ or monoclinic $I2/m$. The hollandite-type structure of the high-pressure polymorph of KAlSi_3O_8 feldspar is tetragonal and has been characterise by means of powder and single-crystal X-ray diffraction (Yamada et al., 1984; Zhang et al., 1993). Si and Al are randomly distributed among the BO_6 octahedra.

The potassium atoms are accommodated in large ‘tunnels’ and are occupying the special position $4/m.$, and are surrounded by eight O1 atoms forming a tetragonally distorted cube with K-O of $\sim 2.80 \text{ \AA}$, and four O2 with K-O of $\sim 3.1 \text{ \AA}$ being at the corners of a square which bisects the cube. These K-O distances define the coordination state of K to be eight. The BO_6 octahedron are very distorted with one of the B-O bond distances very short (1.77 \AA), similar to the Si-O distance in stishovite (Baur and Khan, 1971), and with extremely short O-O distance of the shared edge.

The hollandite structure is very similar to the calcium ferrite structure, which is known to be a high-pressure form of NaAlGeO_4 and NaAlSiO_4 (Ringwood and Major, 1967; Reid et al. 1967; Liu, 1977; Yamada et al. 1983). Also the calcium ferrite structure consists of double chains of edge-sharing octahedra arranged to form tunnels, however the alkali position is at the centre of a triangular prism of six oxygens with one face narrower than the other two, and is coordinated by two more oxygens out of the centre of the two wider prism faces (Yamada et al., 1983). The tetragonally distorted cube coordination of the tunnel position in the hollandite structure appears, therefore, more apt to accommodate large cations such as K (Figure 1.1).

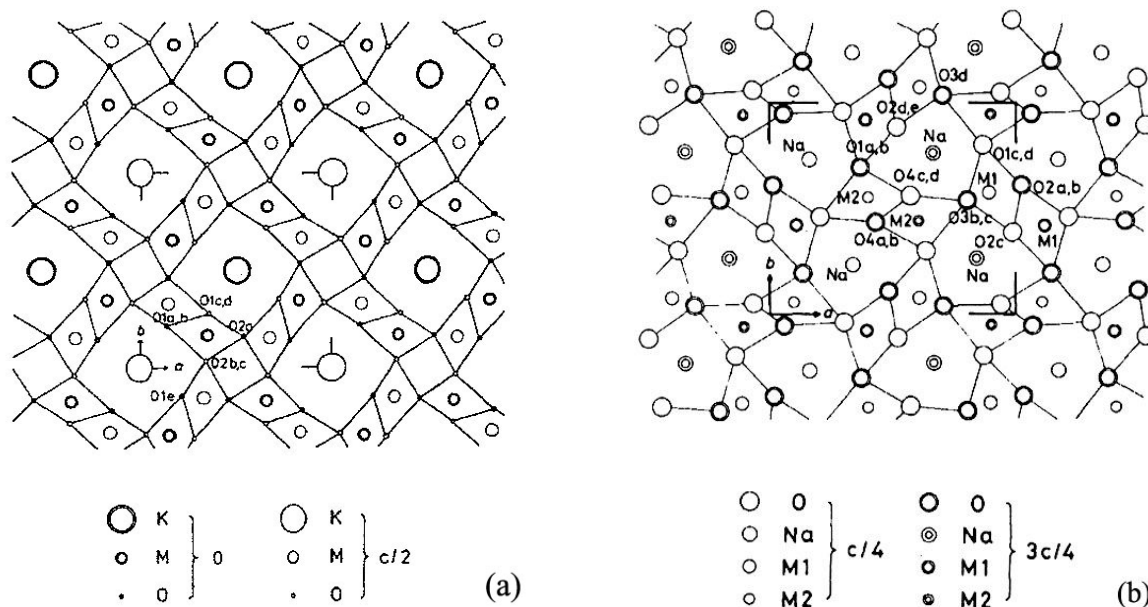


Figure 1.1. (a) Crystal structure of KAlSi_3O_8 with the hollandite structure projected on (001), showing square ‘tunnels’ occupied by K ions. (Yamada et al. 1984). (b) Crystal structure of NaAlSiO_4 with the CaFe_2O_4 structure projected on (001), showing triangular ‘tunnels’ occupied by Na ions, which are formed by four double chains.

1.2.2 The (K,Na)AlSi₃O₈ hollandite solid solution

At low pressures orthoclase KAlSi₃O₈ and albite NaAlSi₃O₈ form a solid solution (alkali feldspar) which is a major constituent mineral in the Earth's crust. At pressures from ~9 to ~26 GPa, KAlSi₃O₈ feldspar transforms to a high-pressure form with a hollandite structure. The NaAlSi₃O₈ hollandite has also been found in meteorites. Whether these two hollandite end members can form a complete solid solution is of great interest from both mineralogy and geochemistry points of view. As in the orthoclase-albite solid solution, the hollandite system involves cation mixing on a single large structural site. They both belong to the framework class of silicates. At high temperatures, there is complete solid solution between the feldspar end-members. In the KAlSi₃O₈ - NaAlSi₃O₈ hollandite system, it is also suggested that the amount of Na component dissolving into the K-hollandite structure increases with temperature (Liu, 2006). However, whether there exists a complete solid solution between the K and Na aluminosilicate hollandite end-members needs to be clarified.

The hollandite solid solution in the system KAlSi₃O₈ - NaAlSi₃O₈ may be an important candidate for the host phase of K as well as Na in the transition zone and the uppermost lower mantle. Previously the K-Na hollandite solid solution has been studied by a few researchers (Yagi et al., 1994; Liu, 2006), and they found that up to 40-51% Na component can be dissolved into the K- hollandite structure. Dobrzhinetskaya et al (2007) reported high-pressure and high-temperature experiments with ultra-high pressure (UHP) metamorphic rocks. They observed NaAlSi₃O₈ dissolving into KAlSi₃O₈ hollandite at 9-12 GPa and 1000-1300°C, and proposed that structure transformations of the UHP rock were accompanied by dissolution of Na-hollandite into K-hollandite. This study proved that the formation of K-Na hollandite solid solution can naturally occur during the subducting process in the Earth.

1.2.3 The experimental stability field of (K,Na)AlSi₃O₈ hollandite

The KAlSi₃O₈ hollandite

It has been reported that sanidine, KAlSi₃O₈, transforms to the KAlSi₃O₈ hollandite structure at high pressure. When KAlSi₃O₈ sanidine is subjected to high pressure, it first decomposes into a three-phase assemblage (wadeite-type K₂Si₄O₉ + Al₂SiO₅ kyanite + SiO₂ coesite) at 6-7

GPa and 700-1200 °C, and then recombines into a single phase of KAlSi_3O_8 hollandite at 9-10 GPa. Ringwood et al. (1967) first synthesized KAlSi_3O_8 with the hollandite structure by transformation of sanidine and breakdown of leucite at 12 GPa and 900 °C and proposed that the high-density hollandite form may exist at great depth in the transition zone of the Earth's mantle and could also be produced naturally by meteoric impact. Liu (1978) also reported the decomposition of kalsilite (KAlSiO_4) to a mixture of hollandite-type KAlSi_3O_8 plus KAlO_2 in the pressure range of 17-30 GPa. Kinimura et al. (1975), Yagi et al. (1994), and Urakawa et al. (1994) verified the phase relationships of K-feldspar and located the lower stability pressure of KAlSi_3O_8 hollandite at 8.5-10 GPa between 700-1200 °C. KAlSi_3O_8 hollandite may also recrystallize from the feldspar component of alkali minerals and rock assemblages at pressures and temperatures of the transition zone and lower mantle.

Faust and Knittle (1994) reported the breakdown of a natural muscovite at ~800 °C to KAlSi_3O_8 hollandite plus corundum and fluid at pressures greater than 11 GPa and its presence up to 20.5 GPa. KAlSi_3O_8 hollandite has also been observed as one of the reaction products of phengite and phengitic muscovite in K-bearing MORB, andesite, and pelitic systems at pressures between 8 to 11 GPa and temperatures between 750-1050 °C (Schmidt, 1996; Domanik and Holloway, 1996, 2000; Ono, 1998). Konzett and Fei (2000) reported the formation of K-hollandite close to stoichiometric KAlSi_3O_8 coexisting with CaSiO_3 perovskite at 20-23 GPa and 1300-1700 °C from the successive breakdown of phlogopite in sub- and per-alkaline systems. Irifune et al. (1994) reported the formation of KAlSi_3O_8 hollandite above 9 GPa in a hydrated average upper continental crust system and reported that at pressures above 16 GPa, the stability field of KAlSi_3O_8 hollandite greatly expands towards the liquidus. Wang and Takahashi (1999) reported the crystallization of KAlSi_3O_8 hollandite at pressures greater than 10 GPa at the expense of K-rich pyroxene dissolving into garnet, in a K-rich basaltic composition. Based on the refractory nature of potassium hollandite in the melting relationship at pressures higher than 20 GPa, they concluded that potassium is geochemically compatible at lower mantle conditions.

At depths below 100 km, Wendland and Eggler (1980) suggested that kalsilite (KAlSiO_4) is stable instead of sanidine (a higher-temperature form of orthoclase, KAlSi_3O_8) based on their study of the $\text{K}_2\text{O}-\text{Al}_2\text{O}_3-\text{SiO}_2$ system. On the other hand, Sommerville and Arhens (1980) argued that KAlSi_3O_8 hollandite is a more plausible potassic phase under mantle conditions

because Si and Al atoms are octahedrally coordinated and hence the hollandite structure has higher density. More recently, Langenhorst and Poirier (2000) reported KAlSi_3O_8 hollandite in meteorite, showing that KAlSi_3O_8 hollandite can actually exist under natural conditions.

Since the first synthesis of KAlSi_3O_8 hollandite, several studies have been made to clarify its stability field. Tutti et al. (2001) suggested that KAlSi_3O_8 hollandite is stable up to 95 GPa based on the results obtained from samples quenched from experiments in a diamond anvil cell. Most recently high-pressure in situ experiments discovered that at pressures above ~20 GPa KAlSi_3O_8 transforms to KAlSi_3O_8 hollandite-II phase with a monoclinic structure (Ferroir et al., 2006; Sueda et al., 2004). The KAlSi_3O_8 hollandite-II phase is reported to be more compressible and denser than the tetragonal phase, and might be stable under lower mantle conditions.

The $\text{NaAlSi}_3\text{O}_8$ hollandite

$\text{NaAlSi}_3\text{O}_8$ albite breaks down into $\text{NaAlSi}_2\text{O}_6$ jadeite plus quartz at 2-3 GPa (Birch and LeCome 1960). At higher pressure, Liu (1978) in his high pressure DAC study observed that jadeite and stishovite then recombine to form $\text{NaAlSi}_3\text{O}_8$ hollandite in the pressure range between 21-24 GPa. At pressures greater than 24 GPa, $\text{NaAlSi}_3\text{O}_8$ hollandite further decomposes to the calcium ferrite-type NaAlSiO_4 plus stishovite. However, in Liu's study no pure $\text{NaAlSi}_3\text{O}_8$ -hollandite was synthesized, and the identification of $\text{NaAlSi}_3\text{O}_8$ hollandite was complicated by its limited stability field, and by the fact that the X-ray pattern of this phase considerably overlapped those of jadeite and of calcium ferrite-type NaAlSiO_4 . He concluded that $\text{NaAlSi}_3\text{O}_8$ hollandite may be stable in a very limited pressure range near 20 GPa. Shock Hugoniot of alkali feldspars were also interpreted by transformation to the hollandite structure (Ahrens et al. 1969; Ahrens and Liu, 1973; Sekine and Ahrens, 1992).

In DAC experiments, a single phase of $\text{NaAlSi}_3\text{O}_8$ -hollandite has not been observed and it has always been found to co-exist with jadeite, stishovite and NaAlSiO_4 (NaScTiO_4 -type) (Liu, 1978). Pure $\text{NaAlSi}_3\text{O}_8$ -hollandite has not yet been synthesized using a multi-anvil press either.

The maximum solubility of $\text{NaAlSi}_3\text{O}_8$ -hollandite in KAlSi_3O_8 -hollandite was found to be limited to ~51% (Liu, 2006). This result appears inconsistent with the pure $\text{NaAlSi}_3\text{O}_8$ -

hollandite reported by Liu (1978) and the observation of the natural occurrence of $\text{NaAlSi}_3\text{O}_8$ -hollandite in many studies of meteorites reviewed in the next section. However, several studies suggest that a complete solid solution between $\text{NaAlSi}_3\text{O}_8$ -hollandite and KAlSi_3O_8 -hollandite might exist at high temperatures (Liu and El Goresy, 2007; Liu, 2006; Yagi et al., 1994).

1.2.4 The natural occurrence of (K, Na) aluminosilicate hollandite: hollandite in meteorites

Both KAlSi_3O_8 hollandite and $\text{NaAlSi}_3\text{O}_8$ hollandite have been discovered in melt veins of shocked meteorites. The natural occurrence of $\text{NaAlSi}_3\text{O}_8$ -rich hollandite (or Lingunite) was first reported by Mori (1990; 1994) in the Yamato-790729 L6 chondrite. Ever since, it has been discovered and unambiguously characterized in many L chondrites (Sixiangkou meteorite by Gillet et al. 2000; Tenham meteorite by Tomioka et al. 2000; Suizhou meteorite by Xie et al. 2001; Yamato-791384 by Ohtani et al. 2004) and H chondrites (Yamato-75100 by Kimura et al. 2000; Yamato-75267 by Kimura et al. 2003). Detailed chemical composition, X-ray data and Raman spectrum of a natural $\text{NaAlSi}_3\text{O}_8$ -hollandite were first reported by Gillet et al. (2000). Tomioka et al. (2000) also reported detailed chemical composition and electron diffraction data of a natural $\text{NaAlSi}_3\text{O}_8$ -hollandite. It has been estimated that the $\text{NaAlSi}_3\text{O}_8$ hollandite found in chondrite may have formed at pressures near 23 GPa and temperatures of $\sim 2000^\circ\text{C}$ (Gillet et al. 2000; Xie et al 2001).

The silicate hollandite rich in KAlSi_3O_8 , however, has been discovered only in Zagami achondrite by Langenhorst and Poirier (2000). This discovery of natural KAlSi_3O_8 hollandite in the melt vein of a shocked meteorite at estimated crystallization pressures below 23 GPa may have important implications for the existence of this mineral at depths of 400-660 km in the transition zone of the Earth's mantle. The high-pressure stability of KAlSi_3O_8 hollandite could, therefore, reveal the extent of its possible presence in the deeper parts of the Earth's interior (Tutti et al., 2001)

1.3 Previous study

1.3.1 High-pressure study of the KAlSi_3O_8 hollandite

The high pressure behaviour of KAlSi_3O_8 hollandite has been studied by several researchers. In previous studies of quenched experiments, it has been concluded that the stability of KAlSi_3O_8 hollandite extends up to 95 GPa implying that such a phase could be the host for potassium down to the lower mantle (Tutti et al., 2001). A previous *in situ* high-pressure single-crystal study of KAlSi_3O_8 hollandite has been performed up to pressures of 4 GPa, resulting in a high compressibility of the octahedral framework with respect to the related stishovite structure (Zhang et al., 1993). This suggests a possible phase transformation of the hollandite structure at higher pressure. In recent high-pressure studies of KAlSi_3O_8 hollandite by Sueda et al. (2004) and Ferroir et al. (2006), a phase transformation from tetragonal to monoclinic structure at about 20 GPa indeed has been observed. The results that are relevant for our study are described in some details in what follows.

In the study by Zhang et al (1993), a high-pressure single-crystal XRD study of KAlSi_3O_8 .with the tetragonal hollandite structure has been carried up to 4.47 GPa. The authors found that the a axis is approximately twice as compressible as the c axis, and the c/a ratio increases with pressure. This anisotropic compressibility is similar to that observed for the structurally related mineral stishovite, though KAlSi_3O_8 hollandite is approximately 53% more compressible along both axes. The relative incompressibility of the c axis can be explained by the strong cation to cation repulsive forces across the shared octahedral edge in the double chain; Si(Al)-O bonds perpendicular to c are more compressible than those in other directions. P - V data give an isothermal bulk modulus of 180(3) GPa using a Birch-Murnaghan equation of state with $K_T' = 4.0$ and constraint V_0 . The polyhedral bulk modulus of the Si(Al) O_6 octahedron is 153(9) GPa, the smallest observed among rutile-related oxides. The KO_8 tetragonal prism has a polyhedral bulk modulus of 181(43)GPa, which is unusually large for an alkali cation site. The volume of the K coordination polyhedron is constrained by the rigid tetragonal octahedral framework, so the bulk modulus is expected to be independent of the size and charge of the central cation.

In the study reported by Ferroir et al. (2006), the tetragonal hollandite structure (KAlSi_3O_8 hollandite) has been studied up to 32 GPa at room temperature using high-pressure *in-situ* powder X-ray diffraction techniques. A phase transition from the tetragonal $I4/m$ phase to a new phase was found to occur at about 20 GPa. This transition is reversible on release of pressure without noticeable hysteresis and hence this new high-pressure phase is unquenchable to ambient conditions. The volume change associated with the transition is found to be small (not measurable), suggesting a second order transition. The diffraction pattern of the high-pressure phase can be indexed in a monoclinic unit cell (space group $I2/m$), which is isostructural with $\text{BaMn}_8\text{O}_{16}$ hollandite. The γ angle of the monoclinic unit cell increases continuously above the transition. A Birch-Murnaghan equation of state fit to pressure-volume data obtained for the tetragonal KAlSi_3O_8 hollandite gave a bulk modulus $K_0 = 201.4$ (7) GPa with $K'_0 = 4.0$. This value is larger than the value (180(3) GPa) reported by Zhang et al. (1993), but considering the difference of the pressure range and the choice of V_0 in these two studies, these two results actually have very small differences. The hollandite-II structure was found to be more compressible compared to the extrapolated curve of tetragonal KAlSi_3O_8 . The compressibility of each axis of the unit cell did not differ significantly before and after the transition. Rather, it was the change of the angle γ that was related primarily to the rapid decrease in volume. The γ -angle started to deviate rapidly from 90° with the onset of the transition and it was still increasing even at about 30 GPa. However, the pressure range of these measurements (~ 30 GPa) was not enough to constrain the equation of state of hollandite-II but the author reports that the monoclinic phase became slightly denser than indicated by the simple extrapolation of the compression curve of KAlSi_3O_8 .

A high-pressure and high-temperature study on phase relations of KAlSi_3O_8 by Urakawa et al. (1994) shows that the melting point of hollandite-type KAlSi_3O_8 is between 1700°C and 1800°C at 11 GPa. Sueda et al. (2004) reported that the KAlSi_3O_8 -hollandite transformed to K-hollandite-II phase at ~ 22 GPa at room temperature and 35 GPa at 1200°C . Nishiyama et al. (2005) reported in-situ XRD measurements of KAlSi_3O_8 hollandite at pressures of 15-27 GPa and temperatures of 300-1800K. Fitting their P - V - T data with a Birch-Murnaghan equation of state these authors obtained $V_{300,0} = 237.6$ (2) \AA^3 , $K_{300,0} = 183$ (3) GPa, $(\partial K_{T,0}/\partial T)_P = -0.033$ (2) GPa, $a_0 = 3.32(5) \times 10^{-5} \text{ K}^{-1}$, and $b_0 = 1.09(1) \times 10^{-8} \text{ K}^{-2}$, assuming $K'_{300,0} = 4$. The broadening and splitting of diffraction peaks of KAlSi_3O_8 -hollandite was observed at 20-23 GPa and 300-1000

K as a result of phase transformation from tetragonal to monoclinic. They also determined the phase boundary to be $P \text{ (GPa)} = 16.6 + 0.007T \text{ (K)}$.

Neither the high-pressure and/or high-temperature behaviour of mixed compositions in the KAlSi_3O_8 - $\text{NaAlSi}_3\text{O}_8$ hollandite solid solution, nor the effect of Na on the compressibility behaviour of KAlSi_3O_8 have yet been studied.

1.3.2 Study of the KAlSi_3O_8 - $\text{NaAlSi}_3\text{O}_8$ hollandite solid solution

Phase relations in the system KAlSi_3O_8 - $\text{NaAlSi}_3\text{O}_8$ have been examined by Yagi et al. (1994) and Liu (2006), and the maximum solubility of the $\text{NaAlSi}_3\text{O}_8$ component into the KAlSi_3O_8 hollandite-type structure has been found to be about 40 – 51 mol%. At higher Na contents the stable high pressure phase appears to be that of the calcium-ferrite type structure. However, in the last few years there have been a number of reports of natural occurrences of $\text{NaAlSi}_3\text{O}_8$ hollandite in shock-induced melt veins of chondrite.

Yagi et al. (1994) studied the phase relations in the system KAlSi_3O_8 - $\text{NaAlSi}_3\text{O}_8$ at pressures of 5 - 23 GPa and temperatures of 700 – 1200 °C. He found that the maximum solubility of the $\text{NaAlSi}_3\text{O}_8$ component into the KAlSi_3O_8 hollandite-type structure at 1000 °C is about 40 mol%. Sanidine first dissociates into a mixture of wadeite-type $\text{K}_2\text{Si}_4\text{O}_9$, kyanite and coesite at 6-7 GPa, which further recombines into KAlSi_3O_8 hollandite at 9-10 GPa. In contrast, $\text{NaAlSi}_3\text{O}_8$ hollandite is not stable at 800-1200 °C, and the mixture of jadeite plus stishovite directly changes into an assemblage of calcium ferrite-type NaAlSiO_4 plus stishovite at pressures of ~ 23 GPa. Phase relations in the system KAlSi_3O_8 - $\text{NaAlSi}_3\text{O}_8$ at 1000 °C (Figure 1.2) show that the $\text{NaAlSi}_3\text{O}_8$ component gradually dissolves into KAlSi_3O_8 hollandite with increasing pressure. The maximum solubility of $\text{NaAlSi}_3\text{O}_8$ in hollandite at 1000 °C was about 40 mol% at 22.5 GPa, above which it decreases with pressure. The unit cell volume of the hollandite solid solution is reported to decrease only slightly with increasing $\text{NaAlSi}_3\text{O}_8$ content.

More recently Liu (2006) reported experiments performed from the starting composition of $(\text{K}_{0.2}\text{Na}_{0.8})\text{AlSi}_3\text{O}_8$ at 14-25 GPa and 1400-2400 °C using a multi-anvil press. In his

experiments the maximum $\text{NaAlSi}_3\text{O}_8$ content in KAlSi_3O_8 hollandite is ~ 51 mol% at ~ 22 GPa and 2200°C , and its fraction is positively correlated to temperature. He therefore concluded that the hollandite with ~ 90 mol% $\text{NaAlSi}_3\text{O}_8$ found in some meteorites is a disequilibrium product. However, this conclusion was drawn from the results of experiments with albite-orthoclase only, but ignored the possible influence of an anorthite content (15% in Sixiangkou, and 67% in Zagami).

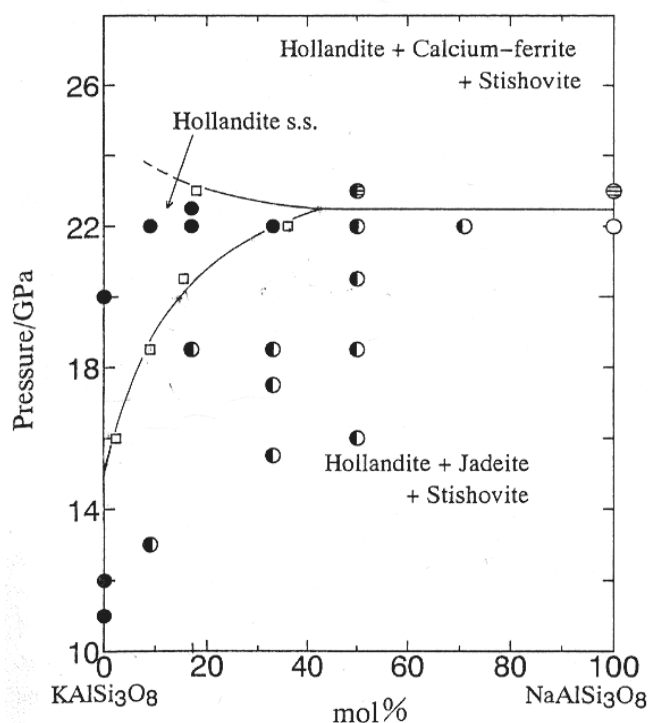


Figure 1.2. Phase relations in the system KAlSi_3O_8 - $\text{NaAlSi}_3\text{O}_8$ at 1000°C by Yagi et al. (1994). Circles represent experimental runs. Areas of different symbols in one circle correspond roughly to the volumes of the different phases (or assemblages). Small squares show the compositions of hollandite coexisting with jadeite (or calcium ferrite) plus stishovite.

1.4 Aim of this research

The basic aim of this research project is to explore the phase relation of the KAlSi_3O_8 - $\text{NaAlSi}_3\text{O}_8$ system at different temperatures and pressures, and to determine the physical-chemical properties and high-pressure and high temperature behaviour of the aluminosilicate

hollandite-type structures containing K and Na in different concentrations. Specifically, it is focused on the following points:

- (1) To determine the phase relations in the system KAlSi_3O_8 - $\text{NaAlSi}_3\text{O}_8$ in the pressure range 13-24 GPa and 1700 °C.
- (2) To investigate the stability field of the $\text{NaAlSi}_3\text{O}_8$ hollandite end-member in the pressure range 19-26 GPa and at temperatures higher than 1700 °C.
- (3) To study the mixing properties of the hollandite structure in the system KAlSi_3O_8 - $\text{NaAlSi}_3\text{O}_8$ both at the macroscopic and microscopic length scale by means of X-ray diffraction and Raman spectroscopy.
- (4) Synthesis experiments of single-crystals of mixed compositions for X-ray structural refinements, to provide information about the crystal chemistry of mixed compositions.
- (5) To study the mixed compositions by means of high-pressure X-ray diffraction and *in situ* Raman spectroscopy, to determine if Na, K substitution produces a variation in the bulk modulus and compressional behaviour of the KAlSi_3O_8 - $\text{NaAlSi}_3\text{O}_8$ solid solution.

2. Experimental techniques and sample characterization

2.1 Samples

2.1.1 Starting materials

Glasses with compositions of $K_xNa_{1-x}AlSi_3O_8$ ($x = 1, 0.9, 0.8, 0.7, 0.5, 0.4$) and $Na_{0.75}K_{0.05}Ca_{0.1}AlSi_3O_8$ were made for starting materials for the synthesis experiments. To make these glasses, mixtures of K_2CO_3 , Na_2CO_3 , $CaCO_3$ (this last compound was only used for the synthesis of $Na_{0.75}K_{0.05}Ca_{0.1}AlSi_3O_8$ glass), Al_2O_3 and SiO_2 powder with purity $>99.99\%$ were weighted in the opportune quantities and ground in an agate mortar, then slowly heated in a platinum crucible up to $1000^\circ C$ overnight for decarbonation. A list of details of the chemicals used is shown in Table 2.1. They were subsequently melted at temperatures between 1350 and $1650^\circ C$, depending on the amount of Na present since the melting temperature of the mixture decreases with increasing Na content. Then the melted mixture was immediately quenched by putting the platinum crucible into cool water. To avoid losing Na and K during melting, the melting time was very short. Each time the mixture was melted a maximum of 15 minutes, then crushed, ground and melted again. For each composition, this process was repeated for at least 5-6 times, in order to get clear and homogeneous glasses. When melted at very high temperature for a long time (e.g. for $KAlSi_3O_8$ composition), an additional 15 mol % K component was added into the mixture beforehand to compensate for a possible lost of K during melting. The glass compositions were analyzed using an electron microprobe. Glasses were also checked by means of Raman spectroscopy to make sure that no carbon component was still present. Details of the melting procedure and the glass compositions are given in Table 2.2. The starting material used for the experiments on the Na end-member hollandite was an albite glass with composition $NaAlSi_3O_8$ from Reid (2002).

The choice of glasses to use as starting materials was dictated by the fact that one could achieve a higher homogeneity of the synthesis products with respect those obtained by using the oxide mixture directly.

Table 2.1. Chemicals used.

Chemical	Purity grade	Company
K ₂ CO ₃	99.99%	Aldrich
Na ₂ CO ₃	99.999%	Aldrich
CaCO ₃	99.999%	Alfa
SiO ₂	99.995%	Alfa
Al ₂ O ₃	99.99%	Chemour

Table 2.2. Details of the preparation of the starting materials and their compositions

Nominal glass composition	Melting T (°C)	Melting time	Results from probe analysis (based on 8 oxygen)
KAlSi ₃ O ₈	1650	15 min for 5 times	K _{1.04} Al _{1.04} Si _{2.96} O ₈
K _{0.9} Na _{0.1} AlSi ₃ O ₈	1650	10 min for 5 times	K _{0.90} Na _{0.10} Al _{1.01} Si _{2.99} O ₈
K _{0.8} Na _{0.2} AlSi ₃ O ₈	1650	10 min for 5 times	K _{0.80} Na _{0.21} Al _{1.01} Si _{2.99} O ₈
K _{0.7} Na _{0.3} AlSi ₃ O ₈	1500	10 min for 5 times	K _{0.68} Na _{0.3} Al _{0.97} Si _{3.03} O ₈
K _{0.5} Na _{0.5} AlSi ₃ O ₈	1500	5 min for 6 times	K _{0.49} Na _{0.51} Al _{1.01} Si _{2.99} O ₈
K _{0.4} Na _{0.6} AlSi ₃ O ₈	1350	15 min for 5 times	K _{0.40} Na _{0.61} Al _{1.01} Si _{2.98} O ₈
Na _{0.75} K _{0.05} Ca _{0.1} AlSi ₃ O ₈	1450	5 min for 6 times	Na _{0.78} K _{0.05} Ca _{0.10} Al _{1.04} Si _{2.96} O ₈
NaAlSi ₃ O ₈	Albite glass (details of this glass is described by Reid (2002))		

For some compositions, non-glass starting materials were also prepared in order to test the possibility of growing larger crystals during the synthesis experiments. It is a general experience that relatively coarse-grained mixture with some carbon component which produces a fluid during the synthesis experiments might help crystal growing. In this case, mixtures of K₂CO₃, Na₂CO₃, Al₂O₃ and SiO₂ powder were ground and only slightly decarbonated at 800 °C for 3 hours before being used for the synthesis experiments. In this

way KAlSi_3O_8 and $\text{K}_{0.8}\text{Na}_{0.2}\text{AlSi}_3\text{O}_8$ hollandite with large grains (more than 100 microns) were obtained. For richer Na compositions, however, also this method for making large grains was not successful.

2.1.2 Multi anvil technique

The samples were synthesized with multi-anvil apparatuses in the pressure range between 13 and 26 GPa and temperatures between 1500 and 2200 °C. The principles of the multi-anvil apparatus are shown schematically in Figure 2.1. The force of a hydraulic press is exerted onto a set of 6 steel anvils that form a cubic gap filled with 8 tungsten carbide (WC) cubes. The corners of the WC cubes are truncated to form an octahedral pressure chamber, which is filled by an MgO octahedron containing the sample capsule. The multi-anvil technique is described in details in a number of publications (see for example Kawai and Endo, 1970; Kawai *et al.*, 1973; Spain and Paauwe, 1977; Graham, 1987; Ohtani *et al.*, 1987; Walker *et al.*, 1990; Liebermann and Wang, 1992; Rubie *et al.*, 1993; Rubie, 1999; Irifune, 2002).

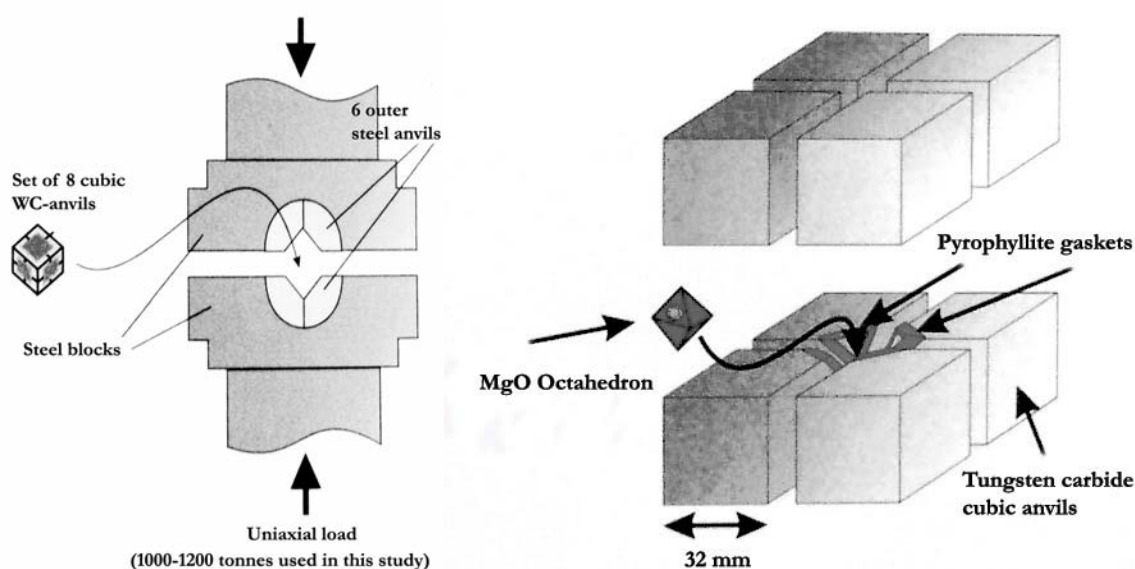


Figure 2.1. Details of the multi-anvil apparatus. Left: the two steel blocks enclosing six anvils forming a cubic cavity. Right: the eight WC cubes, from which the truncated corners form an octahedral void where sits the sample assembly.

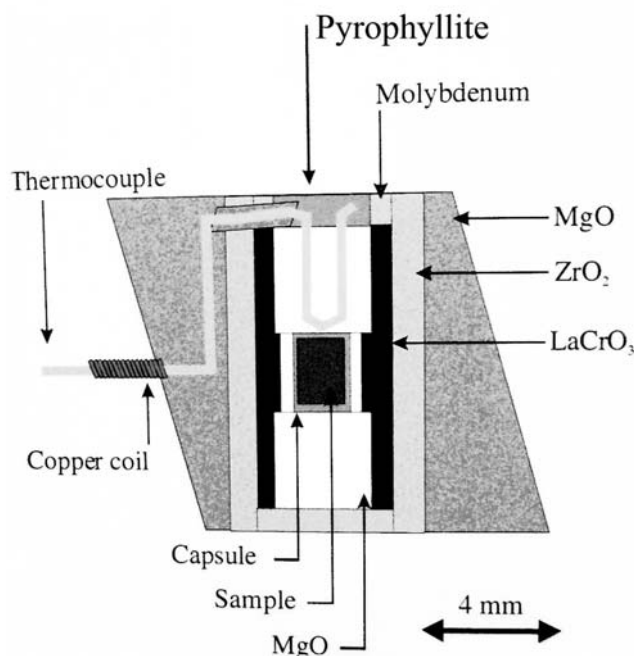


Figure 2.2. A schematic diagram of the 10/4 MgO octahedron assembly

The maximum pressure that can be reached in an experiment depends on the force applied, the edge length of the octahedron and the truncation edge of the cubes. WC cubes with truncation edge lengths (TEL) of 8, 5 and 4mm were used for experiments in three different pressure regions: 13-15; 15-20; and 20-26 GPa, respectively. The size of the sample assembly is determined by the octahedron edge length (OEL, in mm), and also decreases with increasing experimental pressure. In the following, the assemblies will be labeled according to the ratio OEL/TEL, that is: 14/8, 10/5, 10/4. A schematic diagram of the 10/4 assembly is shown in Figure 2.2. The octahedron is made of MgO doped with 5% Cr_2O_3 to reduce heat loss by radiation. A zirconia sleeve insulates the cylindrical LaCrO_3 resistance heater from the octahedron. Similarly, an MgO sleeve insulates the sample capsule from the heater to avoid chromium contamination from the furnace. The sample temperature is monitored using a W75%Re25%-W97%Re3% thermocouple inserted axially into the octahedral assembly, with the hot junction in contact with the capsule. The capsule is placed between two alumina spacer at the middle of the furnace in order to minimize the thermal gradients along the sample

charge. Re foil was used to make the sample capsules. The capsule sizes depend on the assembly used, for the 14/8 assembly is 1.6 mm in diameter and 2.7 mm long; for the 10/5 assembly is 1.6 mm in diameter and 1.8 mm long; and for the 10/4 assembly is 1.2 mm in diameter and 1.2 mm long. Pressures are calibrated using known phase transitions of common minerals. For instance, for the 10/4 assembly, the pressure is calibrated with respect to the phase transitions in the Mg_2SiO_4 system at 1600°C (Fei et al., 1990). The uncertainty of pressure calibration is ~ 1 GPa. The thermal gradient along the capsule at 1600 °C and 10 GPa is ± 50 °C for the 10/5 and the 10/4 assemblies (Canil, 1994; Walter et al. 1995), and 170 °C/mm at 24 GPa and 1650 °C for the 10/4 assembly (Bolfan-Casanova, 2000). In the case of the 14/8 assembly which is larger, and whose furnace is stepped and thicker in the middle (where the sample capsule is placed), the thermal gradient is thought to be much smaller.

In this study, two multi-anvil apparatuses at the Bayerisches Geoinstitut with axial forces of 1000 t and 1200 t were used: a 1000 t 1-Cylinder Hymag Press and a 1200 t 1-Cylinder Sumitomo Press. In all experiments the samples were first compressed to the required pressure and then the temperature was increased to the opportune value at the rate of ~ 100 °C/min. Samples were kept under the desired temperature for 2 hours. Only for temperatures above 1900°C, due to the temperature instability the heating time was reduced to 15-30 minutes. Quenching was achieved by switching off the power and the quench rate is of the order of 1000 °C/s. Automatic decompression was started after quenching and lasted for 15 to 18 hours. Details of the synthesis experiments are given in Table 2.3.

Table 2.3. Details of the synthesis experiments.

Run number *	Starting material	Pressure (GPa)	Temperature (°C)	Type of assembly	Heating time
S3436	KAlSi ₃ O ₈	13	1700	14/8	2h
S3356	KAlSi ₃ O ₈ **	13	1500	14/8	2h
S3600	K _{0.9} Na _{0.1} AlSi ₃ O ₈	15	1700	14/8	2h
S3439	K _{0.7} Na _{0.3} AlSi ₃ O ₈	13	1700	14/8	2h
S3442	K _{0.7} Na _{0.3} AlSi ₃ O ₈	15	1700	14/8	2h
H2216	K _{0.7} Na _{0.3} AlSi ₃ O ₈	17	1700	10/5	2h
S3461	K _{0.7} Na _{0.3} AlSi ₃ O ₈	20	1700	10/5	2h
H2229	K _{0.7} Na _{0.3} AlSi ₃ O ₈	20	1700	10/5	2h
S3524	K _{0.5} Na _{0.5} AlSi ₃ O ₈	20	1700	10/5	2h
H2305	K _{0.5} Na _{0.5} AlSi ₃ O ₈	22	1700	10/4	2h
H2502	K _{0.5} Na _{0.5} AlSi ₃ O ₈	22	1700	10/4	2h
S3598	K _{0.4} Na _{0.6} AlSi ₃ O ₈	22	1700	10/4	2h
H2495	K _{0.8} Na _{0.2} AlSi ₃ O ₈ **	20	1700	10/5	2h
H2353	K _{0.5} Na _{0.5} AlSi ₃ O ₈ **	22	1700	10/4	2h
S3726	Na _{0.75} K _{0.05} Ca _{0.1} AlSi ₃ O ₈	22	1900	10/4	30 m
S3785	Na _{0.75} K _{0.05} Ca _{0.1} AlSi ₃ O ₈	26	2200	10/4	15 m
S3445	NaAlSi ₃ O ₈	20	1700	10/5	2h
H2116	NaAlSi ₃ O ₈	21	1700	10/4	2h
H2306	NaAlSi ₃ O ₈	22.5	1700	10/4	2h

* Letters 'H' and 'S' reported together with the run numbers indicate the multi-anvil press used.

** Starting materials were oxide mixtures instead of glasses.

2.1.3. Characterisation of the run products

The recovered capsules from the synthesis experiments were cut lengthwise into two pieces using a diamond wire of 80 μm diameter. Half of the capsule was polished and prepared for Scanning electron microscopy (SEM) and electron microprobe analysis (EPMA) to determine the homogeneity of the sample, the number of phases present and their chemical compositions. The other half was ground and analyzed by X-ray powder diffraction.

2.1.3.1 Chemical analysis

Scanning electron microscopy (SEM)

A scanning electron microscope (SEM) was used to verify the homogeneity of the synthesized samples and obtain a qualitative chemical composition of the phases present. In the SEM, a focused electron beam with energy between 0.2 and 30 keV is scanned over the surface of the sample. The signal produced by the interaction of the electron beam and the sample is detected synchronous to the scanning process and displayed by modulation of a cathode-ray tube (CRT), i.e. in form of a virtual image. Depending on signal and material a resolution of 1 μm can be reached. Depending on the interaction between electron beam and specimen a number of different signals are generated, and three of them were used in this study: backscattered electrons (BSE), secondary electrons (SE) and X-ray fluorescence (XRF).

Backscattered electrons (BSE) are electrons that are scattered once or more off the atoms inside the specimen and have afterwards re-exited its surface. The energy distribution of the BSE has a peak close to the primary energy of the electron beam, which is due to electrons that have been backscattered (almost) elastically. These electrons dominate the BSE signal and their intensity is strongly dependent on the average atomic number (Z-contrast) and the crystal orientation (channeling contrast). BSE images can be used, therefore, to visualize the distribution of different chemical phases in the sample. The BSE image obtained for an homogeneous run product obtained at 13 GPa and 1700 °C from a glass starting material with composition $\text{K}_{0.7}\text{Na}_{0.3}\text{AlSi}_3\text{O}_8$ is shown in Figure 2.3 as an example.

The secondary electrons (SE) are situated on the low end of the energy spectrum (<50eV). They may be electrons of the primary beam that have lost large amounts of energy due to

inelastic collisions or electrons that originate from the sample itself (interaction with BSE). Due to their low energy only the electrons from near the surface can escape out of the sample, therefore the SE signal is ideally suited for imaging surface structures. The contrast in the image is determined by the sample morphology.

X-ray fluorescence (XRF) is generated by interaction of the primary beam with the atoms. The electron beam impinging on the specimen surface causes some temporary changes in the electronic structure of the atoms, i.e. electrons may jump into a different shell and then fall back into their original shell emitting characteristic X-rays. The X-rays can be recorded with energy- or wavelength-dispersive detectors (EDS or WDS) and the chemistry of the sample can be analyzed. EDS detectors are usually rather rapid, but have an inferior energy resolution compared to WDS detectors, which are used as standard tools in microprobes. The energy dispersive X-ray spectroscopy (EDX) can provide rapid qualitative, or with adequate standards, quantitative analysis of element composition with a sampling depth of 1-2 microns (Adams *et al.*, 1993; Reimer, 1998).

In the present work, SEM analysis was carried out with a SEM LEO Gemini 1530 with a Schottky emitter, using EBSD technique and EDX analysis. The results obtained are presented in the next chapter.

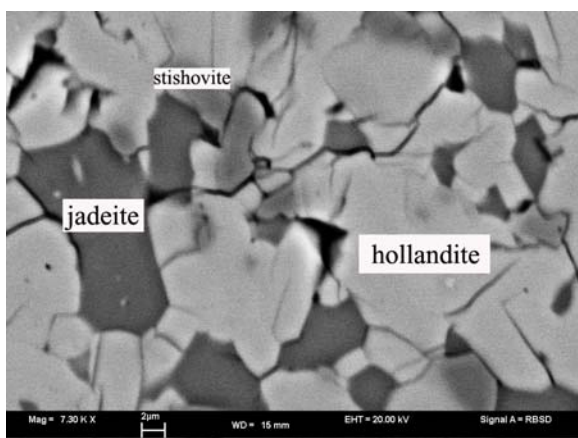


Figure 2.3. Typical BSE image of a non-homogeneous synthesis run product. At 13 GPa 1700 °C, the sample synthesized from $K_{0.7}Na_{0.3}AlSi_3O_8$ glass consists of three phases: a hollandite phase richer in K, stishovite and jadeite. The light grey regions are K-Na hollandite, the darkest regions are jadeite, the intermediate dark cloud-looking phase is stishovite.

Electron microprobe analysis (EPMA)

In this work, quantitative chemical analysis of the glass starting materials and of synthesis run products were determined by means of a JEOL 8200 microprobe, operating at an acceleration voltage of 15 kv and a beam current of 15 nA and in wavelength dispersive mode. Single crystals of andradite, spinel, albite and orthoclase were used as standards for Si, Al, Na and K, respectively. The electron beam size was defocused and about 10 μm for the analysis of the glasses, whereas was 1-2 μm for the analysis of the run products. The crystals of the hollandite phases present in the run products were large enough to be analyzed separately (between 20 to more than 100 μm). For each sample, more than 100 data points were collected. The results obtained for the glass starting materials are reported in Table 2.2. Whereas the results and uncertainties of the hollandite samples are presented in the next chapter.

2.1.3.2 X-ray powder diffraction

X-ray crystallography has historically been the primary tool used to investigate the structure of crystal matter, and the atomic and crystal structures of most materials have been determined using these techniques.

The direction in which X-rays are diffracted from a crystalline material is governed by Bragg's equation:

$$\lambda = 2d \sin \theta,$$

where λ is the wavelength of the radiation, d is the spacing between successive parallel planes that together pass through all of the lattice points in the crystal, and θ is the *Bragg angle*. It is the glancing angle of incident and reflection on the lattice planes of spacing d of the X-rays; the equation is thus written in terms of reflection of X-rays from the lattice planes. The angle 2θ is the angle between the forward direction of the undiffracted incident beam and the diffracted beam.

The measured intensities of the diffracted beams are determined by the arrangement of the atoms within a single unit-cell of the crystal, together with instrumental factors. Since the spacings of the lattice planes are dependent upon the unit-cell parameters of the crystal, the set of *d-spacings* and therefore the set of θ values for a particular X-ray wavelength λ (often reported as 2θ values) are characteristic of a given crystal structure. Together with the relative intensities of the diffraction maxima, they can be used to uniquely identify a crystalline compound.

In this study, all samples synthesized were characterized by means of X-ray powder diffraction. This was done with a Stoe STADI-P diffractometer operating in transmission mode, using Co- $K\alpha_1$ radiation selected with a focusing monochromator ($\lambda = 1.78897 \text{ \AA}$), and a linear position-sensitive detector of $\sim 7^\circ$ 2θ active length. The combination of a focusing incident beam monochromator with a position-sensitive detector results in high resolution. This diffractometer is therefore suited for precise lattice parameter measurements. Data were collected in the 2θ range between 10° and 120° by stepping the detector in 0.5° steps, and then combining the overlapped data from successive steps. A small amount of silicon (silicon standard 640b, $a=5.43088 \text{ \AA}$) was used as internal standard. The measured peak positions were calibrated against the Si peaks. Unit-cell parameters were refined using the position of 25 -38 diffraction lines by means of the STOE WinXPOW software.

2.1.3.3 X-ray single-crystal diffraction

Sample S3356 (KAlSi_3O_8) and sample H2495 ($\text{K}_{0.8}\text{Na}_{0.2}\text{AlSi}_3\text{O}_8$) consisted of hollandite phases with crystals larger enough ($\sim 100 \text{ }\mu\text{m}$) for X-ray single-crystal characterisation and structural refinement. Suitable crystals were selected at the optical microscope according to their sharp extinction and to their transparency. The chosen crystals have size $150 \times 100 \times 70 \text{ }\mu\text{m}$ (crystal S3356) and $100 \times 70 \times 70 \text{ }\mu\text{m}$ (crystal H2495). Single-crystal X-ray diffraction data were collected at room conditions on a Xcalibur diffractometer operated at 50 kV and 40 mA, equipped with a CCD detector and a graphite monochromator for $\text{MoK}\alpha_1$ radiation. In order to maximize the reciprocal space coverage, a combination of ω and ϕ scans was used,

with an exposure time of 15 s/frame for crystal S3356 and 40 s/frame for crystal H2495. For sample S3356, 3283 reflections in the range $3 < 2\theta < 90^\circ$ were collected, out of which 564 were unique in the $I4/m$ space group and 511 reflections had $F_o > 4\sigma(F_o)$. For crystal H2495, 3307 reflections were collected in the range $4 < 2\theta < 90^\circ$, 563 were unique reflections of which 518 had $F_o > 4\sigma(F_o)$. Integration of the intensity data and Lorentz and polarization corrections were made using the CrysAlis package (Oxford Diffraction 2006). An empirical absorption correction was performed using the multiscan procedure implemented in the WinGX crystallographic program (Blessing 1995, Faruggia 1999) and the resulting discrepancy factor among symmetry related reflections is $R_{\text{int}} = \sum |F_o^2 - F_o^2(\text{mean})| / \sum F_o^2 = 0.043$ and $R_{\text{int}} = 0.026$ for crystal S3356 and crystal H2495, respectively. Weighted least-squares structural refinements based on F_o^2 were carried out with space group $I4/m$ using the SHELXL-97 program (Sheldrick 1997), starting from the atomic coordinates of Yamada et al. (1984). Neutral atomic scattering curves (International Table of Crystallography 1992) for O, Al, Si, Na, and K were used. Anisotropic temperature factors were used for all atoms. Si and Al were considered completely disordered at the octahedral sites. The analysis of the Fourier-difference map for crystal S3356 revealed a large residual electron density peak ($\sim 1.3 \text{ e}^-$) on the four-fold axis at about 0.6 \AA from the K atom. This suggests that some of the K ions are displaced from the site with $4/m$ point symmetry (Wyckoff position 2a) along the tunnel axis. The same behaviour has been observed for several priderite structures and it has been ascribed to coulombic repulsive forces between the tunnel cations (Watanabe et al. 1987). However, given the small amount of K atoms displaced from the central position, further refinements with an added split position with coordinated $0,0,z$ (Wyckoff position 4e), although gave a better agreement index, did not define a positive isotropic temperature factor for the split site. The final agreement index $R_1 = \sum ||F_o| - |F_c|| / \sum |F_o|$ was 0.025 for 22 refined parameters and 511 reflections with $F_o > 4\sigma(F_o)$.

The analysis of the Fourier-difference map for crystal H2495 also revealed a large residual electron density peak ($\sim 1.5 \text{ e}^-$) at about 0.6 \AA from the K atom, however the coordinated of this residual ($x,y,1/2$) are not along the tunnel axis, but at the Wyckoff position 8h, i.e. closer to the framework walls. In this case a split site (Na1) has been introduced with coordinated $x = 0.0132$, $y = 0.0620$ and $z = 0$ and with isotropic temperature factor. Two restraints relative to

the occupancies of the split site and of the central site (K) have been added: a) a full occupancy of Na and K should be obtained from the sum of the occupancy of site 2a and site 8h; and b) the total Na occupancy has been constrained to the value and uncertainty of the chemical analysis. The final agreement index R_1 was 0.0286 for 25 refined parameters and 518 reflections with $F_o > 4\sigma(F_o)$. Details of the data collection and structural refinement are reported in Table 2.4.

Table 2.4. Crystal data and refinement results for the hollandite single crystals studied in this work.

	S3356	H2495
Nominal composition	KAlSi ₃ O ₈	K _{0.8} Na _{0.2} AlSi ₃ O ₈
a (Å)	9.322 (1)	9.3214 (2)
c (Å)	2.726 (1)	2.7232 (2)
V (Å ³)	236.89 (7)	236.61 (1)
Space group.	$I 4/m$	$I 4/m$
Nr. unique reflections	564	563
Nr reflections with $F_o > 4\sigma(F_o)$	511	518
R_{int} (%)	4.3	2.6
R_{all} (%)	2.95	3.38
R_1 (%)	2.53	2.86
GooF	1.104	1.154
Refined parameters	22	25

2.2 High-pressure and high-temperature techniques

2.2.1 Diamond anvil cells

The diamond anvil cell (DAC) technique was used for high-pressure high-temperature studies in order to understand the behaviour of K-Na silicate hollandite at the Earth's mantle conditions. The DAC technique makes use of two gem-quality diamonds to apply a force to a sample. Such technique revolutionized the high-pressure research (Eremets, 1996; Hazen and Finger, 1982; Hemley, 1998) since it is very versatile and can be used for different kinds of experiments as Mössbauer, infrared and Raman spectroscopies, resistivity, X-ray diffraction and inelastic scattering measurements. This is due to the fact that the diamonds are transparent to most of the spectrum of electromagnetic radiation, including γ -ray, X-ray, portions of ultraviolet, visible, and most of the infrared region, and the P-T condition in the DAC can be kept constant for long periods of time. The installation of high-pressure beam lines at synchrotron facilities, along with recent developments in X-ray diffraction techniques, have significantly improved our ability to measure the phase behaviour of many minerals at extreme pressure and temperature conditions.

In the DAC, the sample is placed between the polished culets of two diamonds and is contained on the sides by a metal gasket. The size of the diamond culet (the working area of a DAC) determines the maximum pressure that can be achieved during an experiment. In this study diamonds with culet diameter of 300 and 400 microns were used to generate pressure up to 35 GPa. A hole drilled at the center of the gasket serves as the pressure chamber. The strength, or the internal friction of the gasket, must be greater than the radial forces in the pressure chamber. Steel and rhenium gaskets were used in this study. The samples were placed in the pressure chamber together with a pressure transmitting medium and pressure calibrant. Ruby and gold were used as pressure sensors. When ruby was the pressure calibrant, the ruby fluorescence method (Mao *et al.*, 1986) was used. Ruby has a strong fluorescence spectrum which depends on pressure. Small pieces of ruby are placed in the pressure chamber along with the sample, and the increase in pressure can be monitored by the shift of the fluorescence line (Figure 2.4). However, ruby has a limited usefulness at high temperatures because of the excessive broadening of the ruby lines above 670 K (Wunder and Schoen, 1981; Shimomura *et al.*, 1982). Gold is used as a primary internal pressure calibration standard for high pressure and high temperature experiments. If the temperature is known, the lattice parameters of Au can be used to determine the pressure. Au is chemical inert, and is stable over a large range of pressures and temperatures, moreover, there is a considerable amount of data to constrain its

equation of state. Also, because of its simple structure and high atomic number, it is relatively easy to constrain the lattice parameter of Au by X-ray diffraction (Anderson et al. 1989; Dubrovinsky et al. 2007). The pressure transmitting medium is normally a soft material with low shear strength to minimize deviatoric stresses in the sample, chemical inertness, and low absorption. Argon, helium and lithium fluoride were used in this study. Argon and helium are both noble gas at room pressure, and are chemical inert and transparent. Ar is known to provide hydrostatic conditions only up to 8 GPa, however as a soft noble gas it can still provide quasi-hydrostatic conditions at much higher pressures. Helium has excellent hydrostaticity, small X-ray scattering factor and small thermal conductivity. It is reported that helium maintain (quasi)-hydrostatic conditions up to at least 50-70 GPa (Kenichi, 2001; Miletich et al., 2000). However loading He in a DAC requires a special apparatus which are not commonly available. Lithium fluoride, LiF, is a chemically stable soft material, and has the advantage that it cannot only be used as pressure transmitting medium, but also as pressure calibrant in X-ray diffraction experiments. With respect to NaCl and NaF, which are commonly used, its structure is stable up to at least megabar pressures (Dubrovinsky, private communication). Furthermore, LiF is a light material with low absorption, low scattering factor for sample measurements through the DAC. In recent high-pressure studies there have been an increasingly use of LiF under extreme conditions in diamond anvil cell experiments. However, no recent measurements have been performed to better constrain its equation of state and thermal expansivity. Moreover, the properties of LiF under high pressures and high temperatures were determined only in a very limited pressure and temperature range up to 9 GPa and 800 °C (Yagi, 1978). Given the improvements of the DAC technique in the last decade, new measurements of the equation of state and thermal expansivity of LiF up to 32 GPa and 720 °C have been carried out in this study to better constrain the high-pressure and high-temperature behaviour of this material. The results obtained are reported in the next chapter.

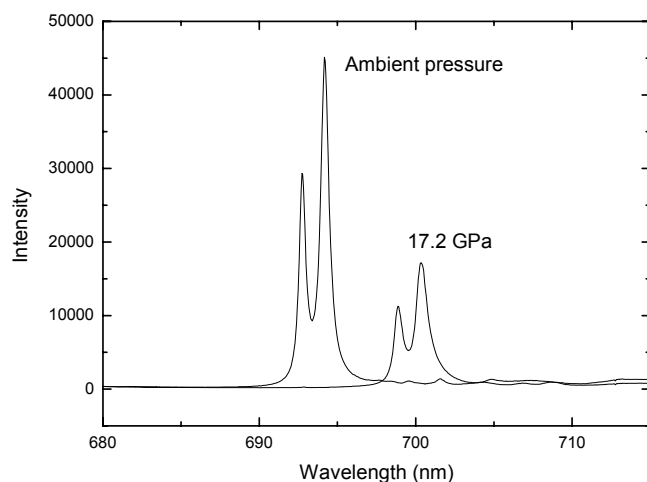


Figure 2.4 An example of ruby fluorescence line shifts with pressure in Raman experiment.

Heating of the DAC was obtained by electrical heating to temperatures up to ~ 800 °C. With electrical heating the temperature is easy to measure with thermocouples, and can be maintained at a constant value for several hours. Resistive heaters were placed around the diamond anvils. An S type thermocouple was placed near the center of the cell, next to the gasket-sample interface. In externally heated DAC at $T > 800$ K stresses are practically absent and the heating is quite homogeneous (Dubrovinsky *et al.*, 1999).

2.2.2 Raman experiments

Raman spectroscopy is a spectroscopic technique commonly used in many scientific and industrial disciplines. It has been used successfully in nearly all geosciences disciplines and virtually all kinds of samples have been studied using this technique. The Raman spectroscopy study of vibrational properties of minerals, glasses, melts and fluids at high pressure and high temperature has important applications in mineral and geosciences (Ferraro, 1984; Gillet, 1996; Gillet *et al.*, 1998). The development of the diamond anvil cell has opened up new possibilities for *in situ* Raman spectroscopic experiments in minerals at high pressures as well as at high and low temperatures (Jayaraman, 1983, 1986; Ferraro, 1984; Chervin *et al.* 1992). Raman spectroscopy mostly in conjunction with the DAC technique has been used to investigate the structure and the high-pressure high-temperature behaviour of minerals, glasses, melts and liquids.

In a Raman spectrum, the Raman shifts correspond to frequencies of vibrations in the sample, *i.e.*, each band in a Raman spectrum represents the interaction of the incident light with a certain vibration of the nuclei. The vibration of the nuclei are controlled by the sizes, valences and masses of the atomic species of which the sample is composed, the bond forces between these atoms, and the symmetry of their arrangement in the crystal structure (bond directions). These factors affect not only the frequencies of atomic vibrations and the observed Raman shifts, but also the number of observed Raman bands, their relative intensities, their widths (typically expresses as FWHM, ‘full width at half band maximum intensity’) and their polarizations. Therefore, Raman spectra are highly specific for a certain type of material and can be used for the identification and structural characterization of unknown samples. The use of Raman spectroscopy has many advantages. First of all, for a quick analysis of a material, there is no need of powdering, thinning, sawing scraping, breaking, drilling, coating/sputtering, dissolving or polishing the sample. Raman spectra can be in fact collected without destruction of the sample. The Raman technique has an excellent volume resolution down to the micron scale. This allows for the analysis of tiny amounts of sample and truly microprobe analysis. Due to the excellent volume resolution, information on the homogeneity/heterogeneity of a sample can be obtained with a lateral resolution of $\sim 1\mu\text{m}$ (Nasdala *et al.*, 2004).

In our experiments, the Raman scattering measurements were carried out on two Raman spectrometers: a Dilor XY system with the 514.5nm Ar⁺ ion laser equipped with a microscope and liquid-nitrogen-cooled CCD detector, and a LABRAM Raman spectrometer with a He-Ne laser with the 632 nm red line excitation. The spectrometers were calibrated using the Γ_{25} phonon of diamond Si ($Fd\bar{3}m$). The vibrational peaks were analysed using the PeakFitTM program by Jandel Scientific. The Savitsky-Golay data-smoothing algorithm was used in the peak analysis. Combinations of Lorentzian and Guassian function were used to describe the peak profile. At ambient conditions, the instrument resolution is 2 cm^{-1} for the peak position, and resolution for peak width (full width at half maximum, FWHM) is 0.5 cm^{-1} given by the peak fitting software.

2.2.3 High pressure X-ray powder diffraction experiments

X-ray diffraction at high pressures is a domain of crystallography that permits insight into structural properties of the solid state, through structural and physical changes occurring when the pressure is varied. Powder-diffraction methods cover a broad static-pressure range in studies of crystal structure, equation of state and phase transitions. The experimental methods that underpin such investigations continue to become increasingly sophisticated. Progress has been made in the design of pressure cells suitable for the application of extremely high pressures and temperatures, and in the properties of the synchrotron X-ray beams used as sources of X-rays in diffraction studies (Paszkwicz 2002).

2.2.3.1 High-pressure X-ray experiments at the BGI

Thanks to recent advances in conventional X-ray diffractometers, collecting data of powder samples at high pressures using *in house* facilities can be now an alternative to the use of synchrotron radiation. The high-brilliance X-ray system installed recently at the BGI is aimed to provide the possibility for diffraction studies at high pressures of different type materials. This system consists of three major components a RIGAKU FR-D high-brilliance source, OSMIC Inc. Confocal Max-Flux optics, and a SMART APEX 4K CCD area detector. The FR-D high-brilliance X-ray Mo rotating anode generator operates at load up to 3.3 kW. The initial beam spot has elliptical shape with the FWHM of the vertical axis of about 200 mm and of the horizontal axis of about 100 mm. The initial beam is focused by the confocal CMF optics. Utilizing constructive interference as in Bragg diffraction, thin film multilayers reflect X-rays at larger angles than total reflection mirrors, yielding a larger capture angle and thus larger flux. The significant advantage of the multilayer mirrors is their capability to act as natural band-pass filters, automatically monochromazing the beam thereby providing more intensity with smaller background. These custom made collimating and focusing 100 mm long mirrors are realized by curving the mirror surfaces into parabolic shapes. A two-dimensional reflection system is realized by using two mirrors in a “side-by-side” Kirkpatrick-Baez scheme. Each mirror independently reflects X-rays in one of the two perpendicular directions. Both mirrors of Confocal Max-Flux optics can be manually positioned with the “side-by-side” scheme in order to optimize the performance parameters including flux, spectrum, and divergence. In order to enhance the system application for DACs, the CMF optics are designed for focusing

on the sample plane a round beam with the FWHM diameter of about 40 mm. The SMART APEX CCD detector with 62 mm 4K chip provides unit demagnification and sensitivity of about 170 electrons per photon. The system is quite versatile and can be used for collecting data from both powder and single-crystal samples. However, its major purpose is the *in situ* study of powder samples at high pressure in DACs. In this study, using the high-brilliance X-ray system we measured compressibility of K-hollandite with different Na component.

2.2.3.2 Synchrotron radiation X-ray powder diffraction

When charged particles, in particular electrons or positrons, are forced to move in a circular orbit, photons are emitted. At relativistic velocities (when the particles are moving at a speed close to that of light) these photons are emitted in a narrow cone in the forward direction at a tangent to the orbit. In a high energy electron or positron storage ring these photons are emitted with energies ranging from infra-red to energetic (short wavelength) X-rays. This radiation is called Synchrotron Radiation.

Synchrotron radiation has a number of unique properties:

- High brightness: synchrotron radiation is extremely intense (hundreds of thousands of times more intense than conventional X-ray tubes) and highly collimated.
- Wide energy spectrum: synchrotron radiation is emitted with a wide range of energies, allowing a beam of any energy to be produced.
- Synchrotron radiation is highly polarized.
- It is emitted in very short pulses, typically less than a nano-second (a billionth of a second)

One of the first techniques to make use of synchrotron radiation was X-ray crystallography: the determination of crystal structure from X-ray diffraction data. The use of intense radiation has revolutionized the high-pressure and high-temperature research, as it enabled the study of very small samples and the collection of data in relatively small time scales of seconds to minutes. The combination of high-pressure cells with synchrotron sources creates the best conditions for studies in an extended range of pressures and temperatures. Principles of powder XRD in DAC's and description of the instrumentation at synchrotron beamlines are

provided by Fei & Wang (2000). Comprehensive reviews of high-pressure powder diffraction techniques and a review of the current state-of-the-art techniques have recently been presented in articles by Paszkowicz (2002) and McMahon (2004).

In this study, high pressure and high temperature synchrotron radiation X-ray powder diffraction data were collected at the European synchrotron Radiation Facility (ESRF, Grenoble, France) on beam line ID-27 (wave length = 0.26472 Å), beam line ID-09 (wave length = 0.4121 Å), and beam line ID-30 (wave length = 0.3738 Å). Samples were put into diamond cells together with pressure transmitting medium and pressure calibrant. The obtained diffraction pattern were integrated using the Fit2d software and the results obtained are presented in the next chapter.

3. Results

3.1 (K,Na)AlSi₃O₈ hollandite solid solution

In order to characterize the Na/K substitution into the aluminosilicate hollandite structure, two different sets of experiments were carried out. First different amounts of Na content were added into the KAlSi₃O₈ end-member to quantify the maximum amount of substitution at different pressure and temperature; second several attempts were made to synthesize the NaAlSi₃O₈ hollandite end-member. The results obtained from these experiments are described in details in the following.

3.1.1 Chemical composition

The run-products of the synthesis experiments were analyzed by scanning electron microscope, electron microprobe, X-ray powder diffraction, and Raman spectroscopy. The synthesis conditions and recovered phases are listed in Table 3.1. Homogeneous assemblages with a pure hollandite phase (and a very small amount of stishovite) were synthesized at temperature of 1700 °C and different pressures with 0%, 10%, 30%, 40%, 50% of Na component. All experiments conducted using NaAlSi₃O₈ albite glasses as starting material failed in producing the hollandite structure. Also the experiment carried out with an albite glass containing small amounts of Ca and K as to simulate the natural occurrence of Na-hollandite in shock melt veins (Gillet *et al.*, 2000; Tomioka *et al.*, 2000; Xie *et al.*, 2001) resulted in a run-product consisting of a mixture of phases. Examples of SEM BSE images of different run-products are shown in Figure 3.1. The different phases present are clearly visible due to their different contrast. The (K,Na)AlSi₃O₈ hollandite phase appears usually as relatively large and homogeneous crystals in light-grey. The run-products resulted from the high-pressure experiments up to 22.5 GPa of the albite glass consist of a mixture of phases having very small grain size difficult to analyze with SEM and microprobe. Their X-ray diffraction pattern is consistent with a mixture of jadeite and stishovite and no hollandite reflections have been observed.

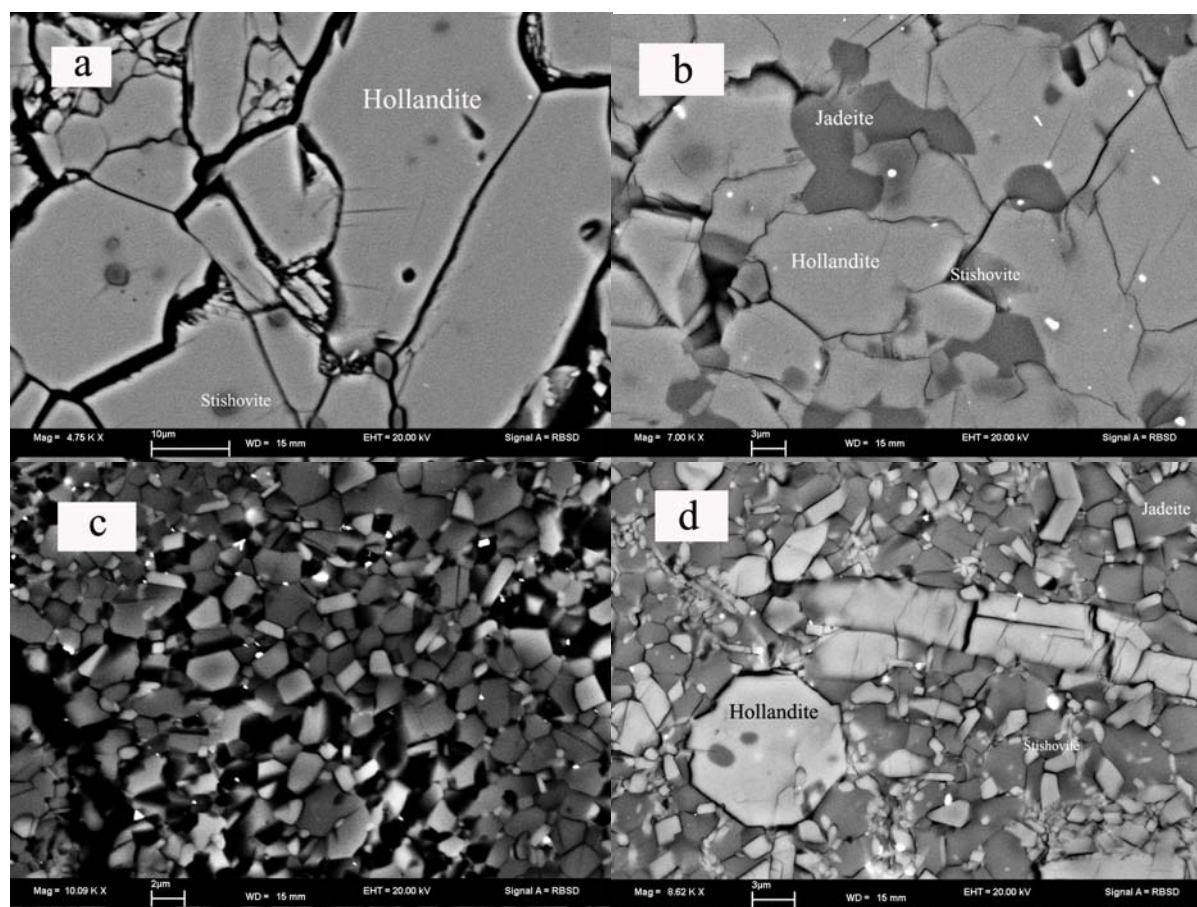


Figure 3.1. Examples of SEM BSE images of four synthesized samples. The light grey crystals are $(\text{K},\text{Na})\text{AlSi}_3\text{O}_8$ hollandite, the dark grey crystals are jadeite, whereas the dark cloud-looking phase is stishovite. The very bright spots are contamination from the Re capsule. a) S3461 sample obtained from $\text{K}_{0.7}\text{Na}_{0.3}\text{AlSi}_3\text{O}_8$ glass at 20 GPa and 1700 °C. The run product consists of $\text{K}_{0.7}\text{Na}_{0.3}\text{AlSi}_3\text{O}_8$ hollandite with minor stishovite inclusions. b) S3442 sample synthesized from $\text{K}_{0.7}\text{Na}_{0.3}\text{AlSi}_3\text{O}_8$ glass at 15 GPa and 1700 °C. The run product has the composition of $\text{K}_{0.860}\text{Na}_{0.132}\text{Al}_{1.006}\text{Si}_{2.997}\text{O}_8$ hollandite coexisting with stishovite and jadeite. c) H2116 sample synthesized from $\text{NaAlSi}_3\text{O}_8$ glass at 21 GPa and 1700 °C. The run-product appears as a complex mixture of phases with very small grain size. d) S3726 sample synthesized from $\text{Na}_{0.75}\text{K}_{0.05}\text{Ca}_{0.1}\text{AlSi}_3\text{O}_8$ glass at 22 GPa and 1900 °C. The recovered capsule contains $\text{K}_{0.259}\text{Na}_{0.533}\text{Ca}_{0.161}\text{Al}_{1.153}\text{Si}_{2.856}\text{O}_8$ hollandite, jadeite, and stishovite.

Chemical analysis by means of electron microprobe was performed on all run products. The results obtained for the samples consisting mainly of the hollandite phase are reported in Table 3.2.

Table 3.1. Synthesis conditions and obtained run-product phases. The nominal composition is reported for the starting material, whereas the composition of the hollandite phases results from the microprobe analysis.

Samples	Compositions of starting material	<i>P</i> (GPa)	<i>T</i> (°C)	Coexisting phases in recovered samples
S3436	KAlSi ₃ O ₈	13	1700	K _{1.04} Al _{1.04} Si _{2.96} O ₈ hollandite, stishovite*
S3356	KAlSi ₃ O ₈ oxide mixture	13	1500	K _{0.94} Al _{1.05} Si _{2.98} O ₈ hollandite, stishovite*
S3600	K _{0.9} Na _{0.1} AlSi ₃ O ₈	15	1700	K _{0.92} Na _{0.09} Al _{1.04} Si _{2.97} O ₈ hollandite, stishovite*
S3439	K _{0.7} Na _{0.3} AlSi ₃ O ₈	13	1700	K _{0.90} Na _{0.12} Al _{1.03} Si _{2.97} O ₈ hollandite, stishovite, jadeite
S3442	K _{0.7} Na _{0.3} AlSi ₃ O ₈	15	1700	K _{0.86} Na _{0.13} Al _{1.01} Si _{3.00} O ₈ hollandite, stishovite, jadeite
H2216	K _{0.7} Na _{0.3} AlSi ₃ O ₈	17	1700	K _{0.82} Na _{0.17} Al _{1.00} Si _{3.00} O ₈ hollandite, stishovite, jadeite
S3461	K _{0.7} Na _{0.3} AlSi ₃ O ₈	20	1700	K _{0.70} Na _{0.29} Al _{1.01} Si _{3.00} O ₈ hollandite, stishovite*
H2229	K _{0.7} Na _{0.3} AlSi ₃ O ₈	20	1700	K _{0.72} Na _{0.29} Al _{0.99} Si _{3.01} O ₈ hollandite, stishovite*
S3524	K _{0.5} Na _{0.5} AlSi ₃ O ₈	20	1700	K _{0.73} Na _{0.31} Al _{1.02} Si _{2.97} O ₈ hollandite, jadeite, stishovite
H2305	K _{0.5} Na _{0.5} AlSi ₃ O ₈	22	1700	K _{0.53} Na _{0.53} Al _{1.04} Si _{2.96} O ₈ hollandite, stishovite*
H2502	K _{0.5} Na _{0.5} AlSi ₃ O ₈	22	1700	K _{0.52} Na _{0.46} Al _{1.03} Si _{2.98} O ₈ hollandite, stishovite*
S3598	K _{0.4} Na _{0.6} AlSi ₃ O ₈	22	1700	K _{0.59} Na _{0.46} Al _{1.03} Si _{2.96} O ₈ hollandite, jadeite, stishovite
H2495	K _{0.8} Na _{0.2} AlSi ₃ O ₈ oxide mixture	20	1700	K _{0.81} Na _{0.19} Al _{1.02} Si _{2.98} O ₈ hollandite, stishovite*
H2353	K _{0.5} Na _{0.5} AlSi ₃ O ₈ oxide mixture	22	1700	K _{0.58} Na _{0.40} Al _{1.04} Si _{2.97} O ₈ hollandite, jadeite, stishovite
S3726	Na _{0.75} K _{0.05} Ca _{0.1} AlSi ₃ O ₈	22	1900	K _{0.26} Na _{0.53} Ca _{0.16} Al _{1.15} Si _{2.86} O ₈ hollandite, jadeite, stishovite, unknown phase
S3785	Na _{0.75} K _{0.05} Ca _{0.1} AlSi ₃ O ₈	26	2200	Badly contaminated with Mg and Zr and other material from the octahedron assembly
S3445	NaAlSi ₃ O ₈	20	1700	Jadeite and stishovite
H2116	NaAlSi ₃ O ₈	21	1700	Jadeite and stishovite
H2306	NaAlSi ₃ O ₈	22.5	1700	Jadeite and stishovite

* Content less than 3-4 %.

From the microprobe analysis it appears that the albite glass containing a small amount of Ca and K (experiment S3726) indeed produced a hollandite phase, although in a complex phases assemblage containing also jadeite, stishovite and a phase that could not be identified. The ratio $\text{Na}/(\text{Na}+\text{K}+\text{Ca}) = 0.56$ of this hollandite phase is greater than the $\text{Na}/(\text{Na}+\text{K})$ ratio of any other experiment performed in this study.

Table 3.2. Selected microprobe analyses for the homogeneous hollandite samples. Also elements such as Fe, Mg, and W which can contaminate the sample during the synthesis experiments were analyzed, and resulted in a negligible amount (on the order of the uncertainties).

Wt%	S3436	S3356	S3600	S3439	S3442	H2216	H2229	S3524	H2305
SiO ₂	64.31 (89)	64.11 (31)	65.17 (32)	64.54 (30)	65.29 (66)	65.47 (33)	66.34 (1.43)	65.90 (70)	66.41 (81)
Al ₂ O ₃	19.24 (63)	19.16 (19)	19.48 (19)	19.00 (16)	18.57 (29)	18.58 (32)	18.36 (79)	19.22 (39)	19.80 (43)
Na ₂ O			0.98 (07)	1.40 (15)	1.48 (23)	1.96 (40)	3.19 (30)	3.56 (33)	6.15 (26)
K ₂ O	17.82 (34)	15.92 (24)	15.77 (43)	15.30 (33)	14.69 (25)	14.00 (60)	12.17 (53)	12.76 (60)	9.40 (30)
Total	101.44 (26)	99.19 (48)	101.57 (43)	100.24 (31)	100.10 (47)	100.02 (35)	100.078 (45)	101.59 (52)	101.75 (35)
Si	2.957 (32)	2.977 (6)	2.966(8)	2.971 (6)	2.997 (15)	2.999 (12)	3.009 (37)	2.972 (21)	2.955 (26)
Al	1.043 (37)	1.049 (7)	1.045 (9)	1.031 (8)	1.006 (19)	1.003 (16)	0.989 (37)	1.022 (21)	1.038 (25)
Na			0.086 (6)	0.125 (14)	0.132 (21)	0.174 (35)	0.294 (27)	0.311 (29)	0.530 (23)
K	1.045 (23)	0.943 (15)	0.916 (25)	0.898 (20)	0.860 (15)	0.818 (34)	0.720 (34)	0.734 (35)	0.533 (18)
Total	5.044 (26)	4.970 (11)	5.013 (20)	5.025 (11)	4.957 (180)	4.995 (13)	4.984 (50)	5.039 (24)	5.057 (30)

3.1.2 X-ray powder diffraction

In our synthesis experiments, hollandite containing up to 50% Na have been successfully synthesized at 22 GPa and 1700 °C. X-ray powder diffraction analysis have been carried out for each hollandite sample containing different Na, and K component. Indexed XRD patterns of pure KAlSi₃O₈ hollandite (sample 3436) and of K_{0.72}Na_{0.29}AlSi₃O₈ (sample H2229) are shown in Fig. 3.2 as examples. The unit-cell lattice parameters of the K/Na hollandite solid solution were calculated with the STOE software using between 25 and 36 reflections (Table 3.3). The variation of the unit-cell parameters as a function of Na content is illustrated in Figure 3.3. The *a* and *c* cell parameters decrease linearly with increasing NaAlSi₃O₈ component, resulting in a decrease of the unit-cell volume *V*. The *a* axis decreases of 0.34% up to *X*_{Na}=0.53, whereas the *c* axis decreases of 0.29%. Linear fits through the data result in the following expressions: $a = 9.3306(3) - 0.0602(1)X_{Na}$ and $c = 2.7261(3) - 0.0133(1)X_{Na}$. Extrapolation to the NaAlSi₃O₈ hollandite end-member using these linear fits results in $a = 9.27$ Å, and $c = 2.71$ Å. These values are in very good agreement with those reported by Gillet et al. (2000) for the NaAlSi₃O₈ hollandite occurring in the shock melt vein of Sixiangkou meteorite: $a = 9.263(3)$ Å, and $c = 2.706(3)$ Å.

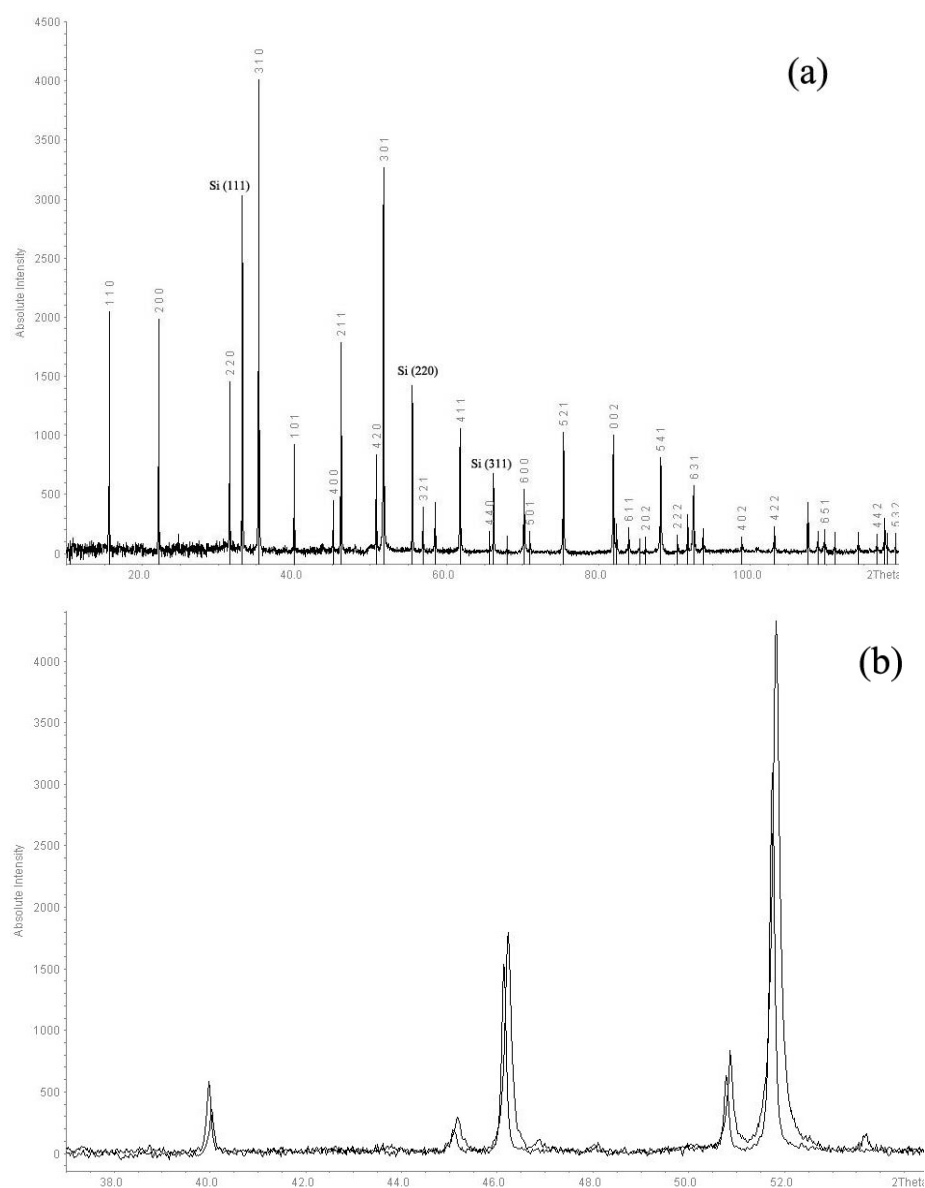


Figure 3.2. a) Indexed diffraction pattern of pure KAlSi_3O_8 hollandite. Note that a small amount of silicon powder was used as internal standard. b) Comparison between the diffraction patterns of KAlSi_3O_8 and $\text{K}_{0.72}\text{Na}_{0.29}\text{AlSi}_3\text{O}_8$ hollandites. The peak shift toward larger 2θ values indicates that the cell volume decreases as Na substitutes into the KAlSi_3O_8 hollandite end-member structure. In these figures backgrounds were subtracted using the Stoe software.

Table 3.3. Unit-cell lattice parameters of the KAlSi_3O_8 - $\text{NaAlSi}_3\text{O}_8$ hollandite solid solution synthesised in this study

Samples	Composition	Number of indexed peaks	a_0 (Å)	c_0 (Å)	V_0 (Å ³)
S3436	$\text{K}_{1.045}\text{Al}_{1.043}\text{Si}_{2.96}\text{O}_8$	34	9.32969 (22)	2.72721 (9)	237.385 (8)
S3356	$\text{K}_{0.943}\text{Al}_{1.049}\text{Si}_{2.977}\text{O}_8$	36	9.3350 (3)	2.72572 (11)	237.526 (10)
S3600	$\text{K}_{0.916}\text{Na}_{0.086}\text{Al}_{1.045}\text{Si}_{2.966}\text{O}_8$	38	9.32626 (21)	2.72505 (9)	237.023 (8)
S3439	$\text{K}_{0.898}\text{Na}_{0.125}\text{Al}_{1.031}\text{Si}_{2.971}\text{O}_8$	31	9.3230 (8)	2.7275 (7)	237.07 (6)
S3442	$\text{K}_{0.860}\text{Na}_{0.132}\text{Al}_{1.006}\text{Si}_{2.997}\text{O}_8$	36	9.3235 (8)	2.7265 (5)	237.01 (4)
H2216	$\text{K}_{0.818}\text{Na}_{0.174}\text{Al}_{1.003}\text{Si}_{2.999}\text{O}_8$	25	9.3202 (6)	2.7233 (3)	236.56 (3)
H2229	$\text{K}_{0.720}\text{Na}_{0.294}\text{Al}_{0.989}\text{Si}_{3.009}\text{O}_8$	25	9.3133 (5)	2.72256 (24)	236.146 (23)
S3524	$\text{K}_{0.734}\text{Na}_{0.311}\text{Al}_{1.022}\text{Si}_{2.972}\text{O}_8$	31	9.3117 (6)	2.7220 (3)	236.017 (24)
H2305	$\text{K}_{0.533}\text{Na}_{0.530}\text{Al}_{1.038}\text{Si}_{2.955}\text{O}_8$	29	9.2984 (4)	2.71920 (17)	235.103 (15)

Unit-cell lattice parameters data reported for the KAlSi_3O_8 - $\text{NaAlSi}_3\text{O}_8$ solid solution by Yagi et al (1994) also are plotted in Figure 3.3. The variations as a function of Na content of Yagi et al. (1994) data is much smaller than that found in our study. Moreover the maximum solubility of $\text{NaAlSi}_3\text{O}_8$ component into the KAlSi_3O_8 hollandite-type structure was reported by those authors to be about 40 mol% at 1000 °C and 22.5 GPa, whereas for higher Na content the high pressure phase appears to be that of the calcium-ferrite type structure. In our experiments performed at higher temperature (1700 °C), the solubility of the $\text{NaAlSi}_3\text{O}_8$ component into the KAlSi_3O_8 hollandite structure significantly increased (Figure 3.4). Also, higher pressures are needed to stabilise the Na-rich hollandite structure with respect to a mixture of Na-poor hollandite + jadeite + stishovite phases. In our experiments, the maximum solubility of Na component into the KAlSi_3O_8 hollandite end-member is ~ 53%, in agreement with the results reported by Liu (2006) which show a maximum content of $\text{NaAlSi}_3\text{O}_8$ of ~51% at ~ 22 GPa and 2200 °C.

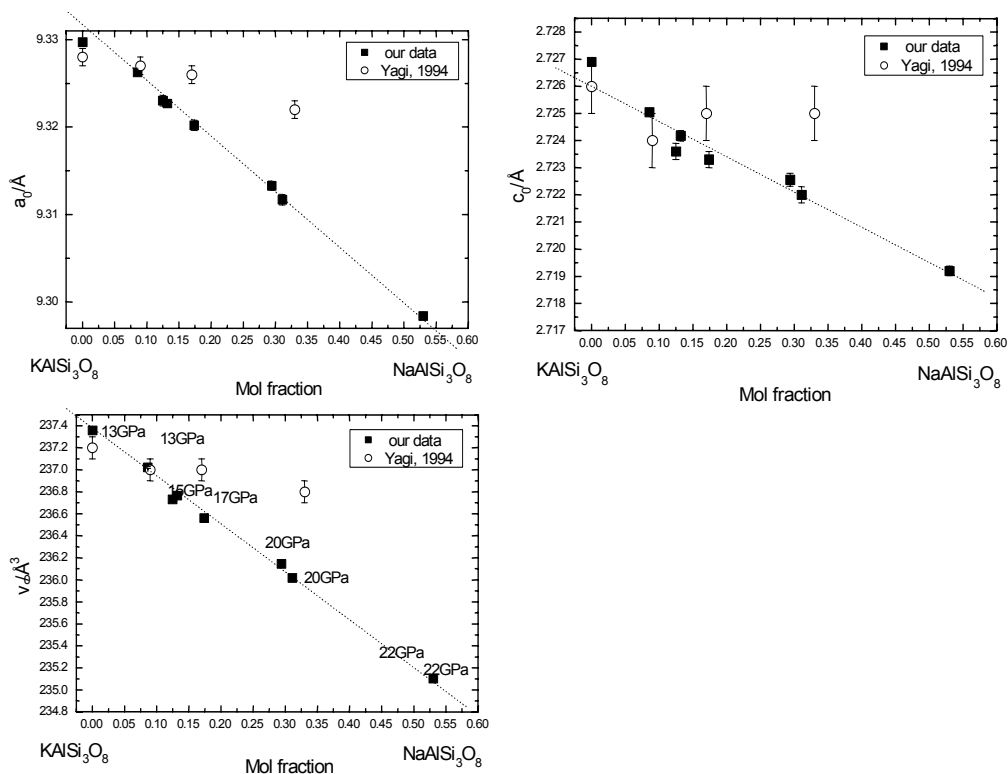


Figure 3.3. Unit-cell lattice parameters of (K,Na)AlSi₃O₈ hollandite solid solutions. Solid squares are the data obtained in this study; open circles are data from the previous study by Yagi et al (1994) at 1000 °C. Vertical bars show the experimental errors.

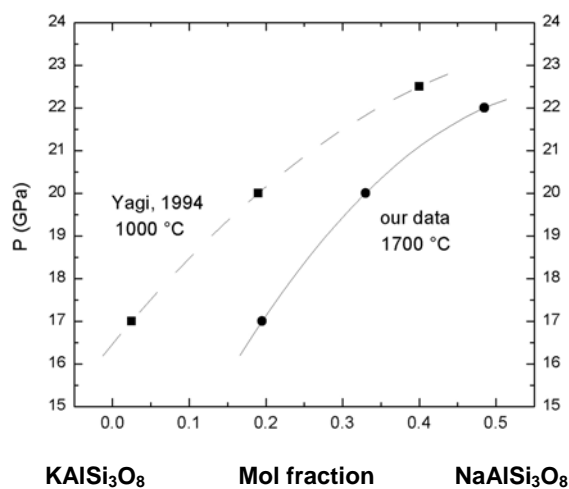


Figure 3.4. The data presented here from Yagi et al (1994) (solid squares) and from this study (solid circles) represent run products with mixtures of (K,Na)AlSi₃O₈ hollandite, jadeite and stishovite. The solubility of NaAlSi₃O₈ component into the KAISi₃O₈ end-member at 1700°C appears larger than in the study of Yagi et al (1994) at 1000 °C.

3.1.3 Raman spectra

The hollandite structure is closely related to the rutile structure rearranged to form open tunnel where large cations and water can be accommodated. Stishovite, a high-pressure SiO_2 polymorph, also has a rutile-type structure and we can expect its Raman spectrum to be very similar to that of aluminosilicate-hollandite (Hemley *et al.*, 1986; Gillet *et al.* 2000). The Raman spectrum collected at room conditions for KAlSi_3O_8 S3356 sample and a stishovite sample (synthesized in the multi-anvil press at 1500 °C and 14 GPa) using a LABRAM Raman spectrometer with a He-Ne laser with the 632 nm red line excitation are compared in Figure 3.5. The effect of Na substitution into the KAlSi_3O_8 hollandite structure can be seen in Figure 3.6 where the Raman spectra collected using a Dilor XY system with the 514.5 nm Ar^+ ion laser for samples S3356, S3600, H2495, H2229, and H2305 containing about 0, 10%, 20%, 30%, 50% $\text{NaAlSi}_3\text{O}_8$ component respectively are compared. Stishovite has 4 Raman-active bands at 967, 753, 589 and 231 cm^{-1} , which are assigned to the B_{1g} , E_g , A_{1g} , and B_{2g} fundamentals, respectively (Hemley *et al.*, 1986).

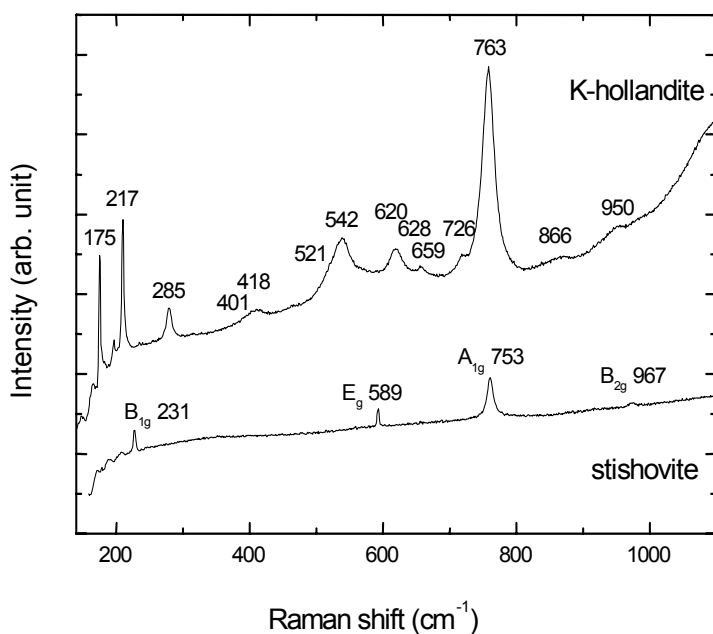


Figure 3.5. Comparison between the Raman spectra of stishovite and that of KAlSi_3O_8 hollandite.

The space group of all recovered (K,Na)AlSi₃O₈ hollandite samples is *I4/m*, and according to selection rules (Fateley et al., 1971) the irreducible representations of the optic modes of KAlSi₃O₈ hollandite end-member are:

$$\Gamma = 6\text{Ag} + 6\text{Bg} + 6\text{Eg} + 3\text{Au} + 3\text{Bu} + 5\text{Eu}$$

of which 18 modes (Ag, Bg and Eg) are Raman active, and 11 modes (Au, Bu and Eu) are infrared active. In the Raman spectra collected in this study 14 vibrational bands are observed for the KAlSi₃O₈ hollandite end-member (Fig. 3.6). The strongest peak at $\sim 765 \text{ cm}^{-1}$ of the hollandites spectra can be assigned to Si-O stretching vibrations in the SiO₆ octahedra by comparison with a similar intense peak observed in the spectrum of stishovite (SiO₂). The peak at $\sim 175 \text{ cm}^{-1}$ has only been observed in samples S3356 and H2495 but not in other samples, probably due to the difference in sample crystalline quality and orientations, since samples S3356 and H2495 are the only run products with large single crystals. By comparison with previously reported Raman spectra of synthesized KAlSi₃O₈ hollandite and naturally found NaAlSi₃O₈ hollandite by Gillet et al. (2000), 5 more Raman bands are observed here. The peak position of the vibrational modes between 200 and 800 cm^{-1} is reported in Table 3.4, and the variation of the peak position as a function of composition is shown in Figure 3.7. Samples with different Na component show similar spectra, with most of the Raman modes having no significant shifts.

Table 3.4. Peak positions of Raman vibrational modes of (K,Na)AlSi₃O₈ hollandite.

Na content (mol %)		Peak positions (cm^{-1})				
0	217.1	285.9	401.4	418.6	521.8	542.1
9	216.7	285.8	394.6	417.0	521.9	543.9
19	216.4	284.9	391.8	419.8	525.2	545.1
29	216.2	283.6	398.1	422.9	516.4	540.8
53	217.0	283.1	396.4	423.3	524.9	547.0
Na content (mol %)		Peak positions (cm^{-1})				
0	620.6	628.9	663.0	726.3	763.1	
9	624.3	639.5	662.7	728.0	763.1	
19	622.9	632.0	658.3	750.0	764.2	
29	621.9	650.8	693.0	723.2	763.6	
53	621.2	629.3	662.7	720.7	764.3	

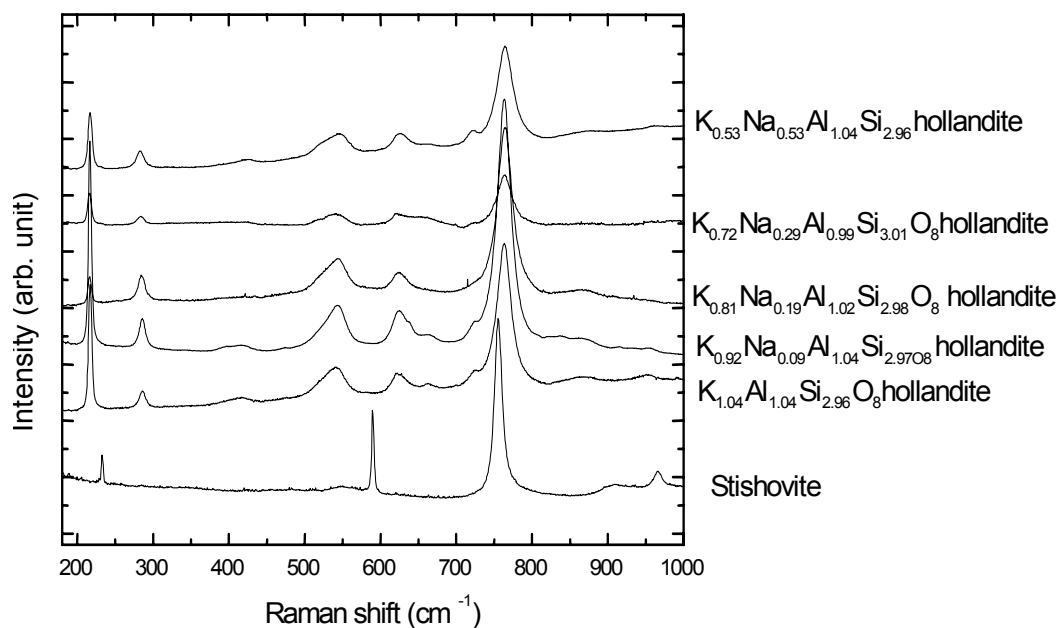


Figure 3.6. Raman spectra of hollandite samples with different Na content. The strongest peak at ~ 765 cm^{-1} can be assigned to Si-O stretching vibrations in the SiO_6 octahedra by comparison with a similar intense peak observed in the spectrum of stishovite (SiO_2). The Raman spectra of the $\text{K}_{0.72}\text{Na}_{0.29}\text{Al}_{0.99}\text{Si}_{3.01}\text{O}_8$ hollandite had a high background and was subtracted using a polynomial fit with the software LABSPEC (1997) of the Raman spectrometer.

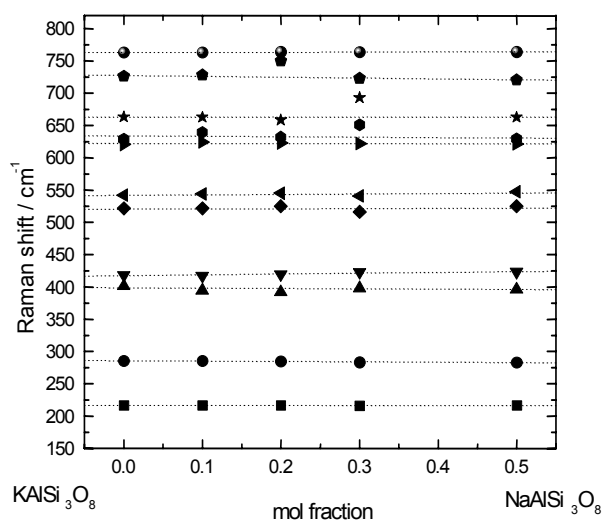


Figure 3.7. Variation of the vibrational modes of hollandite samples as a function of $\text{NaAlSi}_3\text{O}_8$ component. It appears that the Na content does not affect the position of most of the Raman modes in the region between 200 and 800 cm^{-1} .

3.1.4 Crystal structure

Atomic coordinates and equivalent displacement parameters obtained from the structural refinements of the intensity data collected for sample S3356 (KAlSi_3O_8) and sample H2495 ($\text{K}_{0.8}\text{Na}_{0.2}\text{AlSi}_3\text{O}_8$) hollandites are reported in Table 3.5; cation – oxygen bond distances and bond angles are reported in Table 3.6. The hollandite structure determined for sample H2495 is shown in Figure 3.8.

No evidence of ordering between Si and Al among octahedral sites has been found for both hollandite crystals. There are four unique bond distances in the distorted Si(Al)O_6 octahedron. Following the nomenclature reported by Zhang et al. (1993), the oxygen atoms in the equatorial plane parallel to *c* are denoted as O1b and O2b, whereas the apical oxygen atoms are denoted as O1a and O2a (Fig 3.8). Note, however that O1a and O1b, and O2a and O2b are symmetrically related. Each octahedron has four shared edges: two $\text{O1b}\cdots\text{O2b}$ and two $\text{O1a}\cdots\text{O1b}$ which are significantly shorter than the unshared edges (Table 3.6). The octahedra are distorted, but the degree of distortion appears only slightly affected by the Na substitution.

Table 3.5. Atomic coordinates and thermal parameters U (\AA^2) of the two single-crystals studied in this work. Standard deviations are in parentheses.

		S3356	H2495
K	x, y	0.0	0.0
	z	0.5	0.5
	U_{eq}	0.0116 (1)	0.0119 (1)
	occupancy X_{K}	0.960 (3)	0.800 (1)
	occupancy X_{Na}	==	0.074 (6)
Si/Al	x	0.35016 (2)	0.35028 (3)
	y	0.16581 (2)	0.16606 (3)
	z	0.0	0.0
	U_{eq}	0.00466 (7)	0.00463 (8)
	occupancy X_{Si}	0.75 (fixed)	0.75 (fixed)
	occupancy X_{Al}	0.25 (fixed)	0.25 (fixed)
O1	x	0.15450 (7)	0.15428 (7)
	y	0.20412 (7)	0.20359 (7)
	z	0.0	0.0
	U_{eq}	0.0068 (1)	0.0068 (1)
O2	x	0.54127 (7)	0.54145 (7)
	y	0.16436 (6)	0.16430 (7)
	z	0.0	0.0
	U_{eq}	0.0069 (1)	0.0068 (1)

Note: for sample H245 a split site Na1 has been introduced with coordinate -0.0132, 0.062, 0.5; with isotropic temperature factor 0.021 (4) and with occupancy $X_{\text{Na}} = 0.124$ (1).

Table 3.6. Bond distances and bond angles of the single-crystals studied in this work. Standard deviations are in parentheses.

Parameter	S3356	H2495
KO₈ polyhedron		
K-O1 [x 8]	2.7482 (6)	2.7429 (6)
O1-K-O1 [x 8]	75.76 (1)	75.73 (1)
O1-K-O1 (x 4)	60.27 (1)	59.52 (1)
Si(Al) octahedron		
Si(Al)-O1a	1.8585 (7)	1.8602 (7)
Si(Al)-O1b [x 2]	1.8248 (6)	1.8254 (5)
Si(Al)-O2a	1.7817 (7)	1.7821 (7)
Si(Al)-O2b [x 2]	1.7955 (6)	1.7949 (5)
<Si(Al)-O>	1.819	1.814
V (Å ³)	7.807 (6)	7.817 (4)
O1a...O1b [x 2]	2.400 (1)	2.406 (1)
O1b...O2b [x 2]	2.375 (1)	2.378 (1)
O2a...O1b [x 2]	2.5868 (8)	2.5883 (8)
O2a...O2b [x 2]	2.6170 (8)	2.6160 (8)
O1a...O2b [x 2]	2.6483 (8)	2.6454 (8)
O1b...O1b	2.726 (1)	2.723 (1)
O2b...O2b	2.726 (1)	2.723 (1)
O1b-Si(Al)-O1b	96.65 (3)	96.48 (3)
O1a-Si(Al)-O1b [x 2]	81.31 (3)	81.48 (3)
O2b-Si(Al)-O2b	98.77 (4)	98.68 (4)
O2a-Si(Al)-O2b [x 2]	94.04 (3)	94.00 (3)
O1a-Si(Al)-O2a	169.36 (3)	169.69 (3)
O1a-Si(Al)-O2b [x 2]	92.88 (2)	92.72 (3)
O1b-Si(Al)-O2a [x 2]	91.65 (3)	91.69 (3)
O1b-Si(Al)-O2b [x 2]	82.00 (3)	82.13 (2)
O1b-Si(Al)-O2b	174.18 (3)	174.18 (3)
Si(Al)-O1-Si(Al) edge sharing O1a-O1b	98.69 (3)	98.52 (3)
Si(Al)-O1-Si(Al) edge sharing O1b-O2b	96.55 (4)	96.48 (3)
Si(Al)-O2-Si(Al) edge sharing O1b-O2b	98.77 (4)	98.68 (4)
Si(Al)-O2-Si(Al) corner sharing	130.33 (2)	130.38 (2)

Note: the unit of bond length is in Å and the unit of bond angle is in degree. Bracketed figures represent multiplicity.

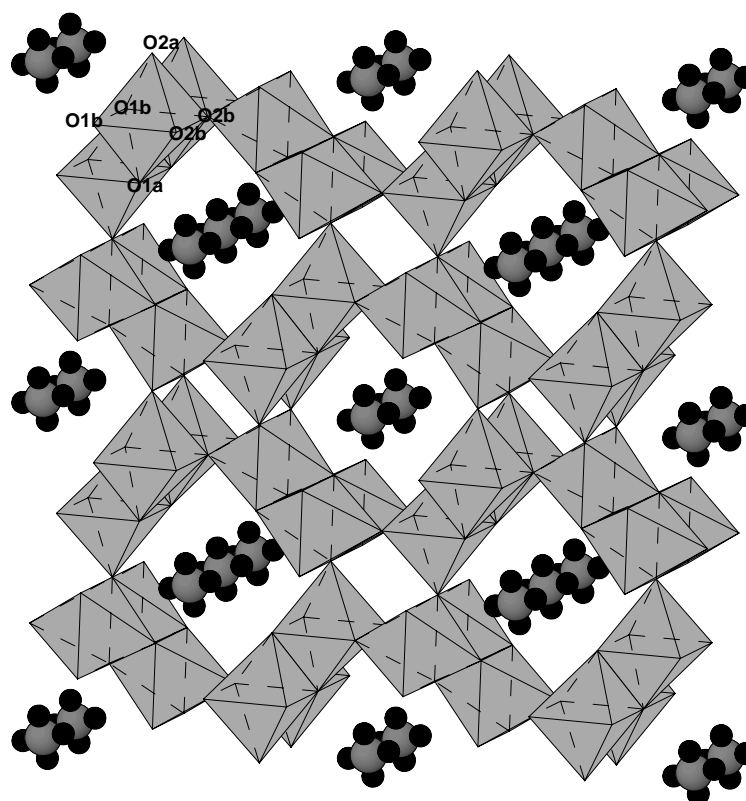


Figure 3.8. $\text{K}_{0.8}\text{Na}_{0.2}\text{AlSi}_3\text{O}_8$ crystal structure from the structural refinements performed in this study.

The framework consists of distorted Si(Al)O_6 octahedra. The split site at about 0.6 \AA from the position at the centre of the tunnels is occupied by Na (black atoms).

The major difference between the KAlSi_3O_8 hollandite end-member and the $\text{K}_{0.8}\text{Na}_{0.2}\text{AlSi}_3\text{O}_8$ sample is the presence in the latter of a split site away from the 4-fold axis. This position, occupied by $\sim 75\%$ of the total Na content, is closer to the framework walls and has a very distorted coordination polyhedra with only 5 Na1-O bond distances between 2.3 and 2.6 \AA whereas all other Na1-O bond distances are larger than 3 \AA .

3.2 High pressure and high temperature behaviour of LiF

High pressure and high temperature synchrotron radiation X-ray powder diffraction data were collected at the European synchrotron Radiation Facility (ESRF, Grenoble, France) on beam line ID-27, with a focused monochromatic beam (wave length = 0.26472 Å, size 5 × 10 μm) and a Mar CCD detector. The detector-to-sample distance was about 350 mm. We used a BGI-designed four-pin diamond anvil cell (Dubrovinskaia, 2003; Dubrovinsky, 2004). Gem-quality diamonds with culets of 300 μm were mounted in the cells. A rhenium gasket with an initial thickness of 250 μm was pre-indented to ~ 40 - 50 μm and drilled to a diameter of 200 μm. LiF and NaF powder were packed into the hole on the gasket. A piece of Au wire with 99.99% purity and 5 μm in diameter was placed near the center of the pressure chamber, as the internal pressure standard. During high temperature measurements, samples were heated by an external heater attached to the DAC. Temperatures were measured by a pair of S-type thermocouples. The samples were compressed at room temperature up to 32 GPa, and then slowly heated to ~700 °C with some adjustments of pressure. After reaching 720 °C and 20 GPa, the samples were then decompressed to ambient pressure at the same temperature. After each adjustment of pressure and temperature, the data were collected in two different areas one with and one without Au, in order to obtain diffraction patterns with and without Au reflections. The diffraction images were integrated using the Fit2d software, and the lattice parameters were determined by full profile refinements of the diffraction patterns using the GSAS package (Larson and Von Dreele, 1994) and EXPGUI interface (Toby, 2001). Equation of state and thermal expansivity were calculated with a Birch-Murnaghan equation of state using the software Eosfit52 written by R. Angel (2001), and the results are listed in Table 3.7. The obtained K_0 and α_0 values are slightly larger than previously reported by Yagi (1978). Figure 3.9 illustrates some of the experimental data plotted on the calculated isothermal curves.

Table 3.7. Equation of state and thermal expansivity parameters.

	V_0 (Å ³)	K_0 (GPa)	K'	α_0 (×10 ⁻⁴)	dK/dT (GPa/K)
At room T	65.61 (3)	74.4 (8)	3.69 (7)		
At high T	65.65 (10)	72 (2)	3.9 (2)	1.05 (3)	-0.025 (2)

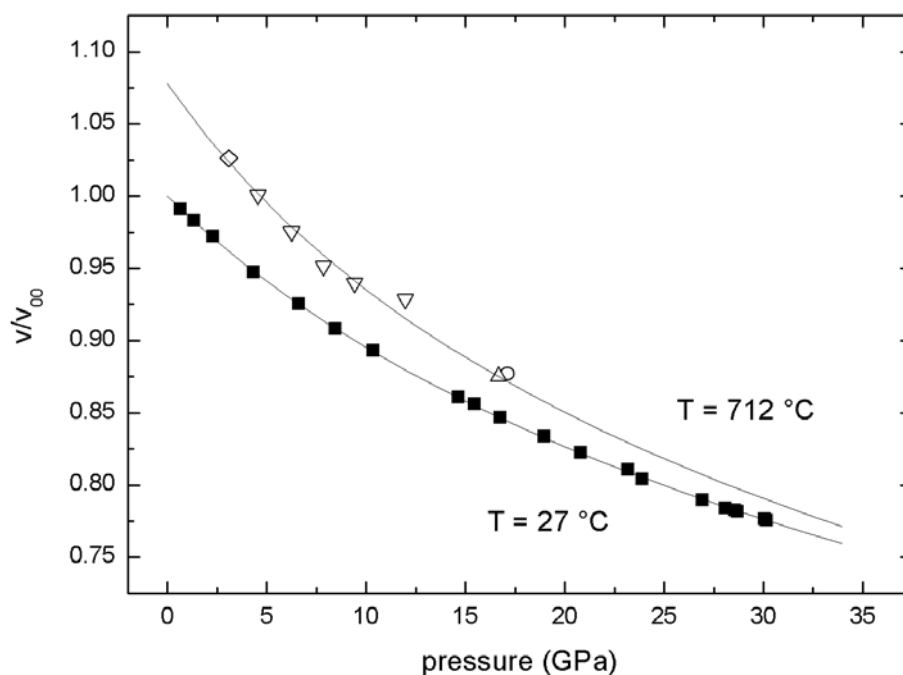


Figure 3.9. Isothermal compressions of LiF at 27 °C and 712 °C. The solid squares indicate data collected at 27 °C, open symbols are data collected at ~ 712 °C. The solid lines are the resulting third order Birch-Murnaghan equations of state fits to the data.

3.3 High pressure behaviour of $\text{K}_{0.8}\text{Na}_{0.2}\text{AlSi}_3\text{O}_8$ hollandite in helium as pressure transmitting medium

3.3.1 Unit-cell lattice parameter determination at room T

High pressure synchrotron radiation X-ray powder diffraction data were collected at the European synchrotron Radiation Facility (ESRF, Grenoble, France) on beam line ID-27, with a focused monochromatic beam (wave length = 0.26472 Å, size is $5 \times 10 \mu\text{m}$) and a Mar CCD detector. A membrane diamond cell provided by ESRF was used for this experiment. $\text{K}_{0.8}\text{Na}_{0.2}\text{AlSi}_3\text{O}_8$ hollandite powder was loaded into the hole on the gasket. We used ruby as the internal pressure standard and helium as pressure transmitting medium. The sample was compressed at room temperature up to ~ 30 GPa and then slowly decompressed to ambient

pressure. During compression, at ~ 18 GPa we observed peak splitting, and in order to confirm the phase transformation boundary, we slowly decompressed back to ~ 16 GPa and then started to compress again. The phase transformation of $\text{K}_{0.8}\text{Na}_{0.2}\text{AlSi}_3\text{O}_8$ hollandite from tetrahedral to monoclinic structure happened at about 17.5 GPa at room temperature. The monoclinic phase was stable up to the maximum pressure reached (~ 30 GPa). Typical 2-D images collected at low and high pressures are shown in Figure 3.10, whereas the correspondent integrated 1-D X-ray diffraction pattern are shown in Figure 3.11.

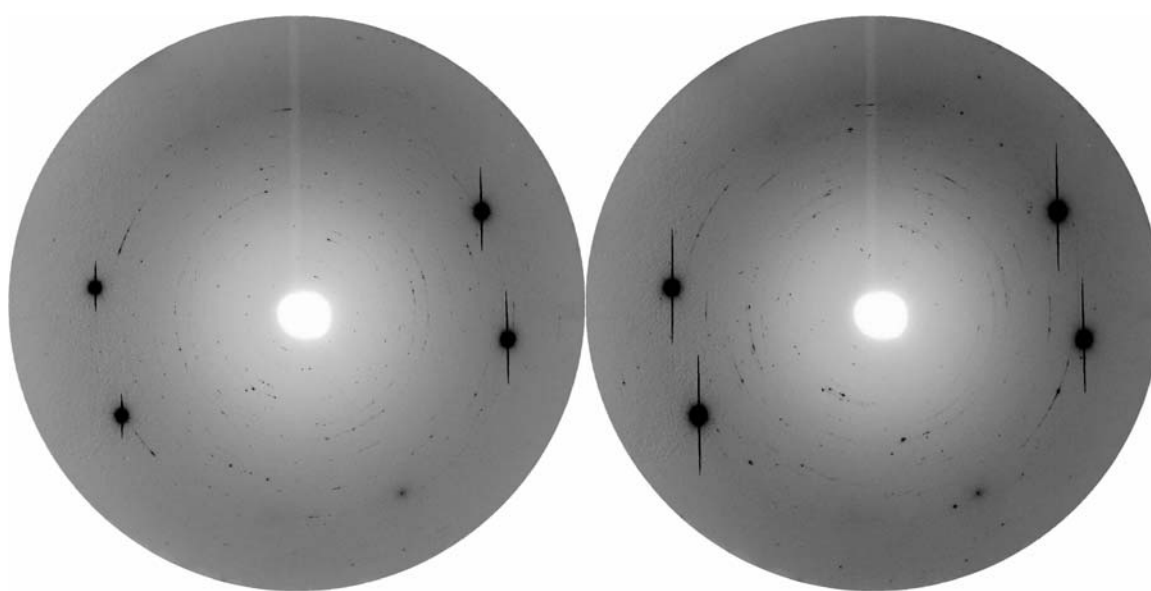


Figure 3.10. Typical 2-D diffraction patterns collected at pressure of 3.1 GPa (left, tetragonal phase) and at 26.5 GPa (right, monoclinic phase). Note that the very strong diffraction spots are due to the diamonds.

The diffraction rings appear very spotty due to the very small beam size (just few μm) with respect to the powder grain size. We preferred, however, to avoid further grinding of the material, since high-pressure phases are known to amorphise or to dissociate during this procedure. Splitting of several diffraction lines are clearly visible at high pressures, due to the tetragonal $I4/m$ to monoclinic $I2/m$ high-pressure phase transformation, which was first reported for the KAlSi_3O_8 hollandite end-member (Ferroir et al. 2006). This splitting increases with pressure as shown in Figure 3.12 for the (200) reflection.

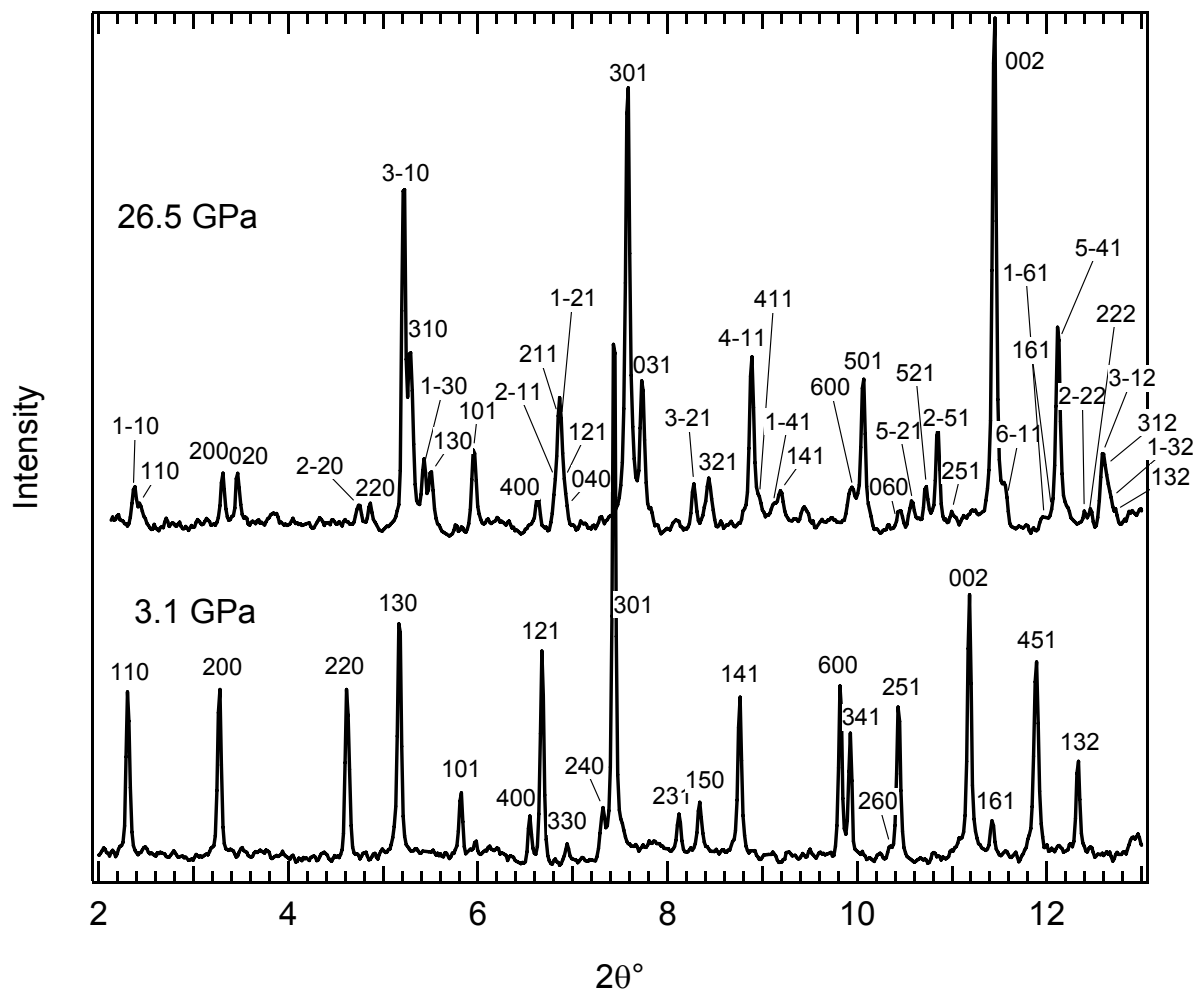


Figure 3.11. Integrated 1-D X-ray diffraction patterns at pressures of 3.1 GPa (tetragonal phase) and 26.5 GPa (monoclinic phase). Note the splitting of several diffraction lines due to the tetragonal to monoclinic phase transformation.

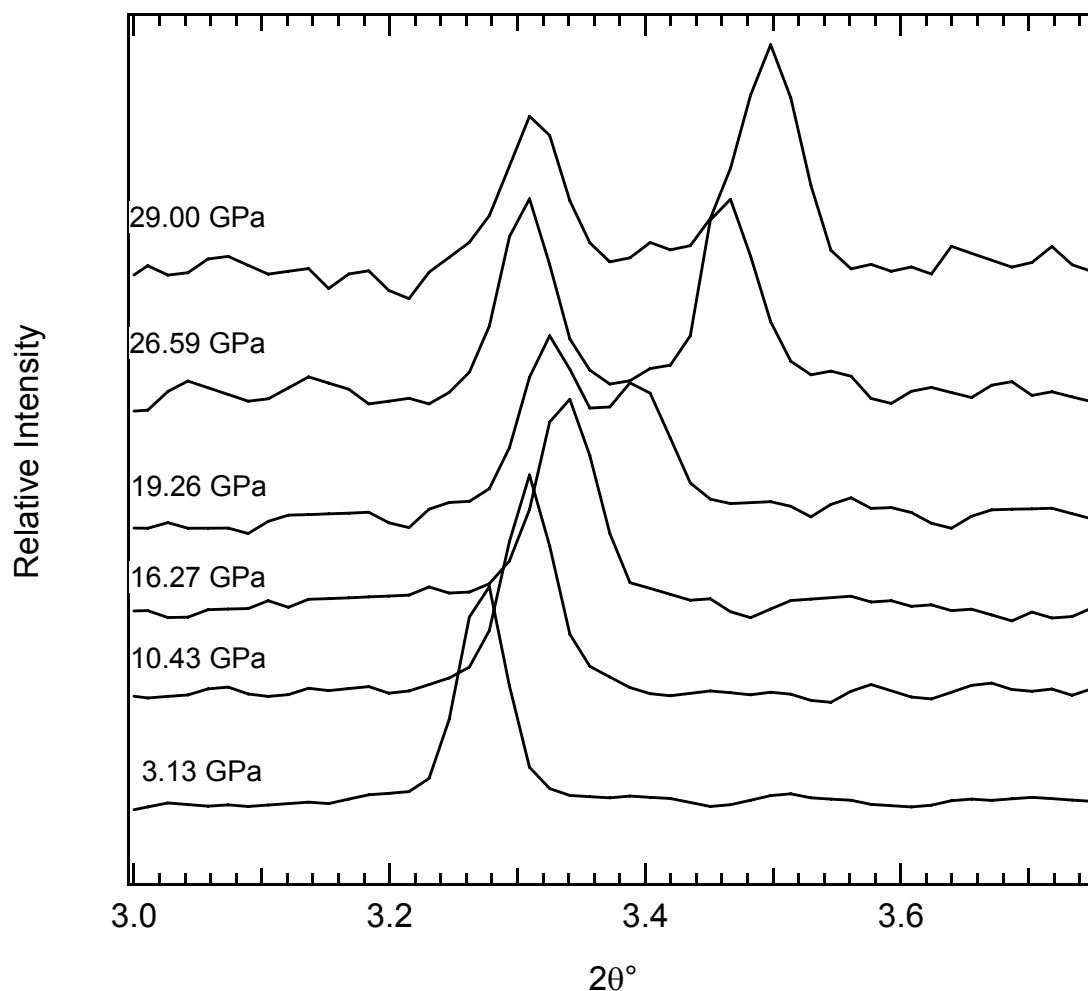


Figure 3.12. Splitting of the (200) reflection due to the tetragonal to monoclinic phase transformation at high pressure.

In order to keep the group subgroup relationship between the tetragonal and monoclinic phase, we use the monoclinic cell $I2/m$ with the c axis unique, instead of using the preferred setting of b unique reported for several hollandite structures (Post et al. 1982; Cheary 1986). In this way the tunnels are still parallel to the c axis and it is possible to compare directly the unit-cell lattice parameters of the two phases. The unit-cell lattice parameters obtained from the Rietveld refinements of the several diffraction patterns collected at different pressures are listed in Table 3.8 for both tetragonal and monoclinic $K_{0.8}Na_{0.2}AlSi_3O_8$ hollandite, and are illustrated in Figure 3.13.

The tetragonal to monoclinic phase transformation is characterized by a clear splitting of the a tetragonal axis into the a and b monoclinic axis and by a continuous increase of the angle γ . No discontinuity appears in the evolution of the c axis and unit-cell volume with pressure. Note that the uncertainties on the unit-cell lattice parameters are normally underestimated by the GSAS program. A better way to evaluate them is represented by the scatter of the data.

Table 3.8. Unit-cell lattice parameters of tetragonal and monoclinic $\text{K}_{0.8}\text{Na}_{0.2}\text{AlSi}_3\text{O}_8$ hollandite at different pressures up to ~ 30 GPa. Standard deviations are in parentheses.

Runs	Pressure (GPa)	a (Å)	b (Å)	c (Å)	γ (°)	V (Å ³)
TEST2_018	9.8	9.1640 (6)		2.6987 (2)	90	226.64 (3)
He2_020	11.1	9.1486 (7)		2.6937 (3)	90	225.45 (3)
He2_022	12.5	9.1280 (6)		2.6894 (3)	90	224.08 (3)
He2_023	13.2	9.1147 (8)		2.6898 (4)	90	223.46 (3)
He2_026	14.6	9.0990 (4)		2.6851 (2)	90	222.31 (2)
He2_028	16.3	9.0882 (7)		2.6811 (3)	90	221.45 (3)
He2_030	16.5	9.0769 (7)		2.6815 (3)	90	220.92 (3)
He2_036	19.3	9.1372 (10)	8.9220 (12)	2.6743 (3)	90.470 (11)	218.01 (4)
He2_037	18.5	9.1265 (10)	8.9857 (12)	2.6754 (2)	90.528 (14)	219.39 (4)
He2_038	17.5	9.0988 (11)	9.0259 (12)	2.6787 (3)	90.273 (12)	219.98 (3)
He2_039	17.0	9.0731 (10)		2.6786 (3)	90	220.51 (4)
He2_040	21.0	9.1376 (14)	8.8809 (9)	2.6682 (2)	90.795 (11)	216.50 (4)
He2_041	24.0	9.1505 (8)	8.8089 (9)	2.6613 (1)	91.316 (10)	214.46 (3)
He2_042	26.6	9.1604 (7)	8.7441 (12)	2.6544 (1)	91.576 (8)	212.54 (3)
He2_043	26.6	9.1668 (9)	8.7377 (12)	2.6542 (1)	91.477 (12)	212.52 (4)
He2_044	26.6	9.1622 (90)	8.741 (12)	2.6544 (2)	91.510 (13)	212.51 (4)
He2_046	29.0	9.1721 (12)	8.6817 (14)	2.6472 (10)	91.553 (14)	210.71 (4)
He2_048	29.3	9.1778 (13)	8.6585 (10)	2.6451 (8)	91.767 (13)	210.10 (3)
He2_049	23.2	9.1666 (13)	8.8009 (14)	2.6607 (1)	91.296 (14)	214.59 (4)
He2_050	13.2	9.1277 (6)		2.6888 (2)	90	224.02 (3)
He2_51	10.4	9.1581 (4)		2.6966 (2)	90	226.16 (2)
He2_052	8.2	9.1957 (6)		2.7035 (2)	90	228.61 (3)
He2_053	5.6	9.2353 (4)		2.7098 (1)	90	231.12 (2)
He2_054	3.1	9.2768 (5)		2.7168 (1)	90	233.80 (2)
He2_055	0.7	9.3180 (5)		2.7244 (1)	90	236.54 (2)

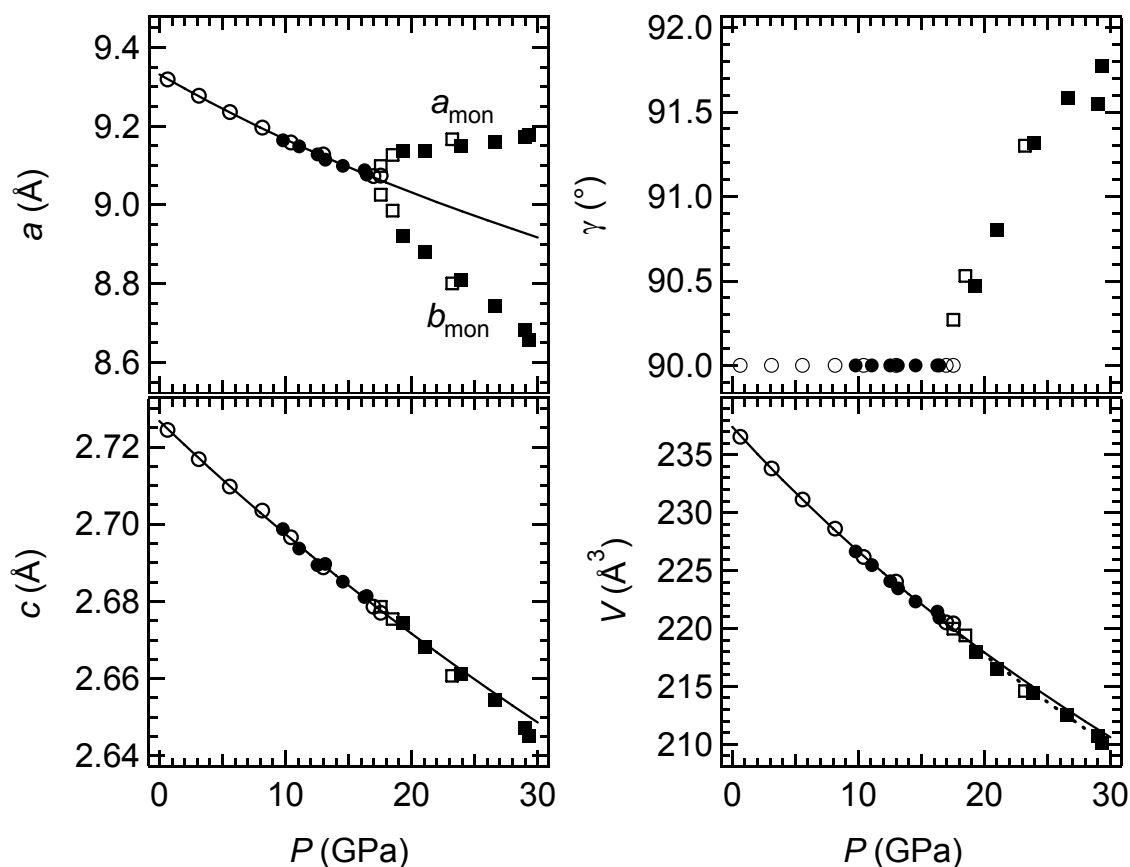


Figure 3.13. Unit-cell lattice parameters changes with pressure. At about 17.5 GPa, the tetragonal $\text{K}_{0.8}\text{Na}_{0.2}\text{AlSi}_3\text{O}_8$ hollandite transforms to monoclinic (hollandite II). Filled and open circles are data of the tetragonal phase in compression and decompression, respectively; solid and open squares are data of the monoclinic phase in compression and in decompression, respectively. Solid curves are second order Birch-Murnaghan EoS fits through the tetragonal data. Dotted curve is a second order Birch-Murnaghan EoS fit of the volume of the monoclinic phase.

3.3.2 Equation of state

P - V and P - V - T equations of state were calculated with the Birch-Murnaghan expression using the software Eosfit52 written by Ross Angel (2001).

An equation of state, EoS, is a relationship between the volume (or density) of a phase and pressure, temperature, or any other relevant intensive thermodynamic variable. Diffraction

experiments at high pressure provide measurement of the variation of the unit-cell parameters of a material with pressure. The variation of the volume of a solid with pressure is characterized by the bulk modulus, defined as $K = -V\partial P/\partial V$. Measured equation of states are usually parameterized in terms of the values of the bulk modulus and its pressure derivatives, $K' = \partial K/\partial P$ and $K'' = \partial^2 K/\partial P^2$, evaluated at zero pressure. Angel (2000) presented the methods by which the parameters of EoS can be obtained from experimental compression data, and the diagnostic tools by which the quality of the results can be assessed.

The derivation of EoS for solids is dealt with in detail in a number of recent texts (e.g. Andersen 1995; Duffy and Wang 1998; Angel 2000). EoS are stress – strain relationships, where stress is the applied pressure change, ΔP , and the resulting strain is the fractional volume change $\Delta V/V$. Finite strain EoS are based upon the assumption (e.g. Birch 1947) that the strain energy of a solid undergoing compression can be expressed as a Taylor series in the finite strain, f . The Birch-Murnaghan EoS (Birch 1947) is based upon the Eulerian strain, $f_E = [(V_0/V)^{2/3} - 1]/2$. Expansion to fourth order in the strain yields the following EoS:

$$P = 3K_0 f_E (1 + 2f_E)^{5/2} \left\{ 1 + 3/2(K' - 4)f_E + 3/2[K_0 K'' + (K' - 4)(K' - 3) + 35/9]f_E^2 \right\} \quad (1)$$

If this EoS is truncated at second order in the energy, then the coefficients of f_E must be identical to zero, which requires that K' has the fixed value of 4 (higher order terms are ignored). The 3rd-order truncation, in which the coefficient of f_E^2 is set to zero yields a three-parameter EoS (with V_0 , K_0 and K') with an implied value of K'' given by (Anderson 1995):

$$K'' = \frac{-1}{K_0} [(3 - K')(4 - K') + 35/9]$$

The Birch-Murnaghan EOS parameters have been calculated for the tetragonal and the monoclinic phases of $K_{0.8}Na_{0.2}AlSi_3O_8$ hollandite assuming $K' = 4$ and are the following: $V_0 = 237.4$ (2) \AA^3 , $K_0 = 197$ (3) GPa for the tetragonal phase and $V_0 = 239.4$ (9) \AA^3 , $K_0 = 174$ (7) GPa for the monoclinic phase. These EoS are reported in Figure 3.12 as solid and dotted curves. A linearised Birch-Murnaghan EoS (implemented in the Eosfit52 software) in which

the cube of the unit-cell axes is substituted for the volume in equation (1) has been used to fit the variation of the unit-cell a and c parameters of the tetragonal $K_{0.8}Na_{0.2}AlSi_3O_8$ hollandite. The K_0 values so obtained are then one-third of the inverse of the zero-pressure linear compressibility β_0 of the axes, defined as $\beta_0 = \frac{1}{l_0} \left(\frac{\partial l}{\partial P} \right)_{P=0}$ in which l_0 is the length of the unit-cell axis at room P. The resulting linearised Birch-Murnaghan EoS parameters obtained assuming $K' = 4$ are the following: $a_0 = 9.331$ (3) Å, and $K_0 = 168$ (3) GPa for the a axis, and $c_0 = 2.7264$ (2) Å, and $K_0 = 292$ (3) GPa for the c axis. The linear compressibility of the $K_{0.8}Na_{0.2}AlSi_3O_8$ hollandite structure is clearly anisotropic, with the a axis much more compressible than the c axis.

3.3.2.1 The f - F plot

The precision with which volumes and pressures can be measured means that it is very difficult to obtain a useful visual assessment of the quality of a EoS from a direct plot of volume against pressure. Nor do P - V plots provide a visual indication of which higher order terms such as K' and K'' might be significant in an EoS. Such a visual diagnostic tool is provided by the f - F plot, which can be applied to any isothermal EoS based upon finite strain. For the Birch-Murnaghan EoS, based upon the Eulerian definition of finite strain f_E , a 'normalized stress' is defined as $F_E = P / [3f(2f+1)^{5/2}]$, and the EoS (Eqn. 1) can be re-written as a polynomial in the strain (e.g. Stacey et al. 1981):

$$F_E = K_0 + 3K_2 / 2(K_0' - 4)f_E + 3K_0 / 2[K_0K'' + (K_0' - 4)(K_0' - 3) + 35/9]f_E^2 + \dots \quad (2)$$

If the P , V data are transformed into f_E and F_E and F_E is plotted vs f_E a direct indication of the compressional behaviour of the material is obtained. If the data points all lie on a horizontal line of constant F then $K_0' = 4$, and the data can be fitted with a 2nd-order truncation of the Birch-Murnaghan EoS. If the data points can be fitted by an inclined straight line, a 3rd-order Birch-Murnaghan EoS is necessary to describe the P - V data and an estimate of the value of K' is given by the slope which is equal to $3K_0(K_0' - 4)/2$. In the same way a parabolic curve in the f - F plot will suggest that the coefficient on f^2 in equation (2) is not zero and a 4th-order Birch-

Murnaghan EoS is required. In all cases, the intercept on the F axis can be used as an estimate of K_0 .

The f - F plot of the P - V data of $K_{0.8}Na_{0.2}AlSi_3O_8$ hollandite for both tetragonal and monoclinic phases is shown in Figure 3.14. Both sets of data can be fit reasonably well by horizontal lines confirming that a second order Birch-Murnaghan EoS ($K_0' = 4$) can satisfactorily fit the P - V data of $K_{0.8}Na_{0.2}AlSi_3O_8$ hollandite.

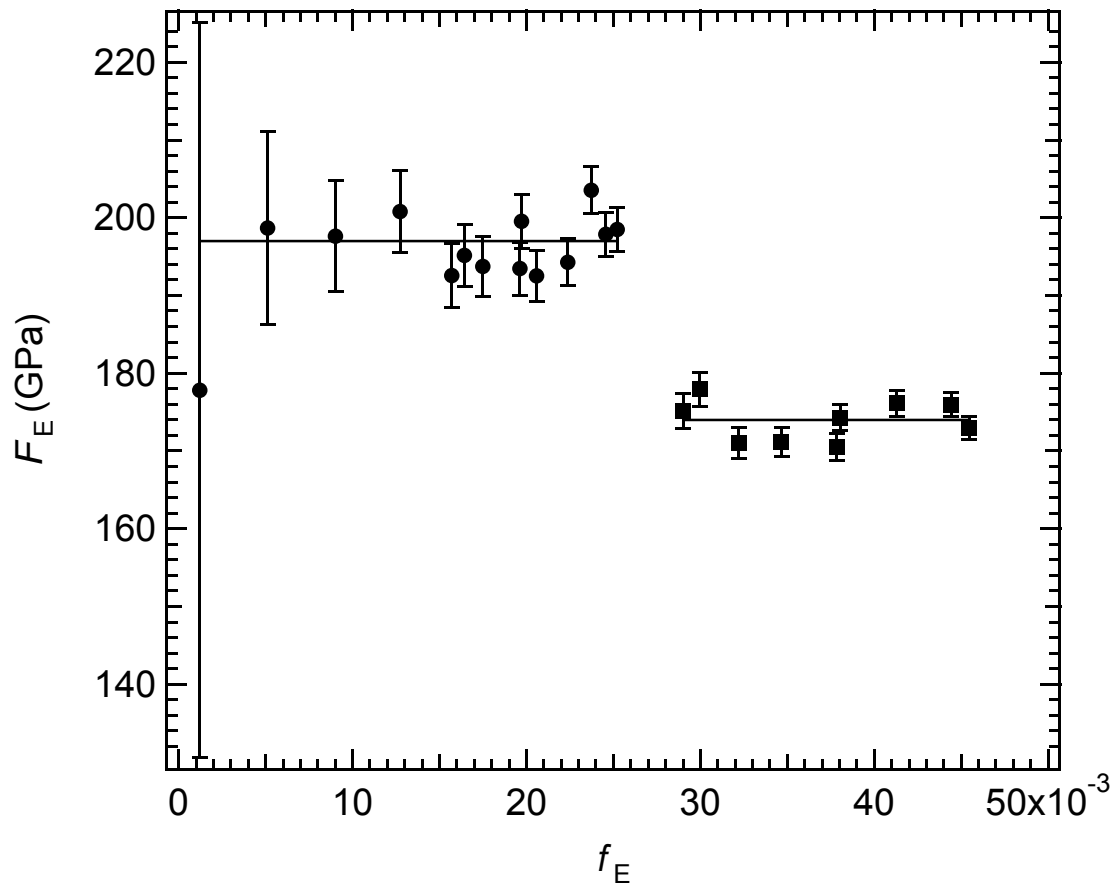


Figure 3.14. f - F plot for the P - V data of $K_{0.8}Na_{0.2}AlSi_3O_8$ hollandite calculated using $V_0 = 237.4 \text{ \AA}^3$ for the tetragonal phase (filled circles) and $V_0 = 239.4 \text{ \AA}^3$ for the monoclinic phase (filled squares). The horizontal fit of the data is consistent with a $K_0' = 4$. The intercepts on the F axis are in excellent agreement with the K_0 values obtained with the Eosfit52 program.

The linearised f - F plots calculated for the tetragonal unit-cell a and c axes are shown in Figure 3.15. Again the data can be described by horizontal lines confirming that a second order

Birch-Murnaghan EoS is sufficient for the fitting of the variation with pressure of the unit-cell axes.

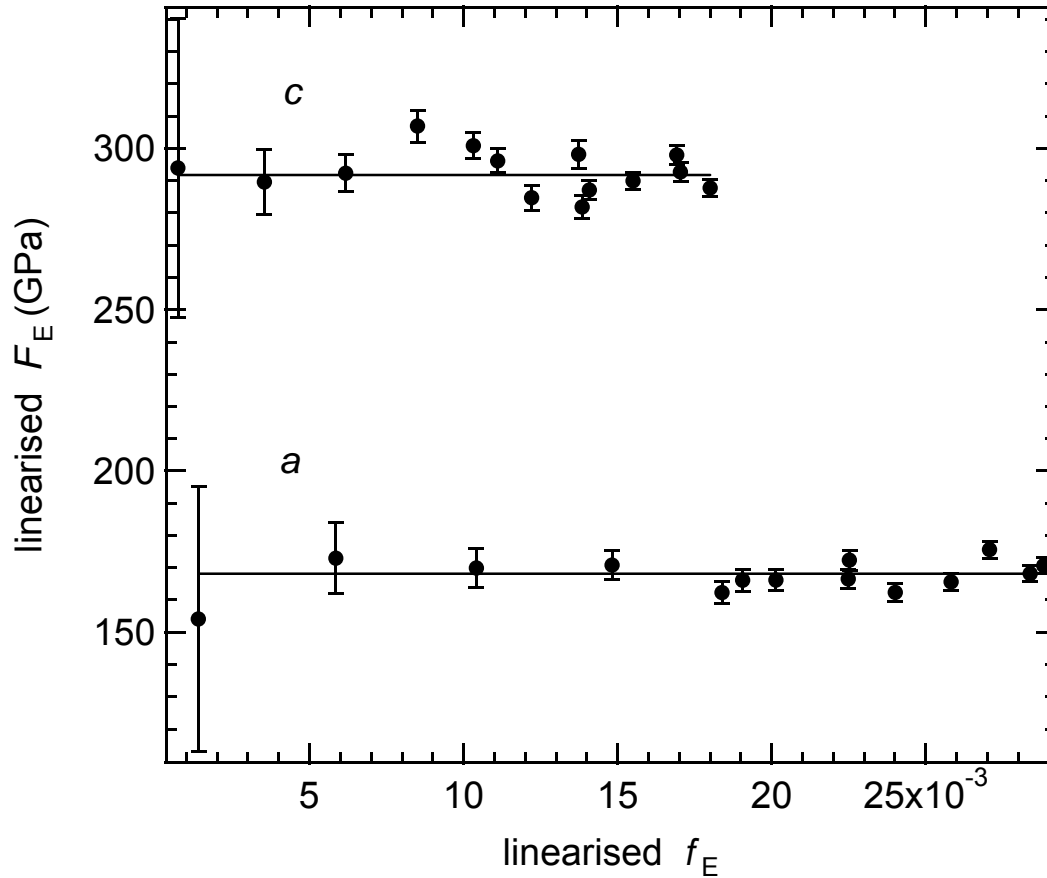


Figure 3.15. Linearised f - F plots for the tetragonal unit-cell axes of $K_{0.8}Na_{0.2}AlSi_3O_8$ hollandite calculated using $a_0 = 9.331 \text{ \AA}$ and $c_0 = 2.7264 \text{ \AA}$. The horizontal fit of the data is consistent with a $K_0' = 4$. The intercepts on the F axis are in excellent agreement with the K_0 values obtained with the Eosfit52 program.

3.3.3 Spontaneous strain:

Lattice parameters are geometrical properties of a crystal, but their variations at phase transitions can be formalized for thermodynamic analysis using the concept of spontaneous strain, ϵ_s , which is used to describe the distortion or lattice relaxation that accompanies a structural phase transition. In the last decades, the concept of spontaneous strain has been used to quantitative describe a number of phase transitions and a comprehensive summary of the

formal definition of spontaneous strain, its symmetry constrains and a number of examples on how it is determined from lattice parameters variations is given by Carpenter et al. (1998). In any lattice distortion accompanying a phase transition, the magnitude of ϵ_s represents a measure of the extent of transformation at a given pressure and/or temperature. For thermodynamic purposes, the extent of transformation is usually specified in terms of an order parameter, Q , which is scaled to vary between zero in the high-symmetry phase and unity in the fully transformed low-symmetry phase. In effect, the spontaneous strains provide an indirect measure of this order parameter, and the interaction between ϵ_s and Q is often described as strain/order parameter coupling.

The relationship between any spontaneous strain, ϵ_s (e in the equations), and the driving order parameter, Q , for a phase transitions in systems in which the order parameter is not itself a strain, can be included explicitly in the Landau free-energy expansion (for transition which occur as a function of temperature):

$$G(Q, e) = \frac{1}{2}a(T - T_c)Q^2 + \frac{1}{3}bQ^3 + \frac{1}{4}cQ^4 + \dots + \sum_{i,m,n} \lambda_{i,m,n} e_i^m Q^n + \frac{1}{2} \sum_{i,k} C_{ik}^0 e_i e_k \quad (3)$$

where the coefficients λ describe the coupling between Q and the strain components, e , and the last term describes elastic energies. The exponents m and n depend on the symmetry properties of both Q and e , but, in general, only one coupling term is needed to account for each strain component. Characteristic relationships are then $e \propto Q$ for symmetry-breaking strains when e and Q have the same symmetry, and $e \propto Q^2$ for all other strains. The volume strain, V_s , is generally expected to vary linearly with Q^2 .

In $K_{0.8}Na_{0.2}AlSi_3O_8$ hollandite, the tetragonal to monoclinic high-pressure phase transition is described by the group subgroup relationship $4/m$ to $2/m$. This transition is proper ferroelastic (Salje, 1993) and the order parameter follows the B_g active representation of point group $4/m$. The basic functions associated with B_g are $x^2 - y^2$ and xy . The symmetry-breaking strain is, therefore, $e_{11}x^2 - e_{22}y^2 + 2e_{12}xy = 1$, with $e_{11} = -e_{22} \neq e_{12} \neq 0$, whereas the other strain components e_{33} , e_{13} , e_{23} are non-symmetry breaking strains. The strain components for a tetragonal to monoclinic transition are defined as (Carpenter et al. 1998):

$$e_1 = e_{11} = \frac{a \sin \gamma - a_0}{a_0}$$

$$e_2 = e_{22} = \frac{b - b_0}{b_0} = \frac{b}{a_0} - 1$$

$$e_6 = 2e_{12} = \frac{a}{a_0} \cos \gamma$$

where, a , b , and γ are the lattice parameters of the monoclinic phase, and a_0 and b_0 are the lattice parameters of the tetragonal phase extrapolated into the stability field of the monoclinic phase. Strictly speaking the volume strain associated to this phase transformation should be zero in order for e_1 to be equal to e_2 , however, as is the case for real phase transformation that condition is not always true. Hence a symmetry adapted strain defined as:

$$e_1 - e_2 = \frac{a \sin \gamma - b}{a_0}$$

has been used instead, in order to exclude the volume strain from the determination of the symmetry-breaking strain components.

The symmetry-breaking strains transform as R_{active} , so that linear coupling terms, $\lambda(e_1 - e_2)Q$ and $\lambda e_6 Q$, will contribute to the excess free energy. The non-symmetry-breaking strain components are $(e_1 + e_2)$, and e_3 , e_4 and e_5 and they couple with Q^2 . The last three strain components are defined as (Carpenter et al. 1988):

$$e_3 = e_{33} = \frac{c - c_0}{c_0}$$

$$e_4 = 2e_{23} = 0$$

$$e_5 = 2e_{13} = 0$$

where c and c_0 are the unit-cell c axis of the monoclinic and of the tetragonal phase extrapolated into the stability field of the monoclinic phase, respectively.

The volume strain associated with the transition is given by:

$$V_s = \frac{V - V_0}{V_0}$$

(again, V is the cell volume of the monoclinic phase, and V_0 is the cell volume of the tetragonal phase extrapolated into the stability field of the monoclinic phase.)

and it transforms as the identity representation, i.e. its lowest-order coupling with the order parameter is $\lambda V_s Q^2$.

Extrapolations of the a and c tetragonal unit-cell axes into the stability field of the monoclinic phase are performed using the 2nd-order Birch-Murnaghan EoS (Fig. 3.12). The monoclinic c parameter hardly deviates from the extrapolation of the tetragonal c parameter, implying that the non-symmetry breaking strain e_3 is practically negligible. The a and b parameters of the monoclinic phase do not diverge symmetrically about the extrapolated value of a_0 for the tetragonal phase because there is a small volume reduction associated with the transition (Fig. 3.12). The calculated strain components e_1-e_2 , e_6 , e_1+e_2 , as well as the volume strain V_s are reported in Table 3.9. Note that both e_1+e_2 and volume strain V_s are one order of magnitude smaller than the symmetry-breaking strains, and their values are on the order of 1-2 ‰ which is the order of the uncertainties. The variation of the strains component with pressure is consistent with Q^2 being proportional to P (Fig. 3.15) and therefore with a transition being second order in character. The linear fits through the data reported in Fig. 3.16 extrapolated to zero strain give a transition pressure, P_c , of ~ 17.5 GPa.

Table 3.9. Calculated strains.

Pressure (GPa)	Strains			
	e_1-e_2	e_6	e_1+e_2	V_s
17.5	0.008031	-0.00478	-0.00015	0.000509
18.5	0.015517	-0.00929	0.00109	0.001517
19.3	0.023763	-0.00829	-0.00278	-0.00212
21.0	0.028355	-0.01406	-0.00248	-0.00254
23.2	0.040395	-0.02305	-0.00254	-0.00367
23.9	0.037743	-0.02339	-0.00167	-0.00182
26.6	0.046105	-0.02813	-0.00123	-0.00174
29.3	0.057688	-0.0317	-0.00226	-0.00425
29	0.05454	-0.02784	-0.00084	-0.00226

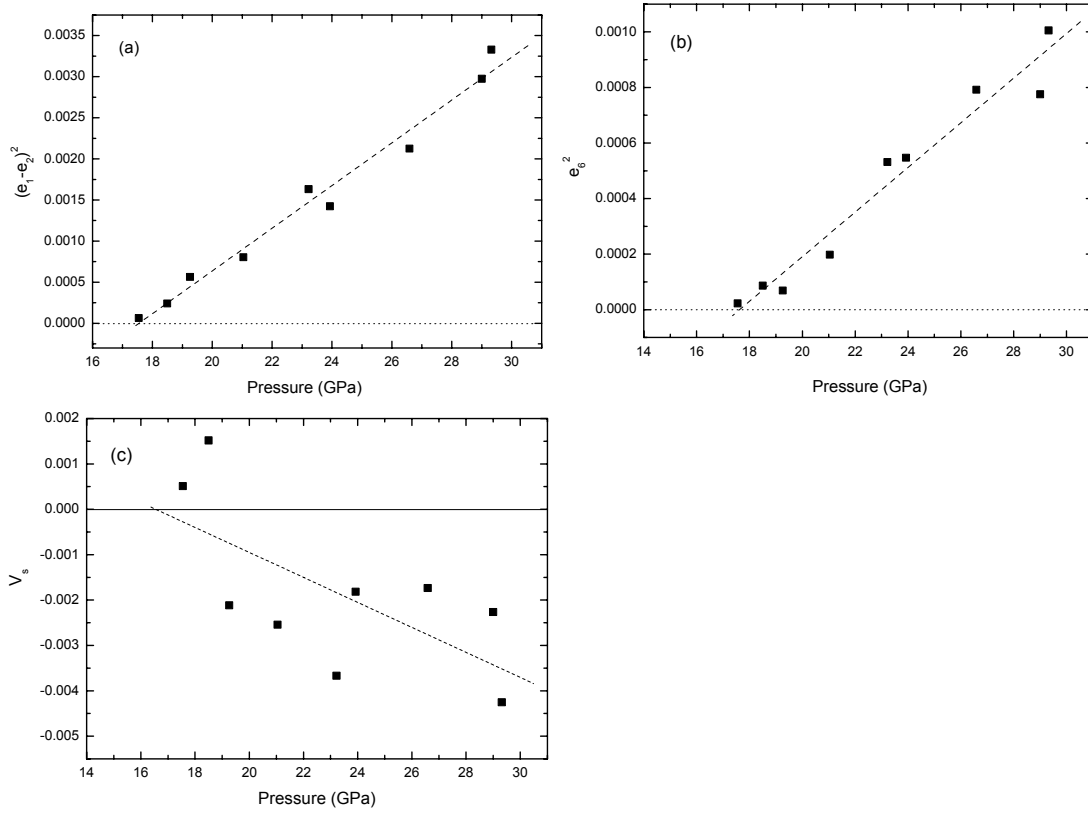


Figure 3.16. Variations as a function of pressure of a) the square of the symmetry adapted strain $e_1 - e_2$; b) the square of the symmetry-breaking strain e_6 (shear strain); and c) the volume strain V_s . Solid lines are linear fits through the data given by: $(e_1 - e_2)^2 = -0.0046(3) + 0.00026(1)P$; $e_6^2 = -0.0014(2) + 0.00008(7)P$; and $V_s = 0.005(3) - 0.0003(1)P$.

The uncertainties of the strain values are on the order of 1%.

The Landau free-energy expansion can, thus, be written as:

$$G(Q, e) = L(Q) + \lambda_1(e_1 - e_2)Q + \lambda_2 e_6 Q + \lambda_3(e_1 + e_2)Q^2$$

where $L(Q) = \frac{1}{2}a(P - P_c)Q^2 + \frac{1}{4}bQ^4$ for the high-pressure phase transition observed in this study. The elastic component

$$\frac{1}{2} \sum_{i,k} C_{ik}^0 e_i e_k = \frac{1}{4} (C_{11}^0 - C_{12}^0) (e_1 - e_2)^2 + \frac{1}{4} (C_{11}^0 + C_{12}^0) (e_1 + e_2)^2 + \frac{1}{2} C_{66}^0 e_6^2 + C_{16}^0 (e_1 - e_2) e_6$$

will be ignored given that the bare elastic constants of $\text{K}_{0.8}\text{Na}_{0.2}\text{AlSi}_3\text{O}_8$ hollandite are not known.

3.4 High pressure behaviour of $\text{K}_{0.5}\text{Na}_{0.5}\text{AlSi}_3\text{O}_8$ hollandite in helium as pressure transmitting medium

High pressure synchrotron radiation X-ray powder diffraction data were collected at the ESRF on beam line ID-27, with the same experimental conditions described in section 3.3. Ruby was used as the internal pressure standard and helium as pressure transmitting medium. Hollandite sample H2502 with composition of $\text{K}_{0.5}\text{Na}_{0.5}\text{AlSi}_3\text{O}_8$ was compressed up to 13.6 GPa at room temperature. At this pressure, unfortunately a leak in the DAC did not allowed further increases of pressure. Until 13.6 GPa no signs of phase transition were observed, and the hollandite sample remained in the tetragonal structure. The obtained lattice parameters at different pressures are listed in Table 3.10 and illustrated in Figure 3.16.

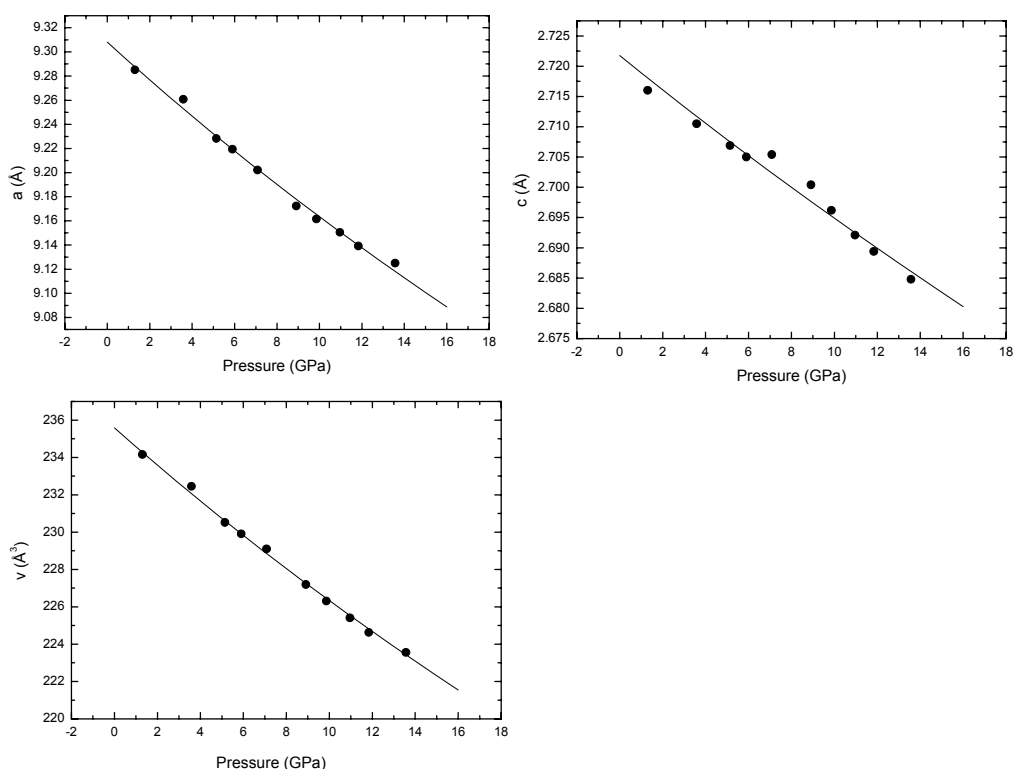


Figure 3.16. Unit-cell lattice parameters changes with pressure for the tetragonal $\text{K}_{0.5}\text{Na}_{0.5}\text{AlSi}_3\text{O}_8$ hollandite. Solid curves are 2nd-order Birch-Murnaghan EoS fits to the data.

Table 3.10. Unit-cell lattice parameters of tetragonal $\text{K}_{0.5}\text{Na}_{0.5}\text{AlSi}_3\text{O}_8$ hollandite at different pressures.

Runs	Pressure (GPa)	a (Å)	c (Å)	V (Å ³)
B-013	1.3	9.2851(4)	2.71603(23)	234.16(3)
B-023	3.6	9.2607(6)	2.7105(4)	232.45(4)
B-025	5.1	9.2282(7)	2.7069(4)	230.52(4)
B-029	5.9	9.2193(7)	2.7050(4)	229.91(4)
B-032	7.1	9.2022(12)	2.7054(5)	229.10(6)
B-034	8.9	9.1723(14)	2.7004(6)	227.19(7)
B-036	9.9	9.1616(16)	2.6962(6)	226.31(8)
B-038	11.0	9.1505(16)	2.6921(5)	225.41(7)
B-040	11.8	9.1391(16)	2.6894(4)	224.63(7)
B-042	13.7	9.1250(20)	2.6848(4)	223.56(8)

3.4.1. The equation of state

The Birch-Murnaghan EOS parameters have been calculated assuming $K' = 4$, and are the following: $V_0 = 235.6$ (1) Å³, $K_0 = 230$ (5) GPa. The Linearised Birch-Murnaghan EoS parameters obtained for the tetragonal phase assuming $K' = 4$ are: $a_0 = 9.308$ (3) Å, and $K_0 = 193$ (7) GPa for the a axis, and $c_0 = 2.723$ (2) Å, and $K_0 = 317$ (23) GPa for the c axis. Curves of the EoS fits to the data are shown in Figure 3.16.

3.5 High pressure behaviour of $\text{K}_{0.8}\text{Na}_{0.2}\text{AlSi}_3\text{O}_8$ hollandite in lithium fluoride as pressure transmitting medium

High pressure synchrotron radiation X-ray powder diffraction data were collected at ESRF on beam line ID-27, with the same experimental conditions and diamond anvil cell described in section 3.2. Hollandite sample H2495 with composition of $\text{Na}_{0.2}\text{K}_{0.8}\text{AlSi}_3\text{O}_8$ and LiF powder were packed into the hole inside the gasket. A piece of Au wire with 99.99% purity and 5 µm in diameter was placed near the center of the pressure chamber, as an internal pressure standard. The sample was compressed at room temperature up to ~ 25 GPa and then

decompressed to ambient pressure. During compression, splitting of several diffraction lines was observed at around 11 GPa, suggesting that the transition from tetragonal to monoclinic was taking place. The monoclinic phase is stable up to at least 25 GPa. The obtained 2D images were integrated using the Fit2d software, and the unit-cell lattice parameters were determined at each pressure by Rietveld full profile refinements (GSAS package). Unit-cell lattice parameters of both Au and LiF were used to determine the pressure, using the EoS of Au reported by Anderson et al. (1989) and the EoS of LiF determined in this study (section 3.2). The two pressure values so determined for each measurement are in good agreement. The lattice parameters of the tetragonal and monoclinic $\text{K}_{0.8}\text{Na}_{0.2}\text{AlSi}_3\text{O}_8$ hollandite phase at different pressures are listed in Table 3.11 and illustrated in Figure 3.17.

Table 3.11. Unit-cell lattice parameters of tetragonal and monoclinic $\text{K}_{0.8}\text{Na}_{0.2}\text{AlSi}_3\text{O}_8$ hollandite .

Runs	Pressure (GPa)	a (Å)	b (Å)	c (Å)	γ (°)	V (Å ³)
hol20_12	0.3	9.3214(8)		2.7231(3)	90	236.61(4)
hol20_14	1.2	9.3073(10)		2.7228(4)	90	235.87(5)
hol20_19	2.4	9.3000(16)		2.7172(5)	90	235.01(7)
hol20_21	4.2	9.2964(20)		2.7117(6)	90	234.35(9)
hol20_24	7.7	9.2659(33)		2.7061(9)	90	232.34(14)
hol20_27	11.5	9.3190(22)	8.9799(20)	2.6983(6)	91.261(25)	225.75(9)
hol20_35	15.6	9.3325(25)	8.8882(12)	2.7249(8)	91.853(22)	225.91(9)
hol20_37	17.2	9.3439(20)	8.8510(15)	2.7135(5)	91.953(22)	224.29(7)
hol20_39	18.8	9.3604(22)	8.8143(12)	2.7058(5)	92.144(23)	223.09(7)
Hol20_115	8.5	9.2550(23)		2.7163(8)	90	232.67(11)
hol20_117	6.8	9.2630(26)		2.7173(10)	90	233.15(12)

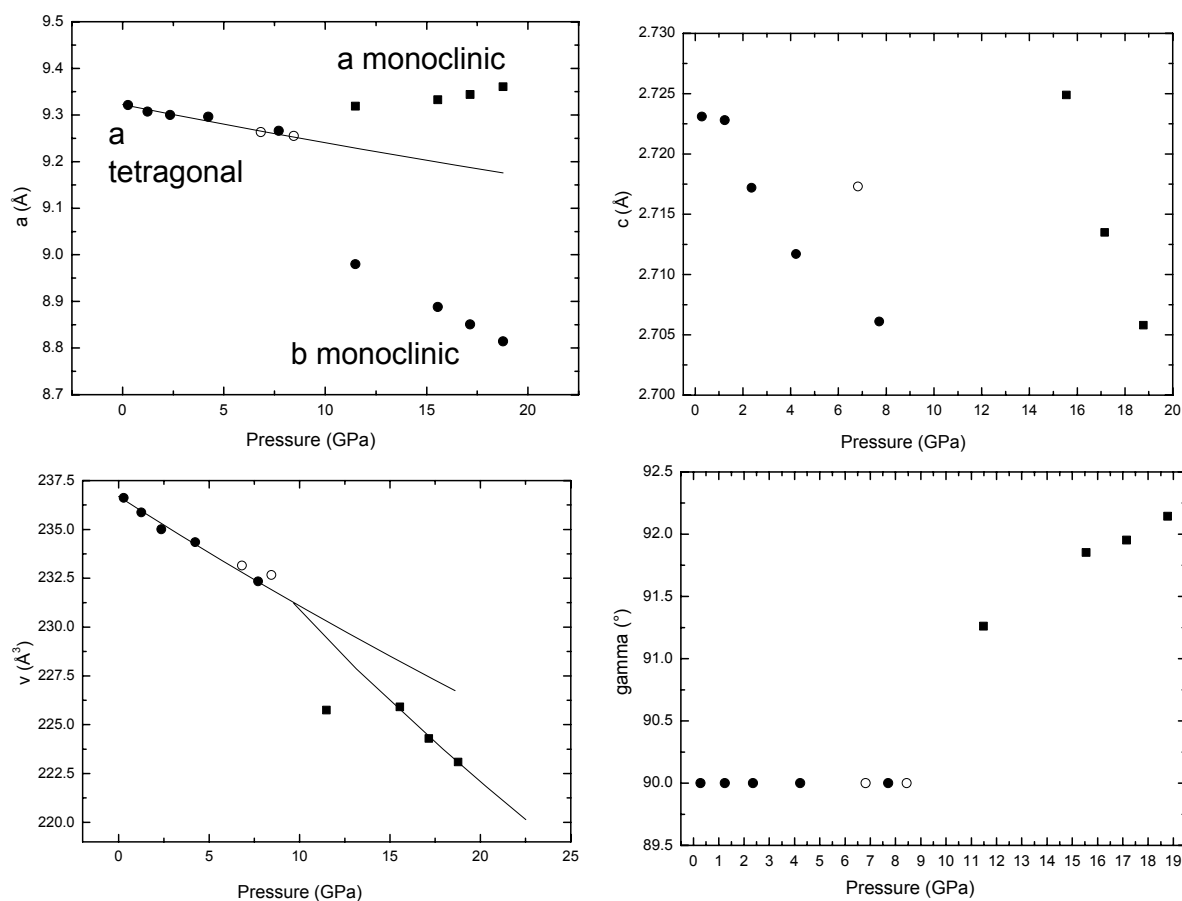


Figure 3.17. Variations of the unit-cell lattice parameters with pressure. Above 11 GPa, the phase transition of $K_{0.8}Na_{0.2}AlSi_3O_8$ hollandite to hollandite phase II with the monoclinic structure was observed. Filled and open circles are data of the tetragonal phase in compression and decompression, respectively; solid squares are data of the monoclinic phase in compression. Solid curves are 2nd – order Birch-Murnaghan EoS fits through the data.

The quasi-hydrostaticity of the experiment conducted in LiF gave rise to major broadening of the diffraction lines at high pressure, therefore the constrain on the monoclinic unit-cell are very poor, as it can be notice from the scatter of the data especially for the c axis.

3.5.1 The Equation of state

The Equation of states for the tetragonal and monoclinic P - V data of $K_{0.8}Na_{0.2}AlSi_3O_8$ hollandite were calculated with a second order Birch-Murnaghan expression ($K_0' = 4.0$) and

are listed in Table 3.12. For the monoclinic phase only three data points were used for the fitting (the data point at 11.5 was not considered). The linearised Birch-Murnaghan EoS parameters were calculated for the tetragonal phase for the a axis, also shown in Table 3.12. No EoS parameters have been calculated for the lattice parameter c , however from the variation as a function of pressure (Table 3.11), it is possible to see that the compressibility of the tetragonal hollandite structure is anisotropic also under quasi-hydrostatic conditions with the a axis much more compressible than the c axis. These results were compared with the parameters obtained from the experiments of $\text{K}_{0.8}\text{Na}_{0.2}\text{AlSi}_3\text{O}_8$ hollandite using He as pressure transmitting medium (Table 3.12). The obtained equation of state parameters for the tetragonal phase seem to be significantly affected by deviatoric stress due to the non-hydrostaticity of LiF.

Talbe 3.12 Equation of state parameters of $\text{K}_{0.8}\text{Na}_{0.2}\text{AlSi}_3\text{O}_8$ hollandite obtained from synchrotron experiments using He and LiF as pressure transmitting media.

	Tetragonal phase				Monoclinic phase	
	V_0 (\AA^3)	K_0 (GPa)	a_0 (\AA)	K_{0a} (GPa)	V_0 (\AA^3)	K_0 (GPa)
In He	237.4 (2)	197 (3)	9.331 (3)	168 (3)	239.4 (9)	174 (7)
In LiF	236.7 (1)	398 (28)	9.322 (3)	358 (48)	242 (2)	192 (23)

3.6 High pressure behaviour of $\text{K}_{0.6}\text{Na}_{0.4}\text{AlSi}_3\text{O}_8$ hollandite in lithium fluoride as pressure transmitting medium

The high pressure behaviour of hollandite sample H2353 with composition $\text{K}_{0.6}\text{Na}_{0.4}\text{AlSi}_3\text{O}_8$ was studied using both the high brilliance X-ray system at the BGI and the synchrotron radiation at the ESRF (ID-09). We used a pair of BGI-designed diamond cells, with anvils having culet diameters of 400 μm . Rhenium gasket was pre-indented and drilled to a diameter of 200 μm . The sample was loaded with lithium fluoride and a piece of ruby into the diamond anvil cell. Pressure was determined using the ruby fluorescence method and the equation of state of lithium fluoride (reported in section 3.2). At ambient temperature, the sample was

compressed up to 31 GPa and studied on the high brilliance X-ray system at the BGI. Peak splitting indicated that the tetragonal to monoclinic phase transition occurs at ~ 5 GPa. The monoclinic structure is stable at ambient temperature up to the maximum pressure reached. However, the quality of the data was too poor to constrain the unit-cell lattice parameters variation as a function of pressure. Synchrotron powder X-ray diffraction data were collected at ESRF on beam line ID-09 during decompression, with a focused monochromatic beam (wave length = 0.4121 Å). The cell was continuously rotating during data collection, in order to get average diffraction line positions and avoid scattered effect from the non-hydrostatic stresses originated from the LiF pressure transmitting medium. The images were integrated with the Fit2d software and then treated with the GSAS package. Unit-cell lattice parameters of the tetragonal and monoclinic hollandite phase determined for the decompression experiments are listed in Table 3.13 and illustrated in Figure 3.18. A clear discontinuity is visible at about 5 GPa in the plots of all unit-cell lattice parameters (Fig. 3.18).

Table 3.13. Unit-cell lattice parameters for tetragonal and monoclinic $\text{K}_{0.6}\text{Na}_{0.4}\text{AlSi}_3\text{O}_8$ hollandite determined for the decompression experiments performed at the ESRF.

Pressure (GPa)	a (Å)	b (Å)	c (Å)	γ (°)	V (Å ³)
31.0	9.2771(22)	8.6110(29)	2.6563(8)	91.861(25)	212.06(11)
28.1	9.2757(22)	8.6304(25)	2.6612(5)	92.104(22)	212.89(9)
24.3	9.2929(20)	8.6947(22)	2.6684(10)	92.012(23)	215.47(11)
22.0	9.3062(22)	8.7620(25)	2.6809(7)	91.790(24)	218.51(10)
20.5	9.3139(21)	8.7777(27)	2.6789(10)	91.73(24)9	218.91(12)
19.0	9.3297(21)	8.8117(28)	2.6882(9)	91.748(23)	220.9(11)
16.5	9.3267(19)	8.8549(25)	2.6914(8)	91.612(23)	222.19(10)
14.5	9.3293(17)	8.8910(24)	2.7015(7)	91.483(22)	224.00(9)
14.0	9.3288(18)	8.8930(27)	2.7065(8)	91.465(23)	224.45(10)
12.0	9.3338(24)	8.9250(33)	2.7115(8)	91.379(25)	225.81(12)
9.0	9.3627(15)	8.9630(28)	2.7212(8)	91.361(22)	228.29(10)
8.5	9.3639(24)	8.9650(40)	2.7202(10)	91.262(26)	228.30(14)
4.7	9.3807(23)	9.0427(30)	2.7282(11)	91.137(23)	231.38(13)
2.5	9.3103(17)		2.7184(11)	90	235.63(11)
3.0	9.3023(14)		2.7197(9)	90	235.34(9)
3.5	9.2983(8)		2.7168(5)	90	234.89(5)

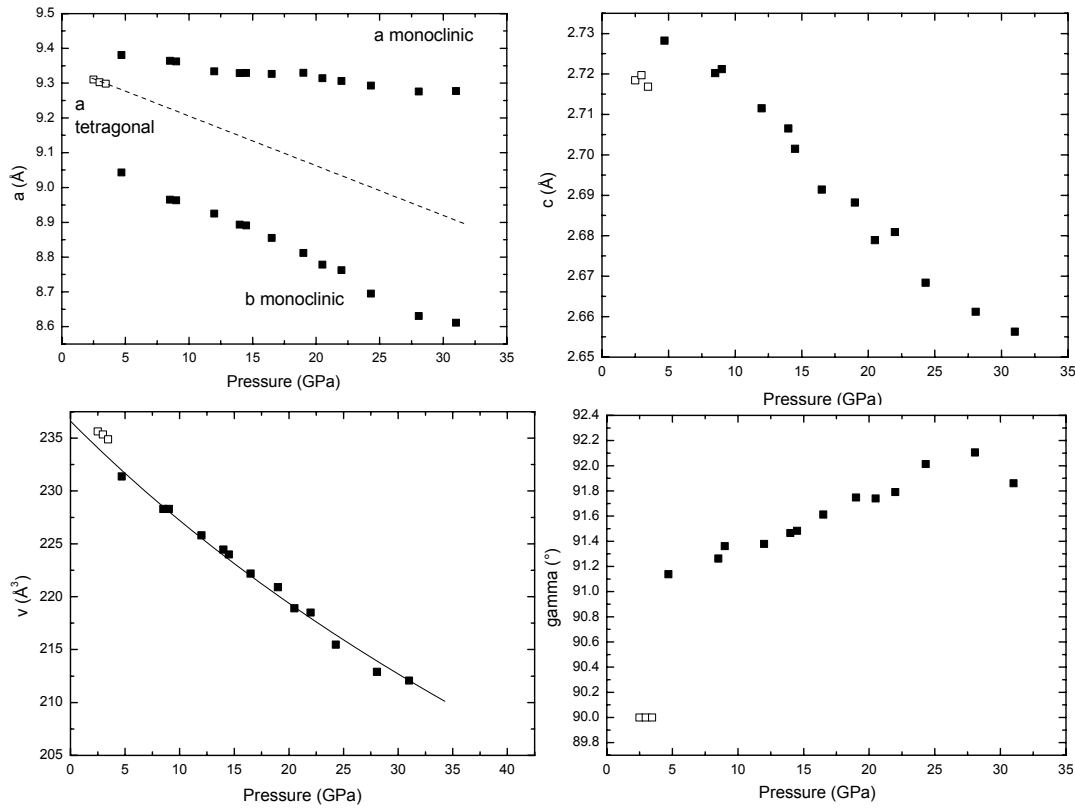


Figure 3.18. Unit-cell lattice parameters variations with pressure. At about 5 GPa, the phase transition of $K_{0.6}Na_{0.4}AlSi_3O_8$ tetragonal hollandite to hollandite phase II with monoclinic structure was observed. Open squares are data for the tetragonal phase; solid squares are data for the monoclinic phase. The dashed line is a linear fit through the tetragonal a axis. The solid curve is the 2nd – order Birch-Murnaghan EoS fit through the monoclinic volume data.

3.6.1 The Equation of state

The Equation of State was calculated with a second order Birch-Murnaghan expression (K_0' fixed to 4.0) for the P - V data of the monoclinic phase and the EoS parameters obtained are the following: $V_0 = 236.6 (3) \text{ \AA}^3$, $K_0 = 227 (8) \text{ GPa}$. For the tetragonal phase there was not enough data for EOS calculation.

3.7 High pressure high-temperature behaviour of $\text{K}_{0.5}\text{Na}_{0.5}\text{AlSi}_3\text{O}_8$ hollandite in lithium fluoride as pressure transmitting medium

High pressure synchrotron radiation X-ray powder diffraction data were collected at the ESRF on beam line ID-27. The conditions and parameters of the synchrotron X-ray and the diamond cell are as described in section 3.2. The hollandite studied in this experiment was sample H2502 with composition $\text{K}_{0.5}\text{Na}_{0.5}\text{AlSi}_3\text{O}_8$. The sample was compressed up to ~ 12 GPa at room temperature, before starting the heating procedure. At room temperature, splitting of the diffraction lines was observed at ~ 6 GPa. Once reached ~ 12 GPa, the sample was heated slowly up to ~ 800 K, then compressed at temperature up to ~ 27 GPa, and decompressed to ~ 7 GPa. The temperature was then decreased to ~ 570 K, and the cell was again compressed up to ~ 22 GPa. X-ray diffraction pattern were collected at different temperatures and pressures. Unit-cell lattice parameters of the tetragonal and monoclinic hollandite phase at different temperatures and pressures are listed in Table 3.14. The variation of the unit-cell lattice parameters at 300 K is illustrated in Figure 3.19. The variation of the unit-cell parameters at constant pressure (~ 12 GPa) and different temperatures is shown in Figure 3.20. In spite of the scatter of the data, it is possible to notice that with increasing temperature the difference between the a and b axes decreases as well as the monoclinic γ angle. The unit-cell lattice parameters measured at different temperatures are compared in Figure 3.21. At high temperature the tetragonal phase has not been recovered at any measured pressure.

Table 3.14. Unit-cell lattice parameters of tetragonal and monoclinic $\text{K}_{0.5}\text{Na}_{0.5}\text{AlSi}_3\text{O}_8$ hollandite at different pressures and temperatures.

Runs	T (K)	P (GPa)	a (Å)	b (Å)	c (Å)	γ (°)	V (Å ³)
hol50_003	300	0.9	9.2952(7)		2.7193(3)	90	234.95(4)
hol50_013	300	1.8	9.2905(10)		2.7181(5)	90	234.61(5)
hol50_015	300	2.2	9.2870(9)		2.7167(5)	90	234.31(5)
hol50_017	300	2.7	9.2835(10)		2.7157(5)	90	234.04(6)
hol50_022	300	4.9	9.2612(13)		2.7115(7)	90	232.56(7)
hol50_024	300	6.3	9.3228(19)	9.1285(16)	2.7171(5)	90.227(28)	231.23(7)
hol50_026	300	7.6	9.3126(25)	9.1006(30)	2.7073(6)	90.430(40)	229.43(11)
hol50_029	300	9.1	9.2970(18)	9.0271(26)	2.7056(5)	90.841(31)	227.04(9)
hol50_031	300	11.2	9.2867(18)	8.9595(29)	2.6959(4)	91.059(28)	224.28(9)
hol50_35	365.5	11.8	9.2091(19)	8.9562(16)	2.6981(4)	91.755(28)	222.43(7)
hol50_037	395.5	12.0	9.2379(23)	8.9601(18)	2.6979(4)	91.579(21)	223.22(8)
hol50_040	453.5	11.7	9.2388(18)	8.9865(18)	2.6993(4)	91.426(25)	224.04(7)
hol50_043	504	12.5	9.2262(18)	9.0317(28)	2.6997(6)	90.994(32)	224.93(10)
hol50_047	600	12.6	9.2109(22)	9.0463(29)	2.7011(9)	90.62(4)	225.06(11)
hol50_049	648	12.3	9.2019(27)	9.0339(25)	2.7040(6)	91.411(7)	224.71(23)
hol50_051	696	12.9	9.2270(15)	9.0930(25)	2.6998(6)	90.22(27)	226.52(9)
hol50_053	775.5	12.7	9.2290(18)	9.1(4)	2.7091(6)	91.00(33)	227.49(12)
hol50_056	783	13.7	9.2924(23)	8.902(4)	2.7085(6)	91.36(4)	223.98(12)
hol50_058	786	15.1	9.3097(29)	8.932(4)	2.7018(7)	91.21(4)	224.61(14)
hol50_060	787	19.5	9.2602(25)	8.833(5)	2.6998(6)	91.80(4)	220.72(14)
hol50_062	790	22.8	9.3402(10)	8.8319(12)	2.7025(3)	91.934(13)	222.80(5)
hol50_064	793	25.1	9.3666(14)	8.7735(14)	2.6940(4)	92.335(16)	221.21(6)
hol50_067	797	26.6	9.3735(29)	8.7560(30)	2.6910(8)	92.581(28)	220.63(12)
hol50_070	803	24.1	9.3914(22)	8.7591(18)	2.6902(4)	92.217(29)	221.13(8)
hol50_074	809	21.5	9.3531(24)	8.760(4)	2.6992(5)	91.887(26)	221.03(12)
hol50_079	809	13.9	9.3543(22)	9.0011(33)	2.7100(6)	91.350(32)	228.12(11)
hol50_081	808	11.7	9.3626(18)	9.013(4)	2.7129(4)	91.280(25)	228.87(11)
hol50_083	808	10.2	9.3546(18)	9.0776(28)	2.7175(5)	91.093(30)	230.72(9)
hol50_086	808	8.9	9.3620(21)	9.100(4)	2.7238(9)	91.02(4)	232.03(13)
hol50_088	795	7.8	9.3637(21)	9.1407(25)	2.7210(5)	90.513(35)	232.89(10)
hol50_090	719.5	7.1	9.3618(22)	9.1681(24)	2.7228(4)	90.651(27)	233.68(9)
hol50_094	619	7.3	9.3731(19)	9.1457(27)	2.7233(5)	90.895(29)	233.42(9)
hol50_097	568	7.2	9.3515(21)	9.1377(31)	2.7241(6)	90.853(33)	232.75(11)
hol50_0103	573	8.7	9.3642(19)	9.082(4)	2.7172(8)	90.93(4)	231.05(13)
hol50_0106	558	9.2	9.3214(22)	9.0798(33)	2.7159(7)	91.031(33)	229.82(12)
hol50_0109	568	10.3	9.3476(22)	9.043(5)	2.7093(8)	228.98(15)	91.06(4)
hol50_0112	570	12.1	9.3624(21)	8.995(5)	2.7066(10)	227.88(16)	91.17(4)
hol50_0114	573	13.1	9.3909(28)	8.836(4)	2.7065(5)	224.46(12)	91.86(35)
hol50_0116	573	15.0	9.3878(29)	8.831(5)	2.7035(7)	224.01(15)	91.89(4)
hol50_0119	573	18.3	9.3843(21)	8.8322(31)	2.7038(7)	223.94(11)	92.138(29)
hol50_0121	573	21.4	9.3513(20)	8.7908(34)	2.6878(4)	220.81(10)	92.021(26)

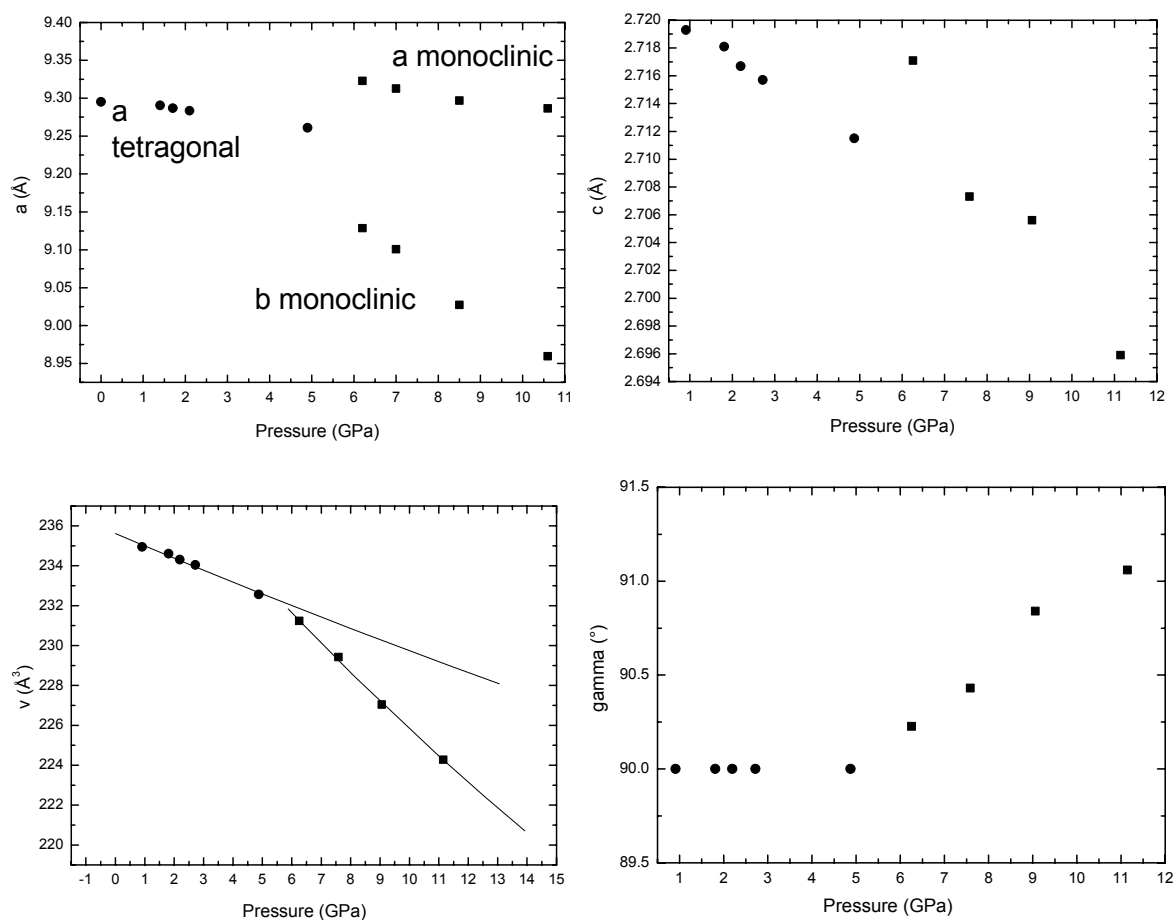


Figure 3.19. Unit-cell lattice parameters variations with pressure at room temperature. At about 6 GPa, a phase transition of $K_{0.5}Na_{0.5}AlSi_3O_8$ from tetragonal to monoclinic structure was observed. Filled circles are data for the tetragonal phase, solid squares are data for the monoclinic phase. Solid curves are 2nd-order Birch-Murnaghan EoS fits to the P - V data of the tetragonal and monoclinic hollandite.

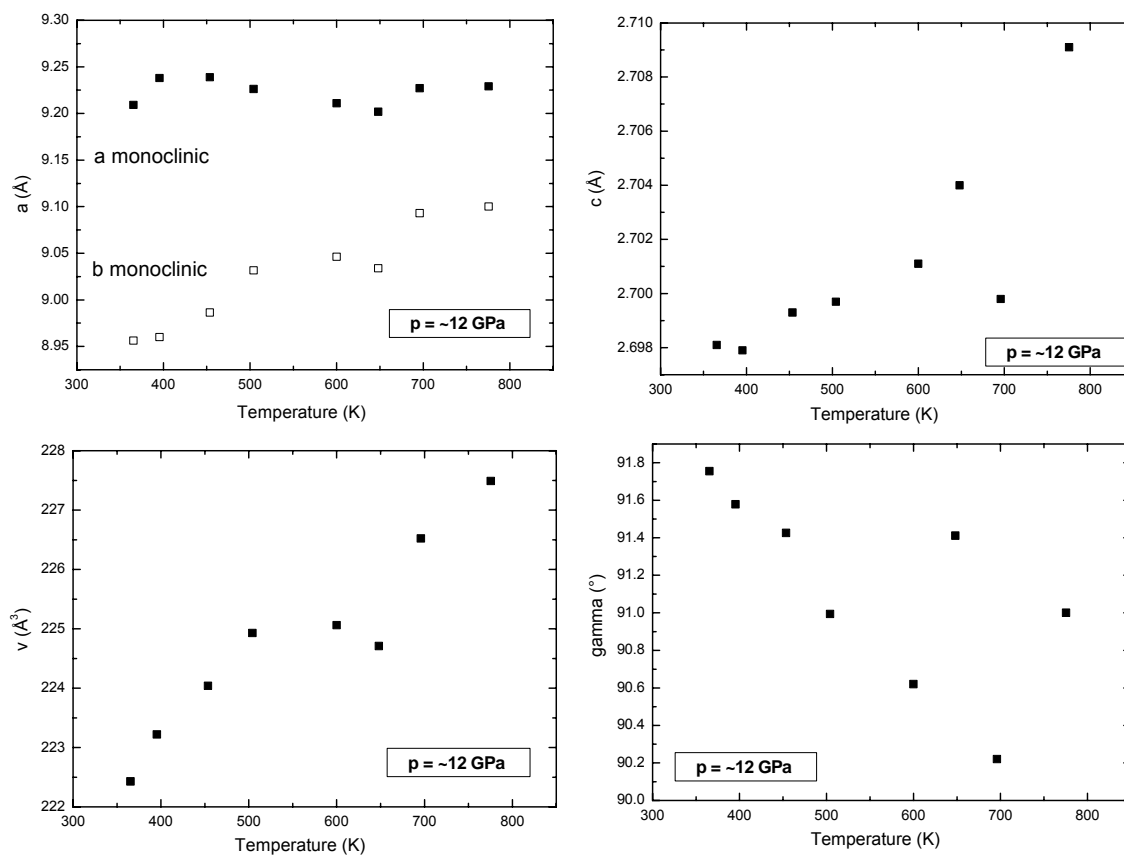


Figure 3.20. Unit-cell lattice parameters changes of the monoclinic phase caused by the temperature increase at ~12 GPa.

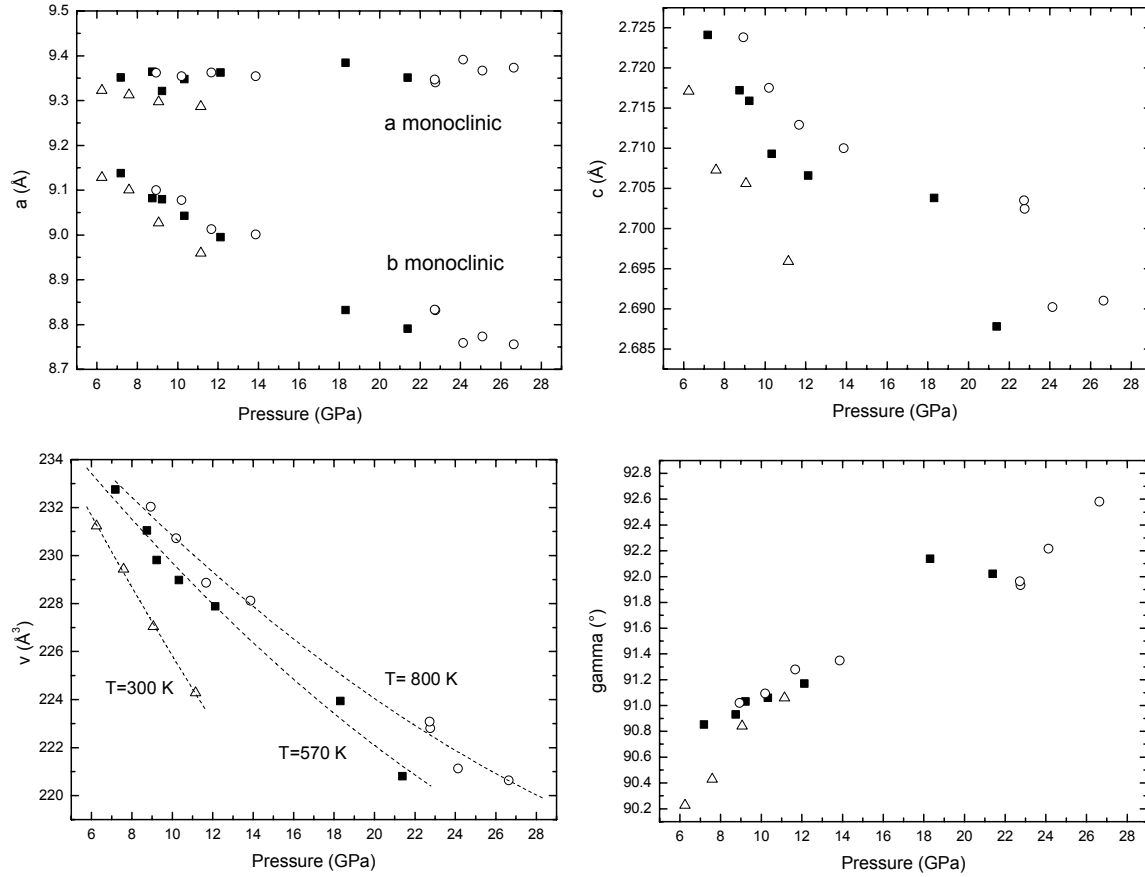


Figure 3.21. Comparison of the unit-cell lattice parameters of the monoclinic phase measured at different temperature. Open triangles are data collected at room temperature; solid squares are data at ~ 570 K; open circles are data at ~ 800 K. Dotted lines are guide to the eyes for the variation of the volume at the different temperatures.

3.7.1 The Equation of state

The equation of state was calculated for the room temperature data only, using a second order Birch-Murnaghan expression (K_0' fixed to 4.0). For the tetragonal phase, the calculated Murnaghan EOS parameters are: $V_0 = 235.6 (1) \text{ \AA}^3$, $K_0 = 376 (30) \text{ GPa}$. For the monoclinic phase: $V_0 = 242.0 (4) \text{ \AA}^3$, $K_0 = 126 (4) \text{ GPa}$. Scattering of the data collected at high-pressure and high-temperature as well as the impossibility to constrain the volume at $P = 0$ for the monoclinic phase at different pressure, prevented from obtaining a P - V - T EoS for $\text{K}_{0.5}\text{Na}_{0.5}\text{AlSi}_3\text{O}_8$ monoclinic hollandite.

3.8 High pressure Raman experiments

3.8.1 High pressure Raman experiments of KAlSi_3O_8 hollandite in argon as pressure transmitting medium

Two high pressure experiments of KAlSi_3O_8 hollandite end-member have been done using Raman spectroscopy. These experiments were carried out on a LABRAM Raman spectrometer with a He-Ne laser with the 632 nm red line excitation. The diamonds of the DAC have culets of 300 μm . Rhenium gaskets with an initial thickness of 250 μm were pre-indented to 50 μm and drilled to a diameter of 150 μm . In each experiment, a single crystal of KAlSi_3O_8 hollandite from sample S3356 was loaded in the DAC with argon as pressure transmitting medium and a ruby as pressure standard. The spectrometer was calibrated using the Γ_{25} phonon of Si ($Fd\bar{3}m$). Raman spectra were analysed using the PeakFitTM program by Jandel Scientific. The Savitsky-Golay data-smoothing algorithm was used in the peak analysis. Combinations of Lorentzian and Guassian function were used to describe the profile of the vibrational peaks. The peak positions of all vibrational peaks as well as the full width at half maximum (FWHM) for the well defined peaks at 217 cm^{-1} and at 763 cm^{-1} determined at each pressure are listed in Table 3.15 for both experiments.

Experiment 1

In this experiment the KAlSi_3O_8 hollandite sample was compressed up to ~ 30 GPa at room temperature, and then slowly decompressed to ambient pressure. Raman spectra were collected during both compression and decompression. However, due to major peak broadening once reached 30.5 GPa, likely due to non-hydrostatic stresses, the quality of the Raman spectra collected during decompression is very poor and they were, therefore, not considered during the quantitative analysis. The Raman spectra collected at different pressure during compression of the DAC are reported in Figure 3.22. Five vibrational peaks are visible in the high-pressure Raman spectra (Table 3.15). The variation as a function of pressure of the well defined peak at about 763 cm^{-1} in the Raman spectrum collected at room temperature is

shown in Figure 3.23. A change in the slope of the peak shift as well as broadening have been observed above 15 GPa.

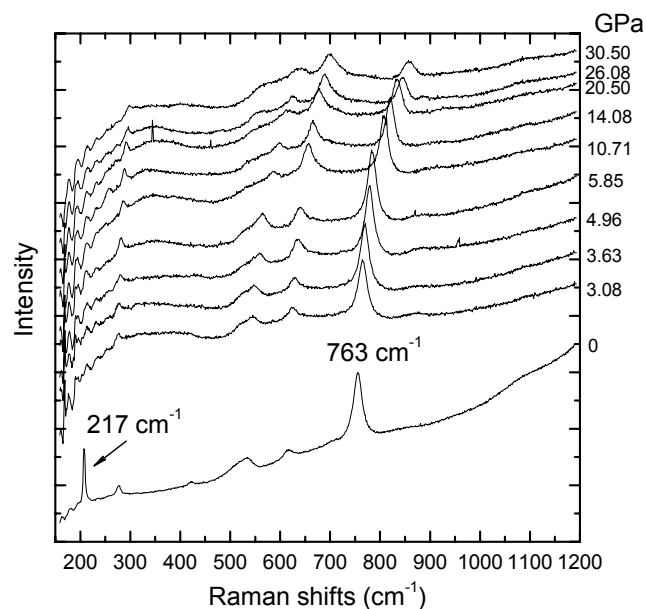


Figure 3.22. Raman spectra of KAlSi_3O_8 hollandite at different pressures. The spectrum at ambient pressure was collected before loading the sample into the diamond cell. After loading, the peak at $\sim 217 \text{ cm}^{-1}$ was no longer visible.

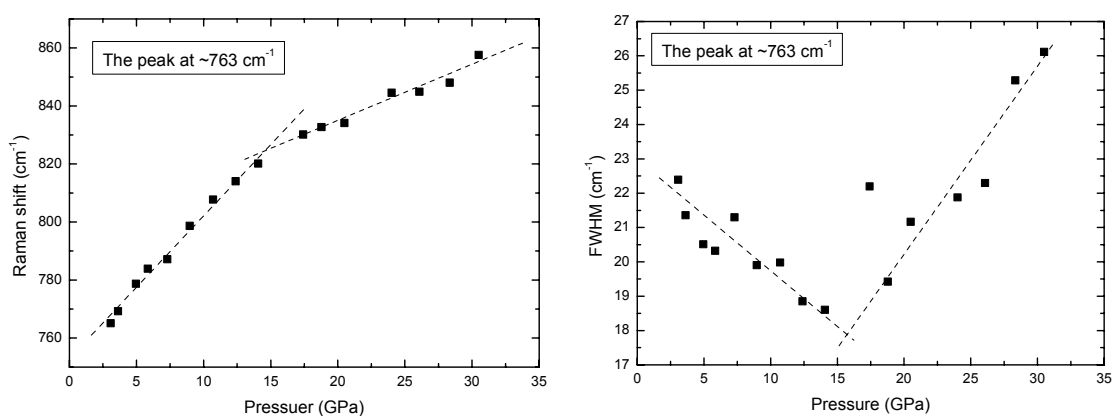


Figure 3.23. Peak shift and FWHM change with pressure of the strongest peak at $\sim 763 \text{ cm}^{-1}$. The change in slope at $\sim 15 \text{ GPa}$ may indicate a phase transition. Dashed lines were drawn as guides to the eye.

Experiment 2

In this experiment, with improved sample quality, high pressure behaviour of the peak at ~ 217 cm^{-1} could be observed in the diamond cell. The KAlSi_3O_8 hollandite single-crystal was compressed up to ~ 20 GPa at room temperature, and then the experiment was terminated due to the breaking of one of the diamonds of the DAC. Raman spectra were collected at different pressures during compression, and are shown in Figure 3.24.

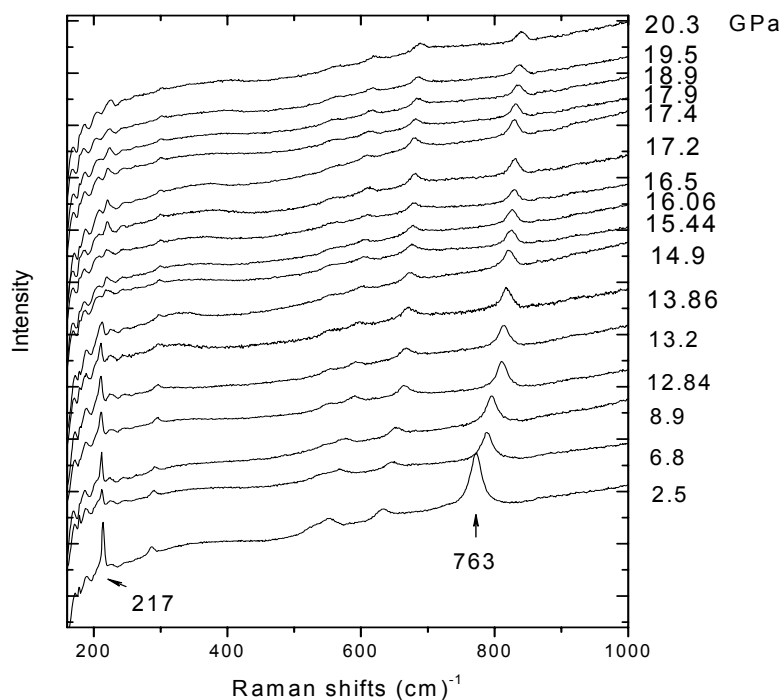


Figure 3.24. Raman spectra collected during compression at different pressures.

The lowest frequency peak at ~ 217 cm^{-1} can be observed at least up to 14 GPa and shows softening with increasing pressure (Figs. 3.25; 3.26). At higher pressures the Raman spectra became too noisy and the intensity of this peak too low to be precisely determined. The variation as a function of pressure of the peak at ~ 763 cm^{-1} is shown in Figure 3.26. No change in slope can be observed in its peak shift.

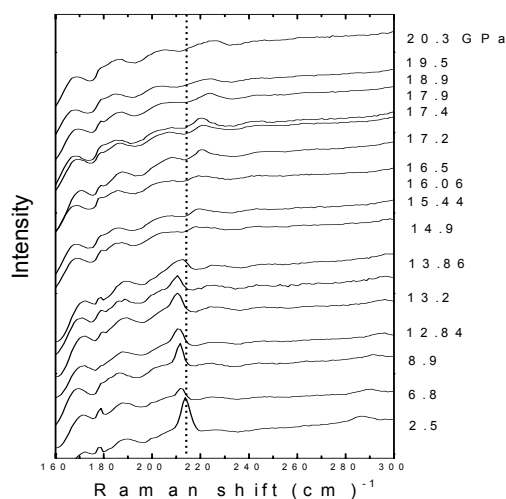


Figure 3.25. Softening of the Raman peak at $\sim 217 \text{ cm}^{-1}$. The dashed vertical line is drawn at 217 cm^{-1} as guide to the eye.

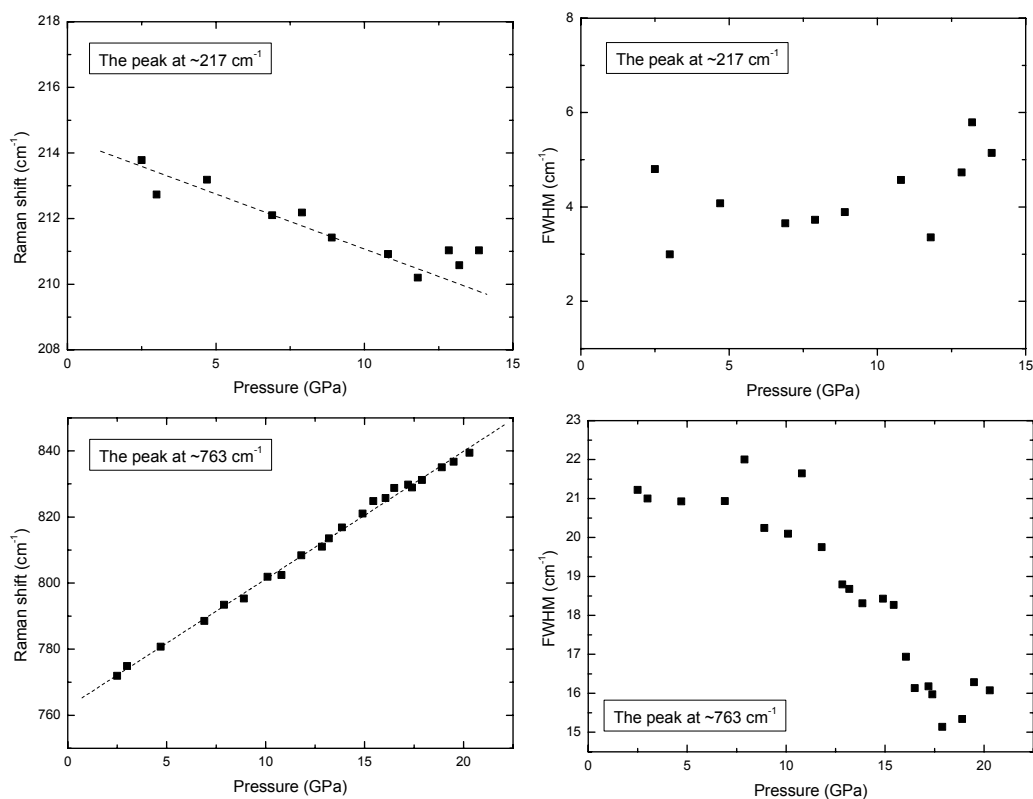


Figure 3.26. Peak shifts and FWHM changes with pressure of the lowest frequency peak at $\sim 217 \text{ cm}^{-1}$ and of the highest frequency peak at $\sim 763 \text{ cm}^{-1}$ observed. The peak at $\sim 217 \text{ cm}^{-1}$ shows a softening behaviour. The peak at $\sim 763 \text{ cm}^{-1}$ shows no significant change in all pressure range. Dashed lines are shown as guides to eye.

Table 3.15. Peak position and full width at half maximum (FWHM) determined at each pressure for KAlSi_3O_8 hollandite in Experiment 1 and 2.

		Peak positions (cm ⁻¹)					FWHM (cm ⁻¹)		
Experiment 1	Pressure (GPa)	Peak 1	Peak 2	Peak 3	Peak 4	Peak 5 at ~763 cm ⁻¹	Peak 6 at ~217 cm ⁻¹	Peak 5 at ~763 cm ⁻¹	Peak 6 at ~217 cm ⁻¹
	3.1	277.3	520.2	543.9	624.3	765.1		22.4	
	3.6	277.4	524.1	548.6	628.2	769.2		21.4	
	5.0	279.7	538.8	559.3	635.7	778.7		20.5	
	5.9	281.6	534.7	564.	640.0	783.9		20.3	
	7.3	281.9	538.2	566.5	642.3	787.1		21.3	
	9.0	284.5	538.1	577.7	649.9	798.7		20.0	
	10.7	286.7	536.7	586.3	656.3	807.7		20.0	
	12.4	2873	547.9	592.4	661.2	814.1		18.8	
	14.1	288.7	549.9	596.9	665.5	820.2		18.6	
	17.4	291.0	565.1	607.8	674.1	830.1		22.2	
	18.8	291.9	551.1	607.3	674.9	832.7		19.4	
	20.5	290.8	557.2	612.1	677.6	834.1		21.2	
	24.0	294.2	563.1	624.37	686.5	844.5		21.9	
	26.1	296.1	557.30	623.8	689.5	844.9		22.3	
	28.4	296.3	555.9	625.2	690.3	848.0		25.3	
30.5	298.2	568.4	634.8	700.4	857.6		26.1		
Experiment 2	2.5	286.6	530.2	551.7	633.5	772.0	213.8	4.8	21.2
	3.0	286.7	531.6	554.0	634.2	774.9	212.7	3.0	21.0
	4.7	287.9	541.3	560.5	639.1	780.7	213.2	4.1	20.9
	6.9	289.5	541.8	567.9	6461	788.5	212.1	3.7	20.9
	7.9	290.7	548.9	572.4	650.2	793.5	212.2	3.7	22.0
	8.9	291.1	546.9	574.3	652.6	795.3	211.4	3.9	20.2
	10.1	292.4	557.8	581.5	657.6	801.9			20.1
	10.8	293.0	550.2	580.7	658.0	802.4	210.9	4.6	21.6
	11.8	293.9	551.9	586.5	662.3	808.4	210.2	3.4	19.7
	12.8	294.9	551.9	588.7	665.0	811.0	211.0	4.7	18.8
	13.2	295.3	554.4	591.0	667.8	813.5	210.6	5.8	18.7
	13.9	296.2	553.8	593.9	670.9	816.8	211.0	5.1	18.3
	14.9	296.8	554.5	599.1	673.2	821.0	212.0	8.7	18.4
	15.4	297.7	559.7	602.6	676.7	824.8		17.5	
	16.1	298.8	562.7	603.2	678.1	825.7		13.0	
	16.5	299.3	557.2	607.6	681.3	828.8		14.5	
	17.2	299.2	558.3	609.1	680.5	829.8		11.2	
	17.4	298.9	558.7	607.7	680.6	828.9		11.0	
	17.9	299.8	558.9	610.6	682.5	831.2		9.8	
	18.9	299.8	558.1	614.2	684.4	835.1		8.2	
19.5	300.8	563.8	615.2	686.0	836.7		13.5		
20.3	301.5	563.6	618.9	688.1	839.4		10.2		

The variation of all peak positions determined from the Raman spectra of both sets of experiments are shown in Figure 3.27. The major difference between the two experiments is the change in slope of the peak shifts of Experiment 1 at about 15 GPa, not visible in the peak shifts determined for Experiment 2. All peak positions appear to increase as a function of pressure, except that of peak 6 (at 217 cm^{-1}), which shows softening.

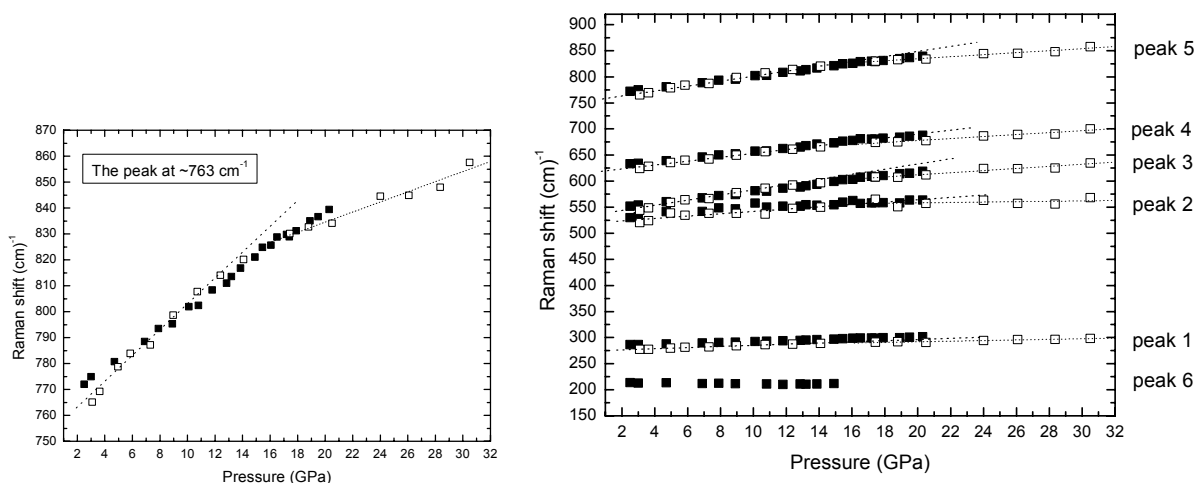


Figure 3.27. Peak shifts of KAlSi_3O_8 hollandite with pressure. Open squares are data from Experiment 1, and solid squares are data from Experiment 2. Dotted lines show the change in slope of the peak shifts determined for Experiment 1 and are simple guides to the eye.

3.8.2 High pressure Raman experiment of $\text{K}_{0.6}\text{Na}_{0.4}\text{AlSiO}_8$ hollandite in lithium fluoride as pressure transmitting medium

This experiment was carried out on a Raman spectrometer of a Dilor XY system with the 514.5 nm Ar⁺ ion laser equipped with a microscope and liquid-nitrogen-cooled CCD detector. Gem-quality diamonds with culets of 400 μm were mounted in the cells. A rhenium gasket with an initial thickness of 250 μm was pre-indented to $\sim 50\text{ }\mu\text{m}$ and drilled to a diameter of 200 μm . $\text{K}_{0.6}\text{Na}_{0.4}\text{AlSiO}_8$ hollandite (sample H2353) and LiF powder were packed into the hole in the gasket. A piece of ruby was placed near the hollandite sample, as an internal pressure standard. The sample was compressed at room temperature up to $\sim 19\text{ GPa}$. After that

broadening of the peaks in the Raman spectra was so severe that no more measurement was possible. This was probably due to the stresses caused by the non-hydrostatic pressure transmitting medium LiF. The Raman spectra collected at different pressures are plotted in Figure 3.28. Quantitative analysis of the peak position and FWHM was performed only for the well defined peaks at $\sim 217 \text{ cm}^{-1}$ and $\sim 763 \text{ cm}^{-1}$ (Table 3.16). At pressures above $\sim 14 \text{ GPa}$ the peak at $\sim 217 \text{ cm}^{-1}$ became too broad and too weak to be further analyzed.

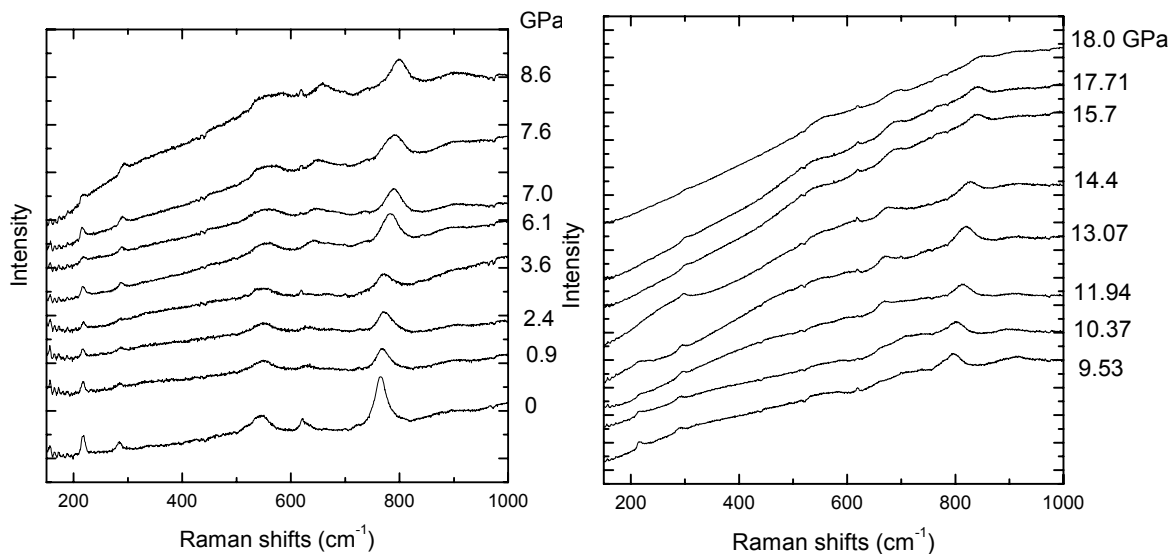


Figure 3.28. Raman spectra collected for $\text{K}_{0.6}\text{Na}_{0.4}\text{AlSiO}_8$ at different pressures.

The variation of the peak position and FWHM of both peaks is shown in Figure 3.29. Broadening of these peaks appears above 4 GPa. At the same pressure a change in slope in the shift of the peak at 763 cm^{-1} can be observed. The change in peak position of the peak at 217 cm^{-1} is very small and shows a large scatter.

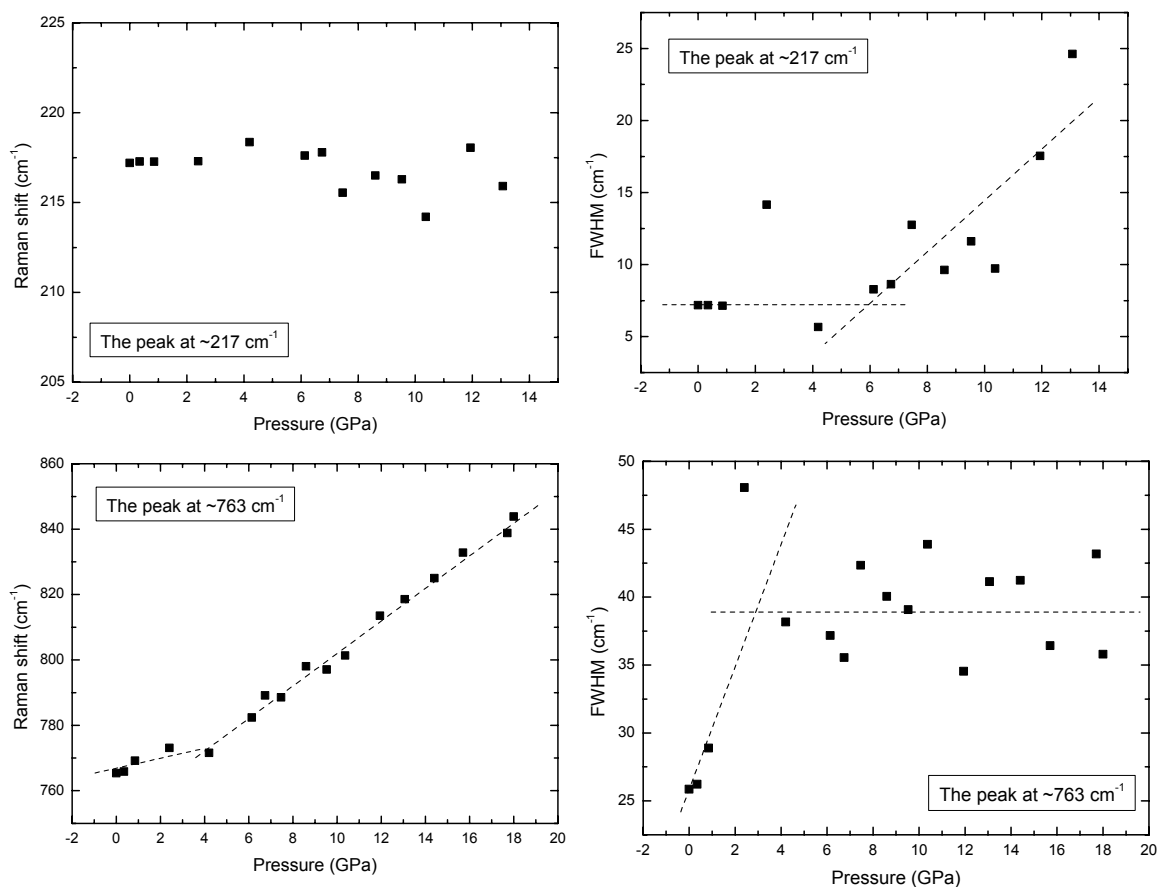


Figure 3.29. Peak shifts and FWHM changes with pressure of the peaks at $\sim 217 \text{ cm}^{-1}$ and at $\sim 763 \text{ cm}^{-1}$. Above $\sim 4 \text{ GPa}$ the peaks are clearly broader. Dashed lines were drawn as guides to the eye.

Table 3.16. Peak position and full width at half maximum (FWHM) determined at each pressure for the well defined peaks in the Raman spectra of $\text{K}_{0.6}\text{Na}_{0.4}\text{AlSiO}_8$.

Pressure (GPa)	Peak at $\sim 763 \text{ cm}^{-1}$		Peak at $\sim 217 \text{ cm}^{-1}$	
	Peak positions (cm^{-1})	FWHM (cm^{-1})	Peak positions (cm^{-1})	FWHM (cm^{-1})
0.00001	765.3	25.9	217.2	7.2
0.4	765.8	26.2	217.3	7.2
0.9	769.2	28.9	217.3	7.1
2.4	773.1	48.1	217.3	14.2
4.2	771.6	38.2	218.4	5.7
6.1	782.4	37.2	217.6	8.3
6.7	789.2	35.6	217.8	8.6
7.5	788.6	42.4	215.5	12.8
8.6	798.0	40.1	216.5	9.6
9.5	797.1	39.1	216.3	11.6
10.4	801.3	43.9	214.2	9.7
11.9	813.5	34.5	218.0	17.5
13.1	818.6	41.1	215.9	24.6
14.4	825.0	41.2		
15.7	832.8	36.4		
17.7	838.8	43.2		
18.0	843.9	35.8		

4. Discussion

4.1 The (Na,K)AlSi₃O₈ hollandite solid solution

The (Na,K)AlSi₃O₈ hollandite solid solution has been studied using multi-anvil apparatus in the pressure range between 13 and 26 GPa and temperatures between 1500 and 2200 °C, using (Na_{0-0.6}, K_{1-0.4})AlSi₃O₈ glasses, NaAlSi₃O₈ glass, and Na_{0.75}K_{0.05}Ca_{0.1}AlSi₃O₈ glass as starting materials. The solubility of Na into the KAlSi₃O₈ hollandite structure increases with increasing pressure as well as with increasing temperature (Figure 3.4). Homogeneous assemblages with a pure hollandite phase (and not more than 1 – 2 % of stishovite) were synthesized at temperature of 1700 °C and different pressures with 0%, 10%, 30%, 40%, 50% of Na content. Any further increase of pressure and/or temperature had no effect on improving the Na solubility. Also no pure Na hollandite end-member was found in any of the recovered synthesis products.

4.1.1 Solid solution behaviour

The unit-cell parameters of the (Na,K)AlSi₃O₈ hollandite decreases linearly with increasing Na content (Figure 3.3). Previous studies (Post et al., 1982; Bayer et al., 1966; Endo et al., 1976; Cadee et al., 1978; Sinclair et al., 1980) have shown that the unit-cell volume of different hollandite-type materials varies linearly with the size of the octahedral cations, without being affected by the size of the cations in the tunnels. In our study, however, the octahedral cations are the same along the solid solution and substitution of Na into the KAlSi₃O₈ end-members clearly affects the unit-cell parameter variation. The cell parameter *a* decreases more rapidly with increasing Na component than the cell parameter *c*. Also high-pressure experiments (Zhang et al., 1993; Ferroir et al., 2006) have shown that the *a* axis is more compressible than the *c* axis. Since decreasing the size of the tunnel cation should affect the octahedral framework in the same way as subjecting it to compression (Hazen and Finger, 1982), we can expect the cation to cation repulsion along the *c* direction will increase with increasing Na content.

The single crystal study of KAlSi_3O_8 hollandite and $\text{K}_{0.8}\text{Na}_{0.2}\text{AlSi}_3\text{O}_8$ hollandite shows that Si and Al are disordered among octahedral sites in KAlSi_3O_8 (sample S3356) and $\text{K}_{0.8}\text{Na}_{0.2}\text{AlSi}_3\text{O}_8$ (sample H2495). That is consistent with the suggestion reported by Post and Burnham (1986) that the octahedral cations are probably disordered in most hollandite structures due to the narrow range of structure energies calculated for most of the possible configurations. The calculations performed by Post and Burnham (1986) also show that the most energetically unfavourable octahedral cation arrangements are those for which the lower-valence cations (in this case Al^{3+}) occupy octahedra that share a common edge. This correlation between structure energy and degree of edge-sharing Al octahedra is analogous to the aluminium avoidance rule (Loewenstein, 1954) observed in several silicate minerals, among which feldspars which are the low pressure phases of the hollandites studied in this work. The major difference shown by the structural refinements of the two crystals is in the distribution of the tunnel cations. The smaller Na appears to prefer a crystallographic site closer to the wall and away from the central axis of the tunnel. In this split position the Na has only 5 oxygens at a distance smaller than 3 Å (all 5 distances are between 2.4 and 2.6 Å). We have excluded that the split-site observed can be occupied by H_2O , although it is known that some minerals with the hollandite structure may incorporate some small amount of H_2O , because, due to the anhydrous synthesis conditions used, the total amount of H_2O which could be present in our samples would be not detectable by means of X-ray diffraction.

The Si(Al)O_6 octahedra are very similar in both KAlSi_3O_8 and $\text{K}_{0.8}\text{Na}_{0.2}\text{AlSi}_3\text{O}_8$ hollandite (Table 3.6), suggesting that there is no significant effect of Na substitution on the octahedral framework. This also is consistent with the results of the Raman study; the Raman spectra, in fact, show no significant changes (Figure 3.6 and 3.7) for the hollandite samples with different Na content, indicating that the Si(Al)-O vibrations are not affected by the cation substitution occurring in the tunnels.*

With respect to stishovite, the Si(Al)O_6 octahedron in both samples are more distorted than the SiO_6 octahedron in stishovite, and this is in agreement with the results reported by Zhang et al. (1993). The difference between the longest and shortest Si(Al)-O bond distances is ~ 0.076 Å and 0.78 Å in KAlSi_3O_8 and $\text{K}_{0.8}\text{Na}_{0.2}\text{AlSi}_3\text{O}_8$ hollandite, respectively (Table 3.6), larger than the difference of ~ 0.05 Å in stishovite (Ross et al., 1990), but slightly smaller than the value

* Note that the vibrational mode dominated by translations of the tunnel cations (Na and K) are at much lower energies than those sampled by the Raman spectrometer used in this study.

reported by Zhang et al. (1993) of ~ 0.1 Å. The angle O1b-Si(Al)-O2b subtended by the shared horizontal edge in KAlSi_3O_8 hollandite is $82.00(3)^\circ$, similar to that in Zhang's study, and larger than the corresponding 81.3° angle in stishovite, which can be due to the weaker cation to cation repulsive force across the shared edge caused by the substitution of Al^{3+} for Si^{4+} . In $\text{K}_{0.8}\text{Na}_{0.2}\text{AlSi}_3\text{O}_8$ hollandite, this value is $82.13(2)^\circ$.

4.1.2 The $\text{NaAlSi}_3\text{O}_8$ hollandite

The solubility of $\text{NaAlSi}_3\text{O}_8$ component into the KAlSi_3O_8 hollandite structure increases with increasing pressure (Figure 4.1) and temperature (Figure 3.4). However, after reaching the maximum Na content of ~ 53 mol %, further increasing pressure and temperature have little effect on increasing the Na solubility. No $\text{NaAlSi}_3\text{O}_8$ hollandite end-member was synthesized in the P - T range of this study. This may be due to the fact that the size of Na is too small to stabilize the hollandite structure.

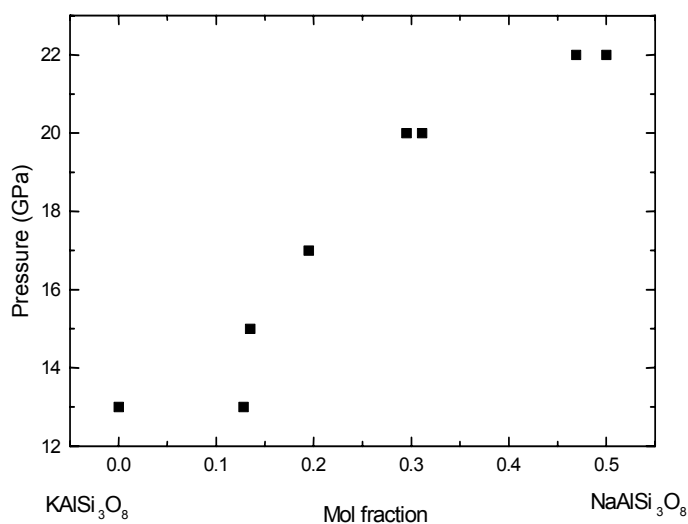


Figure 4.1 The solubility of Na-component in hollandite increases with increasing pressure

In the shock induced melt veins in meteorite where natural $\text{NaAlSi}_3\text{O}_8$ hollandite was found, thermal gradient as well as quenching conditions are very different with respect to the multi-anvil experiments. The temperature dissipates much faster during the shock event and there are

enormous temperature gradients, so that minerals crystallizing under non-equilibrium conditions may survive after quenching. In the multi-anvil press the samples are kept at high temperatures for at least 15 minute up to 2 hours, and the quenching rate is very slow compared to that of the shock event. The $\text{NaAlSi}_3\text{O}_8$ hollandite reported by Liu (1978) was synthesized in the diamond anvil cell experiments by laser heating, also in this case temperature gradients can be quite high as suggested by Yagi et al (1994), and quenching is also very fast. It may therefore be possible that the $\text{NaAlSi}_3\text{O}_8$ hollandite found in meteorites or in the diamond cell experiments could result from disequilibrium conditions. Also in the multi-anvil experiments described by Liu (2006), with $\text{K}_{0.2}\text{Na}_{0.8}\text{AlSi}_3\text{O}_8$ glass as starting material the maximum Na content in the (Na,K) hollandite products found was ~51 mol%, (synthesis conditions: 14-25 GPa and 1400-2400 °C).

$\text{NaAlSi}_3\text{O}_8$ hollandites found in meteorites contain some amount of Ca and K, usually up to ~2% of Ca and ~0.5% of K (Gillet *et al.*, 2000; Tomioka *et al.*, 2000; Xie *et al.*, 2001). In the synthesis experiment at 22 GPa and 1900 °C with an albite glass containing small amounts of Ca and K to simulate the natural occurrence of $\text{NaAlSi}_3\text{O}_8$ hollandite, the resulting synthesis product was a mixture of phase among which also a hollandite with composition $\text{K}_{0.26}\text{Na}_{0.53}\text{Ca}_{0.16}\text{Al}_{1.15}\text{Si}_{2.86}\text{O}_8$. Although the Na content in this hollandite is still no higher than 53 mol%, the ratio $\text{Na}/(\text{Na}+\text{K}+\text{Ca}) = 0.56$ is greater than the $\text{Na}/(\text{Na}+\text{K})$ ratio of any other experiment performed in this study. This also indicates that cations larger than Na need to be used in order to stabilize the hollandite structure.

4.1.3 The symmetry of $(\text{K},\text{Na})\text{AlSi}_3\text{O}_8$ hollandite: tetragonal vs. monoclinic

Many hollandite-type minerals crystallize in the monoclinic symmetry (space group $I2/m$), instead than the tetragonal. Post and Bureham (1986) suggested that when the tunnel cation is small, it becomes less constrained in the coordination polyhedron. If the cation is small enough, the octahedral walls undergo twisting distortions to accommodate minimum energy cation positions, causing the structure to adopt lower symmetry. Zhang and Burnham (1994) derived equations to predict the symmetry of hollandite-type compounds based on their composition. The symmetry of a hollandite-type compound is related to the size of the tunnel

cation (A) relative to the size of the octahedral framework. If $r_A > \sqrt{2}(r_O + r_B) - r_O$ (where r_A , r_B , and r_O are the ionic radii of the tunnel cation A, the octahedral cation B, and the oxygen O, respectively), the compound will be tetragonal, whereas if $r_A < \sqrt{2}(r_O + r_B) - r_O - 0.15$ it will be monoclinic. The extra 0.15 Å in the equation is the estimated limit of tunnel cation displacement that tetragonal structures sustain without octahedral wall distortions. If the size of the tunnel cation lies in between these two values, the hollandite can have either the tetragonal structure or the monoclinic structure. Using this theory, the symmetry of KAlSi_3O_8 , $\text{K}_{0.8}\text{Na}_{0.2}\text{AlSi}_3\text{O}_8$, $\text{K}_{0.5}\text{Na}_{0.5}\text{AlSi}_3\text{O}_8$, and $\text{NaAlSi}_3\text{O}_8$ hollandites are predicted (Figure 4.2). The r_A , r_B , and r_O ionic radii values are those reported by Shannon and Prewitt (1969) (Table 4.1). All KAlSi_3O_8 , $\text{K}_{0.8}\text{Na}_{0.2}\text{AlSi}_3\text{O}_8$, and $\text{K}_{0.5}\text{Na}_{0.5}\text{AlSi}_3\text{O}_8$ hollandites plot in the tetragonal field, in agreement with our experimental results, whereas the $\text{NaAlSi}_3\text{O}_8$ hollandite falls in the region that might have either one of the two structures.

Table 4.1. r_A , r_B and r_O values of hollandite with different K, Na component.

Hollandite composition	r_A (Å)	r_B (Å)	r_O (Å)
KAlSi_3O_8	1.51	0.4325	1.40
$\text{K}_{0.8}\text{Na}_{0.2}\text{AlSi}_3\text{O}_8$	1.44	0.4325	1.40
$\text{K}_{0.5}\text{Na}_{0.5}\text{AlSi}_3\text{O}_8$	1.335	0.4325	1.40
$\text{NaAlSi}_3\text{O}_8$	1.16	0.4325	1.40

Note r_B has been obtained by using $0.75 r_{\text{Si}} + 0.25 r_{\text{Al}}$ ($r_{\text{Si}} = 0.4$ Å, and $r_{\text{Al}} = 0.53$ Å).

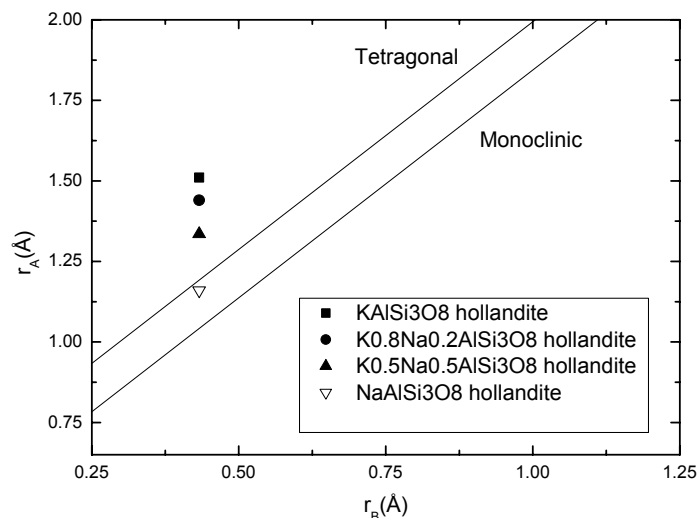


Figure 4.2. Plot of the ionic radii of (K,Na)AlSi₃O₈ hollandites. The solid lines define the two limits $r_A = \sqrt{2}(r_O + r_B) - r_O$, and $r_A = \sqrt{2}(r_O + r_B) - r_O - 0.15$ (Zhang and Burnham, 1994). Data above these lines are predicted to have tetragonal symmetry; whereas data below these lines have monoclinic symmetry. The region between the two lines define those ionic radii for which the hollandite-type compound can be either tetragonal or monoclinic.

4.2 High pressure and high temperature behaviour of (Na,K)AlSi₃O₈ hollandite

High pressure behaviour of hollandite samples with the composition of KAlSi₃O₈, K_{0.8}Na_{0.2}AlSi₃O₈, K_{0.6}Na_{0.4}AlSi₃O₈, and K_{0.5}Na_{0.5}AlSi₃O₈ have been studied using diamond anvil cells by means of X-ray powder diffraction and Raman spectroscopy. High temperature behaviour of K_{0.5}Na_{0.5}AlSi₃O₈ hollandite at high pressures has also been studied using X-ray diffraction. At high pressures, the hollandite samples all transform to hollandite II with monoclinic structure and space group *I2/m*. The transition pressure decreases with increasing Na content, probably because the small Na atom stabilizes the monoclinic structure. If we use the transition pressure determined from the experiments done in quasi-hydrostatic conditions with He as transmitting medium for KAlSi₃O₈ (Ferroir et al, 2006) and for K_{0.8}Na_{0.2}AlSi₃O₈ (this study) we can speculate about the phase transition boundary of NaAlSi₃O₈ hollandite (Figure 4.3). A simple linear fit through the two P_c is in agreement with the observation that

$\text{K}_{0.5}\text{Na}_{0.5}\text{AlSi}_3\text{O}_8$ hollandite was tetragonal up to 13.6 GPa (pressure at which the experiment stopped due to breaking of the diamonds). This linear fit shows that the transition pressure for $\text{NaAlSi}_3\text{O}_8$ hollandite should be below 10 GPa (Figure 4.3). Na substitution has not only the effect of decreasing the tetragonal to monoclinic transition pressure, but also that of increasing the anisotropic axial compressibility of the tetragonal KAlSi_3O_8 (Zhang et al. 1993; Ferroir et al. 2006). A comparison between the axial compressibility of tetragonal KAlSi_3O_8 (Ferroir et al. 2006) and of tetragonal $\text{K}_{0.8}\text{Na}_{0.2}\text{AlSi}_3\text{O}_8$ (this study) is shown in Figure 4.4. As the Na content increases, the **c** axis becomes less compressible and the **a** axis more compressible with respect to the KAlSi_3O_8 end-member. This also can be an effect related to the splitting of the Na position towards the framework walls.

The high-pressure monoclinic phases are more compressible, and are stable at higher pressures up to at least 30 GPa, indicating that hollandite may be stable in Earth's mantle and may be a possible host mineral for Na as well as K in the transition zone and even in to the lower mantle. The 2nd order Birch- Murnaghan equations of state were calculated for the tetragonal phases and monoclinic phases, and the results are summarized in Table 4.2. The values obtained from the data collected using LiF as pressure transmitting medium are very different from the values obtained from experiments under hydrostatic conditions. The bulk moduli obtained for the tetragonal phases from the data in LiF are very large (similar to the values obtained for stishovite (Ross et al. 1990). However, if only experiments done using He are compared, it appears that Na has little effects on the bulk modulus of tetragonal hollandite. The high temperature and high pressure behaviour of $\text{K}_{0.5}\text{Na}_{0.5}\text{AlSi}_3\text{O}_8$ hollandite indicates a positive Clapeyron slope for the tetragonal to monoclinic phase transition. This is in agreement with Sueda et al. (2004) and Nishiyama et al. (2005), who reported the same behaviour for KAlSi_3O_8 hollandite. Unfortunately due to the scatter of the data the P - V - T parameters for this phase could not be determined. In the high pressure Raman experiment of KAlSi_3O_8 hollandite in Experiment 2 (Figure 3.25 and 3.26), the peak at $\sim 217\text{ cm}^{-1}$ shows a softening behaviour, which is similar to the B_{1g} mode at $\sim 231\text{ cm}^{-1}$ in stishovite (Kingma et al. 1995). In stishovite, the rutile- CaCl_2 structure transition is characterized by a reversal in the pressure shifts of the lowest frequency band from the soft B_{1g} mode (in the rutile structure) to the hard A_g mode (in CaCl_2 structure) (Cohen, 1992; Hemly et al. 1994; Kingma et al. 1995). Unfortunately at higher pressures the peak at $\sim 217\text{ cm}^{-1}$ in hollandite could not be observed

due to poor signal to noise ratio of the collected spectra. Given the similarity of the high-pressure phase transformations in hollandite and in stishovite, however, one can expect that this mode will harden at the transition pressure.

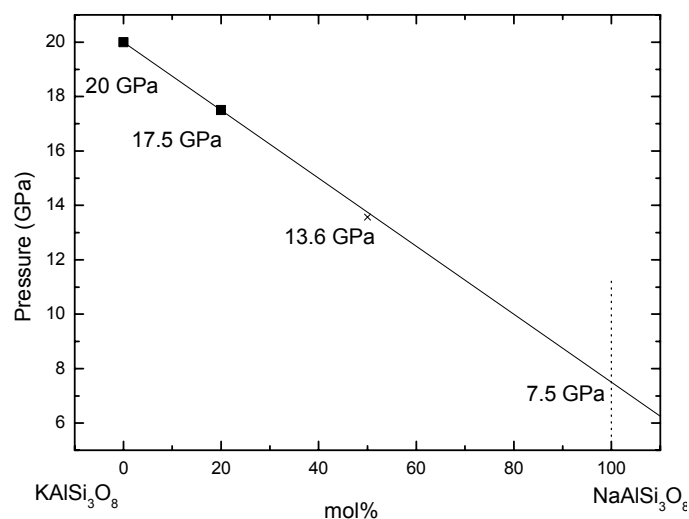


Figure 4.3. Tetragonal to monoclinic transition pressures (solid squares) as a function of Na content in KAlSi_3O_8 hollandite. The datum for KAlSi_3O_8 hollandite is from Ferroir et al. (2006). In our study, the phase transition of $\text{K}_{0.8}\text{Na}_{0.2}\text{AlSi}_3\text{O}_8$ hollandite is at 17.5 GPa. $\text{K}_{0.5}\text{Na}_{0.5}\text{AlSi}_3\text{O}_8$ hollandite is still tetragonal at 13.6 GPa (cross). The solid line is a linear fit through the P_c data at 20 and 17.5 GPa and has been extrapolated to the composition of $\text{NaAlSi}_3\text{O}_8$ hollandite, indicating a phase transition boundary at about 7.5 GPa.

Table 4.2. Comparison of the high pressure behaviours of KAlSi_3O_8 hollandite containing different amounts of Na. All the Eos parameters presented here were obtained from synchrotron X-ray experiments.

	Hollandite composition	Pressure transmitting medium	Observed phase transition pressure (GPa)	Eos parameters			
				Tetragonal phase		Monoclinic phase	
				V_0 (\AA^3)	K_0 (GPa)	V_0 (\AA^3)	K_0 (GPa)
Ferroir et al. (2006)	KAlSi_3O_8	He	20	237.0 (3)	201.4 (7)	-	-
This study: X-Ray experiments	$\text{K}_{0.8}\text{Na}_{0.2}\text{AlSi}_3\text{O}_8$	He	17.5	237.4 (2)	197 (3)	239.4 (9)	174 (7)
	$\text{K}_{0.8}\text{Na}_{0.2}\text{AlSi}_3\text{O}_8$	LiF	11	236.7 (1)	398 (28)	242.3 (2.0)	192 (23)
	$\text{K}_{0.6}\text{Na}_{0.4}\text{AlSi}_3\text{O}_8$	LiF	5	-	-	236.6 (3)	227 (8)
	$\text{K}_{0.5}\text{Na}_{0.5}\text{AlSi}_3\text{O}_8$	He	No phase transition until 13.6 GPa	235.6 (3)	230 (5)	-	-
This study: Raman experiments	$\text{K}_{0.5}\text{Na}_{0.5}\text{AlSi}_3\text{O}_8$	LiF	6	235.6 (1)	376 (30)	242.0 (4)	126 (4)
	KAlSi_3O_8	Ar	15	-	-	-	-
	KAlSi_3O_8	Ar	No phase transition until 20 GPa	-	-	-	-
	$\text{K}_{0.6}\text{Na}_{0.4}\text{AlSi}_3\text{O}_8$	LiF	4	-	-	-	-

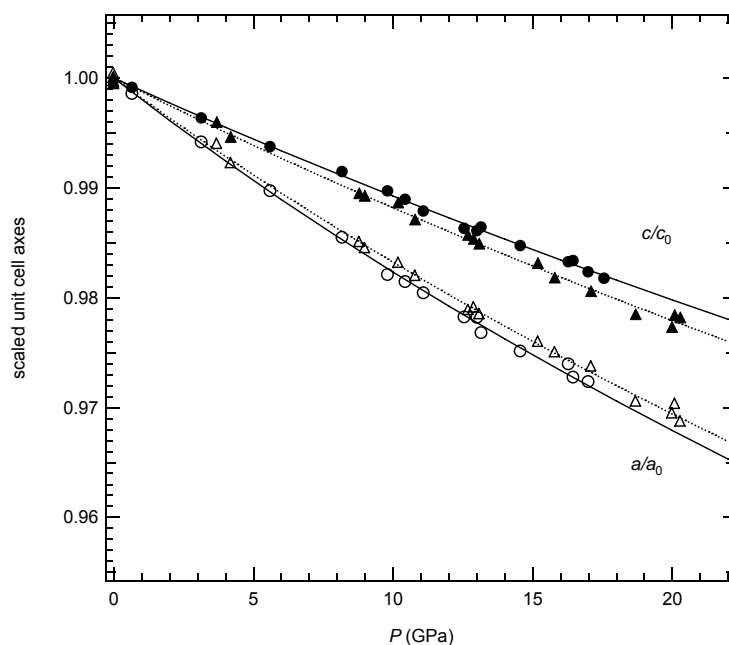


Figure 4.4. Axial compressibilities of KAlSi_3O_8 (triangles, Ferroir et al. 2006) and $\text{K}_{0.8}\text{Na}_{0.2}\text{AlSi}_3\text{O}_8$ (circles, this study) hollandites. The anisotropic behaviour of the tetragonal hollandite axes increases with increasing Na content.

4.2.1. The effect of pressure transmitting media

The choice of pressure transmitting medium can have an effect on the observed high pressure behaviour of minerals. Non-hydrostatic pressure distribution, in fact, can produce deviatoric stresses which will strain the sample in a non predictable way. Helium, for example, provides a (quasi)-hydrostatic environment up to very high pressures, but requires special equipment for loading. Solid soft media as NaCl, KCl, and KBr are instead very easy to load, and can provide a relatively low stress environment.

In the high pressure experiments of this study, three different materials (helium, argon and lithium fluoride) were used as pressure transmitting media. Ar is known to provide hydrostatic conditions only up to 8 GPa, however as a soft noble gas it can still provide quasi-hydrostatic conditions at much higher pressures. The high-pressure tetragonal to monoclinic transition in hollandite appears to be very sensitive to the amount of deviatoric stresses present in the DAC. These will introduce a stress field that can be incorporated into the Landau expansion (see

4.2.2.2 section). Depending on how strong these stresses are, the transition will be observed at lower pressure than in hydrostatic conditions. For very large stresses the monoclinic phase of hollandite will be the stable one at all pressures. To illustrate this point we can use the two Raman experiments done using Ar. A different behaviour of KAlSi_3O_8 hollandite was observed in Experiment 1 and Experiment 2 (Figure 3.23 and 3.26). In Experiment 1, changes in Peak shift and FWHM indicate a phase transition at ~ 15 GPa, which is 5 GPa lower than the transition pressure reported by Ferroir et al. (2006). In Experiment 2, instead, no phase transformation was observed up to ~ 20 GPa. This suggests that the stresses present in the two experiments were different.

The experiments conducted using LiF as pressure transmitting medium show even a more drastic behaviour. LiF was chosen because it is a chemically stable soft material and has similar properties as other solid pressure mediums NaCl, KCl and KBr. This material is much easier to be loaded into the diamond anvil cell than the noble gases such as He and Ar. All the observed transition pressures in LiF are much lower than the real transition pressures. The high stresses also cause broadening of the diffraction peaks, and as a consequence increase the scattering of the lattice parameters obtained at high pressure.

4.2.2 The spontaneous strain behaviour of the tetragonal to monoclinic high-pressure phase transition in hollandite

4.2.2.1. Spontaneous strain behaviour under hydrostatic condition

Under hydrostatic conditions where He was used as pressure transmitting medium, the strain behaviour of $\text{K}_{0.8}\text{Na}_{0.2}\text{AlSi}_3\text{O}_8$ hollandite (Figure 3.16) shows a proper ferroelastic phase transition second-order in character, and extrapolation to zero strain gives a transition pressure of ~ 17.5 GPa, which is consistent with the pressure at which splitting of the diffraction lines was observed. In order to compare the phase transition mechanism of $\text{K}_{0.8}\text{Na}_{0.2}\text{AlSi}_3\text{O}_8$ hollandite with KAlSi_3O_8 hollandite, the strain components of KAlSi_3O_8 hollandite were calculated using the high pressure data reported by Ferroir et al. (2006). Comparison between the square of the symmetry adapted strain, e_1-e_2 , of KAlSi_3O_8 and $\text{K}_{0.8}\text{Na}_{0.2}\text{AlSi}_3\text{O}_8$ hollandites

is shown in Figure 4.5 as a function of pressure. Extrapolation to zero strain of the linear fit through the data of KAlSi_3O_8 hollandite gives a transition pressure of ~ 20 GPa, which is in good agreement with the reported phase transition boundary observed by Ferroir et al. 2006. The practically parallel linear fits of the two sets of data (Figure 4.5) indicate that the tetragonal to monoclinic transition mechanism are the same. Thus, Na substitution affect the transition pressure but does not alterate the transition mechanism.

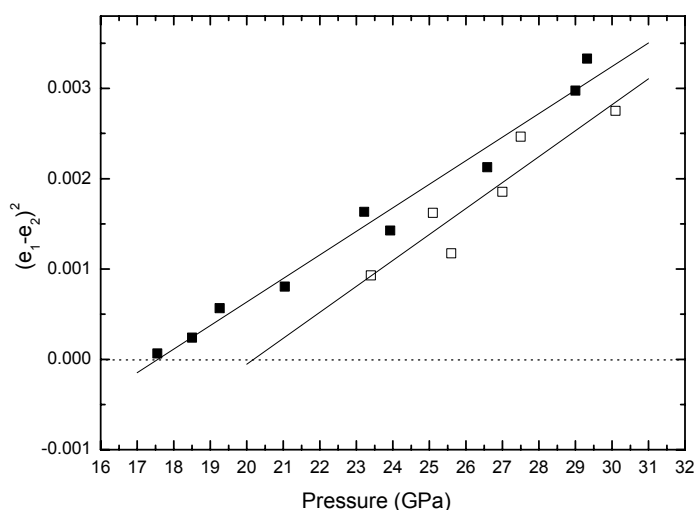


Figure 4.5. Variation of the square of the symmetry adapted strain with pressure. Solid squares are data of $\text{K}_{0.8}\text{Na}_{0.2}\text{AlSi}_3\text{O}_8$ hollandite from this study, and open squares are data calculated using high pressure data of KAlSi_3O_8 hollandite reported by Ferroir et al. (2006). Solid lines are linear fits through the data given by $(e_1 - e_2)^2 = -0.0046(3) + 0.00026(1)P$ for $\text{K}_{0.8}\text{Na}_{0.2}\text{AlSi}_3\text{O}_8$ hollandite, and $(e_1 - e_2)^2 = -0.0058(15) + 0.00029(6)P$ for KAlSi_3O_8 hollandite.

4.2.2.2. Spontaneous strain behaviour in lithium fluoride

The phase transition pressures observed in the experiments conducted with LiF are much lower than those observed under hydrostatic conditions. The stress effect introduced by the non-hydrostaticity of the pressure transmitting medium can be incorporated into the Landau free-energy expansion as:

$$G(Q, e) = hQ + L(Q) + \lambda(e_1 - e_2)Q + \lambda e_6 Q + \lambda(e_1 + e_2)Q^2 + e_3 \lambda Q^2$$

where the term hQ is used to describe the stress applied to the sample. As soon as h is different from zero the stable phase will be the monoclinic independently of the transition pressure of the material. However, for small values of h one can expect to be able to estimate the real phase transition pressure by extrapolating the behaviour of Q at high pressure as qualitatively describe in Figure 4.6 (curve 2). For values of h too large, no information on the transition can be deduced (Figure 4.6, line 3 instead).

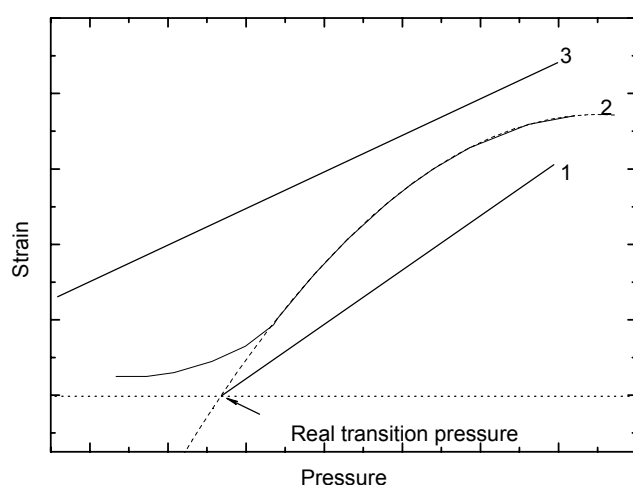


Figure 4.6. Schematic drawing of the effect of stress on the order parameter behaviour for the high-pressure tetragonal to monoclinic transition in hollandite. Line 1 is the behaviour of Q under hydrostatic condition (second order phase transformation). Curve 2 shows an example of order parameter behaviour for small stresses, so that the higher pressure behaviour can be extrapolated to estimate the phase transition pressure. Line 3 shows an example for very large stresses, for which the monoclinic phase is stable at all pressures.

To elucidate what just described, the symmetry-breaking strain behaviours of $\text{K}_{0.8}\text{Na}_{0.2}\text{AlSi}_3\text{O}_8$ hollandite and $\text{K}_{0.6}\text{Na}_{0.4}\text{AlSi}_3\text{O}_8$ hollandite in LiF have been calculated. The variation of $(e_1 - e_2)$ as a function of pressure is used as order parameter variation, since $(e_1 - e_2) \propto Q$, in Figures 4.7 and 4.8. These results show that the deviatoric stress arising from LiF are very large and no indication of a “real” transition pressure can be obtained.

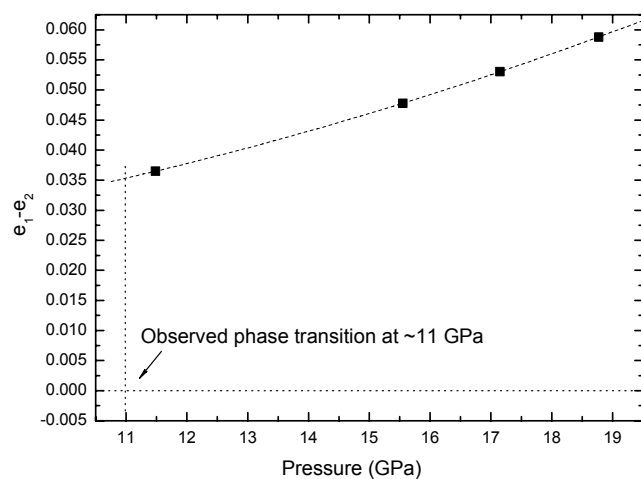


Figure 4.7. Order parameter behaviour described in terms of the symmetry-breaking strain $e_1 - e_2$ for the $4/m - 2/m$ transition in $K_{0.8}Na_{0.2}AlSi_3O_8$ hollandite obtained from the experiment with LiF as pressure transmitting medium. Splitting of the diffraction lines was observed at ~ 11 GPa. If compared to the results obtained for the same hollandite sample under hydrostatic condition (Figure 3.16), the stress effect appears to be significant.

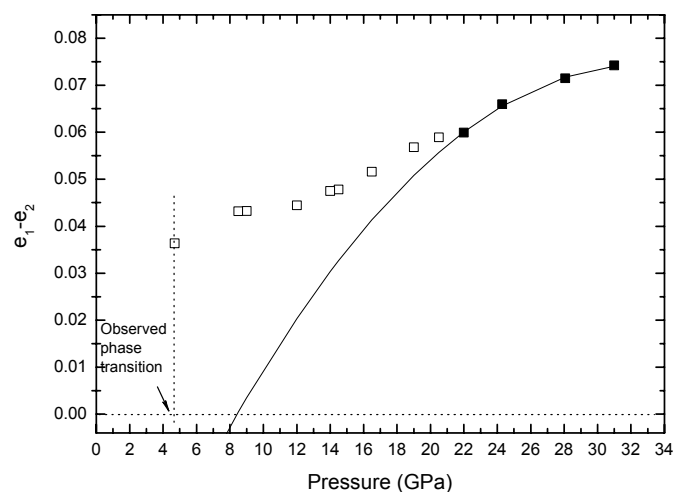


Figure 4.8. Order parameter behaviour described in terms of the symmetry-breaking strain $e_1 - e_2$ for the $4/m - 2/m$ transition in $K_{0.6}Na_{0.4}AlSi_3O_8$ hollandite obtained from the experiment with LiF as pressure transmitting medium. Splitting of the diffraction lines was observed at ~ 5 GPa. The extrapolated curve from the high pressure data gives a transition pressure still lower than expected (see Figure 4.3).

5. Conclusions

Using $(\text{Na}_{0-0.6}, \text{K}_{1-0.4})\text{AlSi}_3\text{O}_8$ glasses as starting materials, in experiments performed on multi-anvil apparatus in the pressure range between 13 and 26 GPa and temperatures between 1500 and 2200 °C, homogeneous assemblages with a pure hollandite phase were synthesized with 0%, 10%, 30%, 40%, 50% of Na component. The unit-cell volume and lattice parameters of $(\text{Na},\text{K})\text{AlSi}_3\text{O}_8$ hollandite decrease linearly with increasing Na content. Structural refinements of crystals of KAlSi_3O_8 end-member and of $\text{K}_{0.8}\text{Na}_{0.2}\text{AlSi}_3\text{O}_8$ hollandite indicate that Na occupies preferentially a split site away from the 4-fold axis, and closer to the framework walls, probably as a consequence of the small size of the Na atom with respect to the tunnel size of the hollandite tetragonal structure. The $\text{Si}(\text{Al})\text{O}_6$ octahedra in KAlSi_3O_8 and $\text{K}_{0.8}\text{Na}_{0.2}\text{AlSi}_3\text{O}_8$ hollandite are more distorted than in stishovite, due to the presence of the tunnel cations and to the substitution of Al^{3+} for Si^{4+} in the octahedral framework.

All experiments conducted using $\text{NaAlSi}_3\text{O}_8$ albite glasses as starting material failed in producing a $\text{NaAlSi}_3\text{O}_8$ hollandite end-member. This has been attributed to the difference in heat dissipation between the shock events in meteorites and the multi-anvil presses. Some experiments were done using a $\text{Na}_{0.75}\text{K}_{0.05}\text{Ca}_{0.1}\text{AlSi}_3\text{O}_8$ glass to simulate the cation substitution presented in the natural $\text{NaAlSi}_3\text{O}_8$ hollandite in some meteorite. In this case the run product was a complex mixture of phases among which a hollandite phase with composition $\text{K}_{0.26}\text{Na}_{0.53}\text{Ca}_{0.16}\text{Al}_{1.15}\text{Si}_{2.86}\text{O}_8$. The ratio $\text{Na}/(\text{Na}+\text{K}+\text{Ca}) = 0.56$ in this hollandite is larger than the $\text{Na}/(\text{Na}+\text{K})$ ratio of any other experiment performed in this study, also suggesting that a certain amount of cations larger than Na are necessary to stabilize the hollandite structure.

Experiments on high pressure behaviour of hollandite samples with compositions of KAlSi_3O_8 , $\text{K}_{0.8}\text{Na}_{0.2}\text{AlSi}_3\text{O}_8$, $\text{K}_{0.6}\text{Na}_{0.4}\text{AlSi}_3\text{O}_8$, and $\text{K}_{0.5}\text{Na}_{0.5}\text{AlSi}_3\text{O}_8$ show that all hollandite samples transform to the monoclinic structure at high pressure. The phase transition pressure decreases with increasing Na content. The transition pressure for $\text{K}_{0.8}\text{Na}_{0.2}\text{AlSi}_3\text{O}_8$ hollandite has been determined to be 17.5 GPa. The presence of Na substitution in the tunnel, therefore, decreases the transition pressure with respect to the KAlSi_3O_8 hollandite end-member, which transforms to monoclinic phase at ~20 GPa. A simple extrapolation of a linear fit through the

transition pressures of KAlSi_3O_8 and $\text{K}_{0.8}\text{Na}_{0.2}\text{AlSi}_3\text{O}_8$ hollandite indicates that the phase transition pressure of $\text{NaAlSi}_3\text{O}_8$ hollandite may be at ~ 7.5 GPa at room temperature. The tetragonal $I4/m$ to monoclinic $I2/m$ phase transition in hollandite is proper ferroelastic with negligible volume strain and is second-order in character. Comparison of the strain behaviours between $\text{K}_{0.8}\text{Na}_{0.2}\text{AlSi}_3\text{O}_8$ and KAlSi_3O_8 hollandite shows no significant difference in the phase transition mechanism. The bulk modulus of tetragonal hollandite, is not affected by the Na substitution, however the anisotropic behaviour of the axial compressibility increases with increasing Na content. Monoclinic hollandite are more compressible than the tetragonal low-pressure form, and are stable up to the maximum pressures reached in the experiments, suggesting that such phases may, indeed, be potential host minerals for Na and K in the transition zone and even down into the lower mantle. The high temperature and high pressure behaviour of $\text{K}_{0.5}\text{Na}_{0.5}\text{AlSi}_3\text{O}_8$ hollandite indicates a positive Clayperon slope.

The tetragonal to monoclinic high-pressure phase transformation is very sensitive to the presence of deviatoric stresses. A Landau excess free-energy expansion has been used to show how, even for “mild” stresses created in a soft medium as LiF, the monoclinic structure is the stable at any pressure, preventing a quantitative characterization of the transition.

References

Adams, B. L., Wright, S. I., and Kunze, K (1993). Orientation imaging: the emergence of a new microscopy. *Metallurgical Transactions*, 24A: 819-833.

Ahmed-Zaïd, I., and Madon, M. (1995). Electron microscopy of high pressure phases synthesized from natural garnets in a diamond anvil cell: Implications for the mineralogy of the lower mantle. *Earth and planetary science letters*, 129:233-247.

Ahmed-Zaïd, I., and Madon, M. (1991). A high-pressure form of Al_2SiO_5 as a possible host of aluminium in the lower mantle. *Nature*, 353: 426-428.

Ahrens, T. J., Liu, L. (1973) A shock-induced phase change in orthoclase. *Journal of Geophysical Research*, 78, 1274-1278.

Ahrens, T. J., Petersen C. F., Rosenberg, J., T.(1969) Shock compression of feldspars. *Journal of Geophysical Research*, 74, 2727-2746.

Akaogi, M. (2000). Clues from a shocked meteorite. *Science*, 287: 1602-1603.

Anderson, O. L. (1995). Equation of state of solids for geophysics and ceramic science. Oxford University Press, Oxford, UK.

Anderson, O. L., Isaak, D. G., Yamamoto, S. (1989). Anharmonicity and the equation of state for gold. *Journal of Applied Physics*, 65(4): 1534-1543.

Angel, R. J. (2000). Equation of state. In Hazen, R. M. and Downs, R. T. (eds): *Review in mineralogy and geochemistry volume 41: High-temperature and high-pressure crystal chemistry*: 35-59. The Mineralogical Society of America, Washington, DC 20036 U.S.A.

Angel, R. J. (2002) Eosfit52t.exe. Crystallography laboratory, department of geological sciences. Virginia Tech, Blacksburg, USA.

Armstrong, R. L. (1981). Radiogenic isotopes: The case for crustal recycling on a near-steady state no-continental growth earth. *Philosophical transactions of the Royal Society A*, 301: 443-472.

Bayer, G. and Hoffman, W. (1966). Complex alkali titanium oxides $A_x(B_yTi_{8-y})O_{16}$ of the α - MnO_2 structure-type. *American mineralogist*, 51: 511-516.

Birch, F. (1947). Finite elastic strain of cubic crystals. *Phys. Rev.* 71: 809-824

Birch, F (1978). Finite strain isotherm and velocities for single crystal and polycrystalline NaCl at high pressures and 300K. *Journal of Geophysical Research*, 83, 1257-1268.

Birch, F. and LeComte, P. (1960). Temperature-pressure plane for albite composition. *American Journal of Science*, 258: 209-217.

Blessing, R. H. (1995) An empirical correction for absorption anisotropy. *Acta Crystallographica A*, 51: 33-38.

Bolfan-Casanova, N. (2000). The distribution of water in the earth's mantle: an experimental and infrared spectroscopic study. (PhD thesis) Bayerisches Geoinstitut.

Cadee, M. C., and Verschoor, G. C. (1978). Barium tin chromium oxide, a new hollandite phase. *Acta Crystallographica*, B34: 3554-3558.

Canil, D. (1994). Stability of clinopyroxene at pressure-temperature conditions of the transition zone, *Physics of the Earth and Planetary Interiors*, 86:25-34.

Carpenter, A. A., Salje, E. K. H., and Graeme-Barber, A. (1998). Spontaneous strain as a determinant of thermodynamic properties for phase transitions in minerals. *European Journal of Mineralogy*, 10:621-691.

Cheary, R. W. (1986). An analysis of the structural characteristics of hollandite compounds. *Acta Crystallographica*, B42: 229-236

Chervin, J. C., Canny, B., Gauthier, M., and Pruzan, P. (1993). Micro-Raman at variable low-temperature and very high pressure. *Review of Scientific Instruments*, 64: 203-206.

Chopin, C. (1984). Coesite and pure pyrope in high-grade blueschists of the Western Alps: a first record and some consequences. *Contributions to Mineralogy and Petrology*, 86: 107-118.

Cohen, R. E. (1992). First-principles predictions of elasticity and phase transitions in high pressure SiO₂ and geophysical implications. In: *High-Pressure Research: Application to Earth and Planetary Sciences*. Syono, Y., Manghnani, M. H., 425-431. Terra Scientific, Tokyo-Am Geophs Union, Washington DC.

Collerson, K. D., Hapugoda, S., Kamber, B. S., and Williams, Q. (2000). Rock from the mantle transition zone: majorite-bearing xenoliths from Malatia, Southwest Pacific. *Science*, 288: 1215-1233.

Deer, W. A., Howie, R. A., and Zussman, J. (1966). An introduction to the rock-forming minerals. Longmans, London.

Domanik, K. J., and Holloway, J. R. (1996). The stability and composition of phengitic muscovite and associated phases from 5.5 to 11 GPa: Implications for deeply subducted sediments. *Geochimica et Cosmochimica Acta*, 60: 4133-4150.

Domanik, K. J., and Holloway, J. R. (2000). Experimental synthesis and phase relations of phengitic muscovite from 6.5 to 11 GPa in a calcareous metapelite from the Dabie Mountains, China. *Lithos*, 52: 51-77.

Downs, R. T., Hazen, R. M., Finger, L. W., and Gasparik, T. (1995). Crystal chemistry of lead aluminosilicates hollandite: a new high-pressure synthetic phase with octahedral Si. *American Mineralogist*, 80: 937-940.

Dubrovinskaia, N., Dubrovinsky, L. (2003). Whole-cell heater for the diamond anvil cell. *Review of Scientific Instruments*, 74: 3433-3437.

Dubrovinsky, L., Dubrovinskaia, N., Crichton, W. A., Mikhaylushkin, A. S., Simak, S. I., Abrikosov, I. A., de Almeida, J. S., Ahuja, R., Luo, W., and Johansson, B. (2007). Noblest of all metals is structurally unstable at high pressure - art. *Physical Review Letters*, 98 (4): 5503-5503.

Dubrovinsky, L., Dubrovinskaia, N., Kantor, I., McCammon, C., Crichton, W., Urusov, V. (1997). Decomposition of ferropericlase ($\text{Mg}_{0.80}\text{Fe}_{0.20}\text{O}$) at high pressures and temperatures. *Journal of Alloys and Compounds*. 390: 41-45.

Dubrovinsky, L., Dubrovinskaia, N., Kantor, I., Nestola, F., and Gatta, D. (2006). High-Brilliance X-ray System for High-Pressure In-House Research: Applications for Studies of Superhard Materials. *High Pressure Research*, 26: 137-143.

Dubrovinsky, L. S., Saxena, S. K., Tutti, F., and Le Bihan, T. (1999). In situ X-ray study of thermal expansion of iron at multimegabar pressure. *High Pressure-High temperature*. 31: 553-559.

Dobrzhinetskaya, L. F. And Green, H. W. (2007). Experimental studies of mineralogical assemblages of metasedimentary rocks at Earth's mantle transition zone conditions. *Journal of metamorphic geology*, 25: 83-96.

Duffy, T. S., Wang, Y. (1998). Pressure-volume-temperature equations of state. In Hemley, R. J. (ed) Ultra-high-pressure mineralogy. *Reviews in Mineralogy*, 33: 425-457.

Dupre, B. and Allegre, C. (1983). Pb-Sr isotope variation in Indian Ocean basalts and mixing phenomena. *Nature*, 303: 142-146.

Endo, T., Kume, S., Kinomura, N., and Koizumi, M. (1976). A new compound $K_2Cr_8O_{16}$ with hollandite type structure. *Materials research bulletin*, 11, 609-614.

Eremets, M. (1996). *High Pressure Experimental Methods*, Oxford University Press, New York.

Faruggia, L. (1999) WinGX suite for single crystalsmall molecule crystallography. *Journal of applied crystallography*, 32: 837-838

Fateley, W. G., Dollish, N. T., McDewitt, N. T., Bentley, F. R. (1971). Infrared and Raman selection rules for molecular and lattice vibrations. Wiley-Interscience, New York.

Faust, J. and Knittle, E. (1994). The equation of state, amorphization, and high-pressure phase diagram of muscovite. *Journal of Geophysical Research*, 99: 19785-19792.

Fei, Y., Saxena, S. K. And Navrotsky, A. (1990). Internally consistent thermodynamic data and equilibrium phase relations for compounds in the system $MgO-SiO_2$ at high pressure and high temperature, *Journal of Geophysical Research*, 95: 6915-6928.

Fei, Y. and Wang, Y. (2000). High-temperature and high-pressure powder diffraction. In Hazen, R. M. and Downs, R. T. (eds.): *high-temperature and high-pressure crystal chemistry / Review in Mineralogy and Geochemistry*, 41/. Washington (D. C.):Mineral. Soc. Am., 521-557.

Ferraro, J. R. (1984). Vibrational spectroscopy at high external pressures- The diamond anvil cell. New York (N.Y.): Academic Press, 264 p.

Ferroir, T., Onozawa, T., Yagi, T., Merkel, S., Miyajima, N., Nishiyama, N., Irifune T., and Kikegawa, T. (2006) Equation of state and phase transition in $KAlSi_3O_8$ hollandite at high pressure. *American Mineralogist*, 91, 327-332.

- Finger, L. W., and Hazen, R. M. (1991). Crystal chemistry of six-coordinated silicon: a key to understanding the Earth's deep interior. *Acta Crystallographica*, B47: 561-580.
- Funamori, N., Jeanloz, R. Z., Nguyen, J. H., Kavner, A., Cldwell, W. A., Fijino, K., Miyajima, N., Shinmei, T., and Tomioka, N. (1998). High-pressure transformations in MgAl_2O_4 . *Journal of Geophysical Research*, 103, 20813-20818.
- Gasparik, T., Tripathi, A., and Parise, J. B. (2000). Structure of a new Al-rich phase, $(\text{K}, \text{Na})_{0.9}(\text{Mg}, \text{Fe}, \text{Al}, \text{Si})_6\text{O}_{12}$, synthesized at 24GPa. *American Mineralogist*, 85: 613-618.
- Gautron, L., Fitz Gerald, J. D., Kesson, S. E., Eggleton, R. A., and Irifune, T. (1997). Hexagonal Ba-ferrite: a good model for the crystal structure of a new high-pressure phase $\text{CaAl}_4\text{Si}_2\text{O}_{11}$? *Physics of the Earth and planetary Interiors*, 102: 223-229.
- Gillet, P. (1996). Raman spectroscopy at high pressure and high temperature. Phase transitions and thermodynamic properties of minerals. *Physics and chemistry of minerals*, 23: 263-275.
- Gillet, P., Chen, M., Dubrovinsky, L. S., and El Goresy, A. (2000). Natural $\text{NaAlSi}_3\text{O}_8$ -holandite in the shocked Sixianglou meteorite. *Science*, 287: 1633-1636.
- Gillet, P., Hemley, R. J., and McMillan P. F. (1998). Vibrational properties at high pressures and temperatures. In Hemley, R. J. (ed): *Ultrahigh-pressure mineralogy – Physics and chemistry of the Earth's deep interior / Reviews in Mineralogy*, 37/. Washington (D.C.): Mineral. Soc. Am., 525-590.
- Graham (1987). The multianvil press. In Sammis, C. G. And Henyey, T. L., editors, *Geophysics Part A, Laboratory Measurements*, Methods of experimental physics. Academic Press, Orlando.
- Hall, H. T. and Murthy, V. R. (1971). The early chemical history of the Earth: some critical elemental fractionations. *Earth and planetary science letters*, 11:239-244.

Harris, J. W., Hutchison, M. T., Huesthouse, M., Light, M., and Harte, B. (1997). A new tetragonal silicate mineral occurring as inclusions in lower-mantle diamonds. *Nature*, 387: 486-488.

Hazen, R. J., Finger, L. W. (1982). *Comparative Crystal Chemistry*, John Willey & Sons, New York.

Heinz, D. L. And Jeanloz, R. (1984). The equation of state of the gold calibration standard. *Journal of applied physics*. 55 (4): 885-893.

Hemley, R. J. (ed.) (1998), *ultrahigh-pressure Mineralogy*, *Rev. Mineralogy* 37, New York.

Hemley, R.J., Mao, H., and Chao, E. (1986). Raman spectrum of Natural and Synthetic stishovite. *Physics and Chemistry of Minerals*, 13: 285-290.

Hemley, R. J., Prewitt C. T., and Kingma, K. J. (1994). High-pressure behaviour of silica. In: *Reviews in Mineralogy volume 29: Silica: Physical Behavior, Geochemistry and Materials Applications*. Heaney, P. J., Prewitt, C. T., and Gibbs, G. V. 41-81. Mineralogical Society of America, Washington, DC.

Hofmann, A. W. (1997). Mantle geochemistry: The message from oceanic volcanism, *Nature*, 385: 219-229.

Holzapfel, C., (2004). Fe-Mg interdiffusion at high pressures in mineral phases relevant for the Earth's mantle. PhD thesis. Bayerisches Geoinstitut

International tables for crystallography, Vol. C (1992) Ed. A.J.C. Wilson, Kluwer Academic Publishers, Dordrecht, The Netherlands.

Irifune, T. (2002). Application of synchrotron radiation and Kawai-type apparatus to various studies in high pressure mineral physics. *Mineralogical Magazine*, 66(5):769-790.

Irifune, T. (1994). Absence of an aluminous phase in the upper part of the Earth's lower mantle. *Nature*, 370:131-133.

Irifune, T., Fujino, K., and Ohtani, E. (1991). A new high-pressure form of MgAl_2O_4 . *Nature*, 349: 409-411.

Irifune, T., Koizumi, T., and Ando, J. (1996). An experimental study of the garnet-perovskite transformation in the system $\text{MgSiO}_3\text{-Mg}_3\text{Al}_2\text{Si}_3\text{O}_{12}$. *Physics of the Earth and Planetary Interiors*, 96: 147-157.

Irifune, T., Ringwood, A. E., and Hibberson, W. O. (1994). Subduction of continental crust and terrigenous and pelagic sediments: an experimental study. *Earth and Planetary Science Letters*, 126: 351-368.

Jayaraman, A. J. (1983). Diamond anvil cell and high-pressure physical investigations. *Review of Modern Physics*, 55: 65-85.

Jayaraman, A. J. (1986). Ultrahigh pressures. *Review of Scientific Instruments*, 57: 1013-1031.

Kawai, N. and Endo S., (1970). The generation of ultrahigh hydrostatic pressures by a split sphere apparatus. *Review of Scientific Instruments*, 41: 1178-1181.

Kawai, N., Togaya, M., and Onodera, A. (1973). *Proceedings of the Japan Academy*, 49:623-626.

Kenichi, T. (2001). Evaluation of the hydrostaticity of a helium-pressure medium with powder x-ray diffraction techniques. *Journal of applied physics*. 89(1): 662-668.

Kesson, S. E., Fitz Gerald, J. D., and Shelley, J. M. G. (1998). Mineralogy and dynamics of a pyrolite lower mantle. *Nature*, 393: 252-255.

Kimura, M. Chen, M., Yoshida, Y., El Goresy, A., and Ohtani, E. (2003). Back-transformation of high-pressure phases in a shock melt vein of an H-chondrite during atmospheric passage: implications for the survival of high-pressure phases after decomposition. *Earth and Planetary Science Letters*, 217: 141-150.

Kimura, M., Suzuke, A., Kondo, T., Ohtani, E., and El Goresy, A. (2000). Natural occurrence of high-pressure phases. Jadeite, hollandite, wadsleyite and majorite-pyropes in an H-chondrite, Y75100. *Meteorites and Planetary Science*, 35: A87-88.

Kingma, K. J., Cochen, R. E., Hemley, R. J., and Mao, H. (1995). Transformation of stishovite to a denser phase at lower-mantle pressures. *Nature*, 374: 243-245.

Kinomura, N., Kume, S., and Koizumi, M. (1975). Stability of $K_2Si_4O_9$ with wadeite type structure. *Proceedings of the 4th International Conference on High Pressure Science and Technology*, 211-214.

Kondo, T. and Yagi, T. (1998). Phase transition of pyrope garnet under lower mantle conditions. In M. H. Manghnani and T. Yagi, Eds., *Properties of Earth and Planetary Materials at High Pressure and Temperature*. Geophysical Monograph 101, p. 419-427. American Geophysical Union, Washington DC.

Konzett, J. and Fei, Y. (2000). Transport and storage of potassium in the Earth's upper mantle and transition zone: an experimental study to 23 GPa in simplified and natural bulk compositions. *Journal of Petrology*, 41: 583-603.

LABSPEC v 2.07 (1997). DILOR SA & UNIVERSITE DE REIMS.

Langenhorst, F., Poirier, J. P. (2000). 'Eclogitic' minerals in a shocked basaltic meteorite. *Earth and Planetary Science Letters*, 176: 259-265.

Larson, A and Van Dreele, R. B. (1994). GSAS general structure analysis system. Los Alamos National Laboratory, New Mexico, USA.

- Lewis, J. S. (1971). Conferences of the presence of sulphur in the core of the Earth. *Earth and planetary science letters*, 11:130-134.
- Liebermann, R. C. and Wang, Y. (1992). Characterization of sample environment in a uniaxial split-sphere apparatus. In Syono, Y. And Manghnani, M. H., editors, *High-pressure research: Application to earth and planetary sciences*. American Geophysical Union, Washington, D. C.
- Liu, L. (1977). High Pressure NaAlSiO₄: The First Silicate Calcium Ferrite Isotype. *Geophysical research letters*, 4: 183-186.
- Liu, L. (1978a) High-pressure phase transformations of albite, jadeite and nepheline. *Earth and planetary Science Letters*, 37, 438-444.
- Liu, L.(1978b), High-pressure phase transitionis of kalsilite and related potassium bearing aluminosilicates. *Geochemical Journal*, 12:275-277.
- Liu, L. and El Goresey, A. (in press) High-pressure phase transitions of the feldspars and future characterization of lingunite.
- Liu, X. (2006). Phase relations in the system $KAlSi_3O_8$ - $NaAlSi_3O_8$ at high pressure-high temperature conditions and their implication for the petrogenesis of lingunite. *Earth and Planetary Science Letters*, 246: 317-325.
- Loewenstein, W. (1954). The distribution of aluminum in the tetrahedra of silicates and aluminates. *American Mineralogist*, 39: 92-96.
- Madon, M., Castex, J., and Peyronneau, J. (1989). A new aluminocalcic high-pressure phase as a possible host of calcium and aluminium in the lower mantle. *Nature*, 342: 422-424.

Mao, H. K., Bell, P. M., Shaner, J. W., and Steinberg, D. J. (1978). Specific volume measurements of Cu, Mo, Pd, and Ag and calibration of the ruby R1 fluorescence pressure gauge from 0.06 to 1 Mbar. *Journal of applied physics*, 49: 3276-3283.

Mao, H. K., Xu, J., Bell, P. M. (1986). Calibration of the ruby pressure gauge to 800 kbar under quasi-hydrostatic conditions. *Journal of Geophysical Research*, 91: 4673–4676.

McMahon, M. I. (2004). High pressure diffraction from good powders, poor powders and poor single crystals. In Katrusiak, A. And McMillan, P. (eds.): *high-pressure crystallography /NATO Science. Series. 140/*. Dordrecht: kluwer, 1-20.

Miletich, R., Allan, D. R., and Kuhs, W. F. (2000). High-pressure single-crystal techniques. In *Reviews in mineralogy and geochemistry volume 41: High-temperature and high-pressure crystal chemistry*, 445-519. Edited by Hazen, R. M. and Downs. Mineralogical Society of America, Washington DC.

Miyajima, N., Fujino, K., Funamori, N., Kondo, T., and Yagi, T. (1999). Garnet-perovskite transformation under the conditions of Earth's lower mantle: an analytical transmission electron microscopy study. *Physics of the Earth and Planetary Interiors*, 116: 117-131.

Miyajima, N., Yagi, T., Hirose, K., Kondo, T., Fujino, K., and Miura, H. (2001). Potential host phase of aluminium and potassium in the Earth's lower mantle. *American Mineralogist*, 86: 740-746.

Mori, H. (1994). Shock-induced phase transformations of the earth and planetary materials. *Journal of the Mineralogical Society of Japan*, 23: 171-178.

Mori, H. (1990). Hollandite type NaAlSi₃O₈ in shocked meteorites. In: *31st High Pressure Conference of the Japan Society of High Pressure Science and Technology*, 134-135. Osaka, 1990.

Murthy, V., A., Westrenen, W., V., and Fei, Y. (2003) Experimental evidence that potassium is a substantial radioactive heat source in planetary cores. *Nature*, 423, 163-165.

Nasdala, L., Smith, D. C., Kaindl, R., and Ziemann, M. A. (2004). Raman spectroscopy: Analytical perspectives in mineralogical research. In Beran, A. and Libowitzky, E.(2004): *EMU Notes in Mineralogy, Vol. 6: Spectroscopic Methods in Mineralogy*. Eötvös University Press, Budapest. 281-243.

Nishiyama, N., Rapp, R. P., Irifune, T., Sanehira, T., Yamazaki, D., and Funakoshi, K. (2005). Stability and *P-V-T* equation of state of KAlSi_3O_8 -hollandite determined by in situ X-ray observations and implications for dynamics of subducted continental crust material. *Physics and Chemistry of Minerals*, 32: 627-637.

Oguri, K., Funamori, N., Uchida, T., Miyajima, N., Yagi, T., and Fujino, K. (2001). Post-garnet transition in a nature pyrope: a multi-anvil study based on in situ X-ray diffraction and transmission electron microscopy. *Physics of the Earth and Planetary Interiors*, 122: 175-186.

Ohtani, E., Irifune, T., Hibberson, W., and Ringwood, A. E.(1987). Modified split-sphere guide block for practical operation of a multi-anvil apparatus. *High Temperatures-high pressures*, 19:523-529.

Ohtani, E., Kimura, M., Takata, T., Kondo, T., and Kubo, T. (2004). Formation of high-pressure minerals in shocked L6 chondrite Yamato 791384: constraints on shock conditions and parent body size. *Earth and Planetary Science Letters*, 227: 505-515.

Ono, S. (1998). Stability limits of hydrous minerals in sediment and mid-ocean ridge basalt compositions: Implications for water transport in subduction zones. *Journal of Geophysical Research*, 103: 18253-18267.

Oxford Diffraction (2006). Oxford Diffraction Ltd., Xcalibur CCD system, CrysAlis Software system, Version 171.30.2

Paszkowicz, W. (2002). High-pressure powder X-ray diffraction at the turn of the century. *Nuclear Instruments and Methods in Physics Research, B*, 198:142-182.

Perraki, M., Proyer, A., Mposkos, E., Kaindl, R. & Hoinkes, G. (2006). Raman micro-spectroscopy on diamond, graphite and other carbon polymorphs from the ultrahigh-pressure metamorphic Kimi Complex of the Rhodope Metamorphic Province, NE Greece. *Earth and Planetary Science Letters*: 241, 672–685.

Post, J. E. and Burnham, C. W. (1986) Modeling tunnel-cation displacements in hollandites using structure-energy calculations. *American Mineralogist*, 71: 1178-1185.

Post, J. E., Von Dreele, R. B., and Buseck, P. R. (1982). Symmetry and cation displacements in hollandites: structure refinements of hollandite, cryptomelane and priderite. *Acta Crystallographica*, B 38: 1056-1065.

Reid, A. F., Wadsley, A. D., and Ringwood, A. E. (1967). High pressure NaAlGeO_4 , a calcium ferrite isotype and model structure of silicates at depth in the earth's mantle *Acta Crystallographica*, 23: 736-739.

Reid, A. F. and Ringwood, A. E. (1969). Six-coordinate silicon: high pressure strontium and barium aluminosilicates with the hollandite structure. *Journal of Solid state Chemistry*, 1: 6-9.

Reid, J. (2002). Transport properties of silicate liquids at high pressure. PhD thesis. Bayerisches Geoinstitut.

Reimer, L. (1998). *Scanning Electron Microscopy*. Springer Verlag, Berlin.

Ringwood, A. E. (1991). Phase transformations and their bearing on the constitution and dynamics of the mantle. *Geochimica et Cosmochimica Acta*, 55: 2083–2110.

- Ringwood, A. E. and Major, A. (1967). Some high-pressure transformations of geophysical significance. *Earth and planetary science letters*, 2: 106-110.
- Ringwood, A. E., Reid, A. F., and Wadsley, A. D. (1967). High-pressure KAlSi_3O_8 , an aluminosilicate with sixfold coordination. *Acta Crystallographica*, 23: 1093-1095.
- Ross, N. L., Shu, J. F., and Hazen, R. M. (1990). High-pressure crystal chemistry of stishovite. *American mineralogist*, 75: 739-747.
- Rubie, D. C. (1999). Characterizing the sample environment in multianvil high-pressure experiments. *Phase Transitions*, 68: 431-451.
- Rubie, D. C., Karato, S., Yan, H., and O'Neill, H. S. C. (1993). Low differential stress and controlled chemical environment in multianvil high-pressure experiments. *Physics and Chemistry of Minerals*, 20: 315-322.
- Toby, B. H. (2001) EXPGUI, a graphical user interface for GSAS. *Journal of Applied Crystallography* (2001).
- Salje, E. K. H. (1993). Phase transitions in ferroelastic and co-elastic crystals (student edition). University Press, Cambridge.
- Schmidt, M. W. (1996). Experimental constraints on recycling of potassium from subducted oceanic crust. *Science*, 272: 1927-1930.
- Sekine, T., Ahrens, T. J. (1992) Shock-induced transformations in the system $\text{NaAlSiO}_4\text{-SiO}_2$: a new interpretation. *Physics and Chemistry of Minerals*, 18, 359-364
- Shannon, R. D. and Prewitt, C. T. (1969). Effective ionic radii in oxides and fluorides. *Acta Crystallographica*, B25: 925-945.

Sheldrick, G. M. (1997) SHELX-97. Programs for crystal structure determination and refinement. University of Göttingen, Germany

Shimomura, O., Yamaoka, S., Nakazawa, H., and Fukunaga, O. (1982). *High-pressure Research in Geophysics*, edited by S. Akimoto and M. H. Manghnani (center for Academic Publishing, Tokyo), p49.

Sinclair, W., McLaughlin, G. M., and Ringwood, A. E. (1980). The structure and chemistry of a barium titanate hollandite-type phase. *Acta Crystallographica*, B36, 2913-2918.

Smith, D. (1984). Coesite in clinopyroxene in the Caledonides and its implications for geodynamics. *Nature*, 310: 641–644.

Sobolev, N. V. and Shatsky, V. (1990). Diamond inclusions in garnets from metamorphic rocks: A new environment for diamond formation. *Nature*, 343: 742-746.

Sommerville, M. and Arhens, T. J. (1980). Shock compression of KFeS₂ and question of potassium in the core. *Journal of Geophysical Research*, 85: 7016-7024.

Spain, I. L. and Paauwe, J. (1977). *High Pressure Technology*, volume 1. Marcel Dekker, Inc, New York.

Spengler, D., van Roermund, H. L. M., Drury, M., Ottolini, L., Maso, P. R. D. & Davies, G. (2006). Deep origin and hot melting of an Archaean orogenic peridotite massif in Norway. *Nature*, 440, 913–917.

Stacey, F. D., Brennan, B. J., and Irvine, R. D. (1981). Finite strain theories and comparisons with seismological data. *Geophysical Survey*, 4: 189-232.

Sueda, Y., Irifune, T., Nishiyama, N., Rapp, R. P., Ferroir, T., Onozawa, T., Yagi, T., Merkel, S., Miyajima, N., and Funakoshi, K. (2004). A new high-pressure form of KAlSi₃O₈ under lower mantle conditions. *Geophysical research letters*, 31: L23612.

Takzawa, E., Sekine, T., Kobayashi, T., and Zhu, Y. (1998) Hugoniot equation of state and high-pressure transformation of jadeite. *Journal of Geophysical Research*, 103:B6, 12261-12268.

Tomioka, N., Mori, H., and Fujino, K. (2000). Shock-induced transition of NaAlSi₃O₈ feldspar into a hollandite structure in a L6 chondrite. *Geophysical Research Letters*, 27, 3997-4000, 2000.

Tutti, F., Dubrovinsky, L. S., and Saxena, S. K. (2001). Stability of KAlSi₃O₈ hollandite-type structure in the Earth's lower mantle conditions. *Geophysical Research Letters*, 28:2735-2738.

Urakawa, S., Kondo, T., Igawa, N., Shimomura, H., Ono, H. (1994). Synchrotron radiation study on the high-pressure and high-temperature phase relations of KAlSi₃O₈. *Physics and chemistry of minerals*, 21: 387-391.

Van Roermund, H. L. M. & Drury, M. R. (1998). Ultra-high pressure ($P > 6$ GPa) garnet peridotites in Western Norway: exhumation of mantle rocks from >185 km depth. *Terra Nova*, 10: 295–301.

Walker, d., Carpenter, M. A., and Hitch, C. M. (1990). Some simplifications to multianvil devices for high pressure experiments. *American Mineralogist*, 75: 1020-1028.

Wang, W. and Takahashi, E. (2000). Subsolidus and melting experiments of a K-doped peridotite KLB-1 to 27 GPa: Its geophysical and geochemical implications. *Journal of Geophysical Research*, 105: 2855-2868.

Wang, W. and Takahashi, E. (1999). Subsolidus and melting experiments of a K-rich basaltic composition to 27 GPa: Implication for the behaviour of potassium in mantle. *American Mineralogist*, 84: 357-361.

- Wasserburg, G. J., MacDonald, G. J. F., Hoyle, F., Flower, W. A. (1964). Relative contributions of uranium, thorium, and potassium to heat production in the Earth. *Science*, 143: 464-467.
- Watanabe, M., Fujiki, Y., Kanazawa, Y., Tsukimura, K. (1987). The effects of cation substitution on the hollandite-type structure. *Journal of Solid State Chemistry*, 66, 56-63
- Wendland, R. F. and Eggler, D. H. (1980). The origins of potassic magmas: 1. melting relations in the system $\text{KAlSiO}_4\text{-Mg}_2\text{SiO}_4\text{-SiO}_2$ and $\text{KAlSiO}_4\text{-MgSiO-SiO}_2\text{-CO}_2$ to 30 kilobars. *American Journal of Science*, 280: 385-420.
- Wunder and Schoen, S. L. (1978). *Journal of applied physics*. 49, 3276.
- Xie, S., Chen, M., and Wang, D. (2001). Shock-related mineralogical features and P-T history of the Suizhou L6 chondrite, *Eur. J. Mineral.*, 13: 1177-1190.
- Xie, X., Chen, M., Wang, D., and El Goresey, A. (2001). $\text{NaAlSi}_3\text{O}_8$ -hollandite and other high-pressure minerals in the shock melt veins of the Suizhou meteorite. *Chinese Science Bulletin*, 46: 1121-1126.
- Yagi, A., Suzuki, T., and Akaogi, M. (1994) High-pressure transitions in the system KAlSi_3O_8 - $\text{NaAlSi}_3\text{O}_8$. *Physics and Chemistry of Minerals*, 21, 12-17.
- Yagi, T. (1978). Experimental determination of thermal expansivity of several alkali halides at high pressures. *Journal of Physics and Chemistry of Solids* 39: 563-571.
- Yamada, H., Matsui, Y., and Ito, E. (1984). Crystal-chemical characterization of KAlSi_3O_8 with the hollandite structure. *Mineralogical Journal*, 12: 29-34.
- Yamada, H., Matsui, Y. and Ito, E. (1983). Crystal-chemical characterization of NaAlSiO_4 with the CaFe_2O_4 structure. *Mineralogical Magazine*, 47:177-181.

Yang, J., Xu, Z., Dobrzhinetskaya, L. F., Harry W. Green II, Xianzhi Pei, Rendeng Shi, Cailai Wu, Joseph L. Wooden, Jianxin Zhang, Yusheng Wan, Haibing Li (2003). Discovery of metamorphic diamonds in Central China: an indication of a >4000 km-long-zone of deep subduction resulting from multiple continental collisions. *Terra Nova*, 15: 370-379.

Yukutake, T. (2000). The inner core and the surface heat flow as clues to estimating the initial temperature of the Earth's core. *Physics of the Earth and Planetary interiors*, 121: 103-137.

Zhang J. and Burnham, C. W. (1994). Hollandite-type phases: geometric consideration of unit-cell size and symmetry. *American Mineralogist*, 79: 168-174.

Zhang, J., Ko, J., Hazen R. M., and Prewitt, C. (1993). High-pressure crystal chemistry of KAlSi_3O_8 hollandite. *American Mineralogist*, 78: 493-499.

Appendix 1: Indexed peaks in lattice parameter refinement

Sample S3436:

Peaklist [Range 1 : 2Theta = 9.993 119.833 0.020 I_{max} = 4037]

D-spacing	2Theta	I(rel)	I(abs)	I(int)	FWHM	H	K	L
6.590555	15.6007	51.14	2055	260.77	0.1000	1	1	0
4.661617	22.1253	49.64	1994	253.08	0.1000	2	0	0
3.297816	31.4755	36.40	1463	148.49	0.0800	2	2	0
2.949431	35.3086	100.00	4018	509.89	0.1000	3	1	0
2.616829	39.9755	23.12	929	94.31	0.0800	1	0	1
2.332523	45.0992	11.38	457	58.02	0.1000	4	0	0
2.282669	46.1403	44.55	1790	227.13	0.1000	2	1	1
2.086142	50.7795	21.06	846	107.36	0.1000	4	2	0
2.050278	51.7327	81.51	3275	332.47	0.0800	3	0	1
1.877048	56.9189	9.91	398	50.51	0.1000	3	2	1
1.829646	58.5344	10.93	439	66.85	0.1200	5	1	0
1.741320	61.8186	26.53	1066	162.31	0.1200	4	1	1
1.649462	65.6790	4.75	191	9.68	0.0400	4	4	0
1.600325	67.9648	3.87	155	35.48	0.1800	5	3	0
1.554976	70.2327	13.76	553	84.21	0.1200	6	0	0
1.540039	71.0162	4.76	191	19.43	0.0800	5	0	1
1.462327	75.4228	25.76	1035	131.36	0.1000	5	2	1
1.363582	81.9880	25.13	1010	128.11	0.1000	0	0	2
1.336737	84.0036	5.58	224	34.12	0.1200	6	1	1
1.318843	85.4114	3.33	134	17.62	0.1036	7	1	0
1.308492	86.2509	3.56	143	18.75	0.1033	2	0	2
1.285132	88.2177	20.43	821	145.86	0.1400	5	4	1
1.260188	90.4374	4.04	162	28.87	0.1400	2	2	2
1.237886	92.5372	14.57	585	118.83	0.1600	3	1	2
1.225149	93.7897	5.40	217	49.58	0.1800	7	3	0
1.177087	98.9128	3.67	147	22.44	0.1200	4	0	2
1.141365	103.2004	5.73	230	52.58	0.1800	4	2	2
1.099484	108.8879	4.87	196	29.83	0.1200	6	6	0
1.093398	109.7853	5.16	207	52.60	0.2000	5	1	2
1.084496	111.1346	4.56	183	23.24	0.1000	7	5	0
1.065301	114.2069	4.61	185	42.34	0.1800	8	1	1
1.050892	116.6772	4.31	173	13.17	0.0600	4	4	2
1.043264	118.0493	4.48	180	23.49	0.1028	8	4	0

Sample S3356:

Peaklist [Range 1 : 2Theta = 10.000 119.980 0.020 I_{max} = 33031]

D	2Theta	I(rel)	I(abs)	I(int)	FWHM	H	K	L
6.599476	15.5795	10.49	3351	439.87	0.1034	1	1	0
4.666968	22.0996	14.98	4786	619.80	0.1021	2	0	0
3.300348	31.4507	13.12	4192	553.88	0.1041	2	2	0
2.952517	35.2705	60.45	19320	2947.26	0.1202	3	1	0
2.616307	39.9838	8.53	2726	336.62	0.0973	1	0	1
2.333729	45.0746	3.58	1143	157.83	0.1088	4	0	0
2.282243	46.1495	27.91	8919	1197.33	0.1058	2	1	1
2.200038	47.9798	1.03	329	60.47	0.1449	3	3	0
2.087309	50.7491	11.82	3778	521.38	0.1087	4	2	0
2.050226	51.7341	61.34	19603	2692.77	0.1082	3	0	1
1.876630	56.9327	4.37	1397	297.35	0.1677	3	2	1
1.830753	58.4955	6.99	2234	357.47	0.1261	5	1	0
1.741558	61.8093	20.72	6620	990.96	0.1180	4	1	1
1.650187	65.6465	1.18	379	78.27	0.1629	4	4	0
1.601040	67.9303	1.07	343	47.21	0.1084	5	3	0
1.555782	70.1909	11.06	3534	626.70	0.1397	6	0	0
1.540278	71.0035	1.81	578	152.94	0.2085	5	0	1
1.462669	75.4021	22.66	7241	1176.23	0.1280	5	2	1
1.362797	82.0454	12.91	4125	738.00	0.1410	0	0	2
1.337206	83.9674	3.17	1014	198.47	0.1543	6	1	1
1.334788	84.1543	1.27	405	68.45	0.1332	1	1	2
1.320125	85.3087	0.91	291	53.34	0.1445	7	1	0
1.285502	88.1857	18.06	5771	1111.41	0.1518	5	4	1
1.259606	90.4908	1.18	377	60.59	0.1266	2	2	2
1.237490	92.5756	9.42	3012	843.65	0.2207	3	1	2
1.225715	93.7332	3.11	995	206.82	0.1638	7	3	0
1.176781	98.9477	0.97	310	65.09	0.1653	4	0	2
1.160252	100.8764	0.56	179	42.30	0.1865	7	2	1
1.141129	103.2303	2.70	864	168.35	0.1536	4	2	2
1.100130	108.7939	1.73	554	118.87	0.1690	6	6	0
1.093316	109.7975	1.51	483	145.43	0.2372	5	1	2
1.085145	111.0347	1.42	455	99.51	0.1723	7	5	0
1.065614	114.1548	1.40	446	114.40	0.2019	8	1	1
1.050755	116.7014	0.80	256	57.12	0.1757	4	4	2
1.037795	119.0627	0.76	243	55.12	0.1786	5	3	2

Sample S3600

Peaklist [Range 1 : 2Theta = 10.000 119.990 0.010 I_{max} = 7722]

D	2Theta	I(rel)	I(abs)	I(int)	FWHM	H	K	L
6.593956	15.5926	31.22	2248	313.94	0.1100	1	1	0
4.662950	22.1189	36.72	2645	420.50	0.1253	2	0	0
3.297365	31.4799	21.36	1538	233.85	0.1198	2	2	0
2.949342	35.3097	100.00	7202	1211.02	0.1325	3	1	0
2.615738	39.9929	8.32	599	89.56	0.1178	1	0	1
2.331490	45.1202	4.42	318	58.68	0.1453	4	0	0
2.281218	46.1714	26.84	1933	319.75	0.1304	2	1	1
2.198144	48.0238	1.01	73	11.30	0.1225	3	3	0
2.085382	50.7993	13.01	937	165.90	0.1395	4	2	0
2.049119	51.7642	59.53	4287	799.81	0.1470	3	0	1
1.875871	56.9579	4.01	289	67.03	0.1829	3	2	1
1.829034	58.5559	6.97	502	119.87	0.1881	5	1	0
1.740450	61.8529	19.46	1401	299.71	0.1686	4	1	1
1.648596	65.7178	1.12	81	16.39	0.1599	4	4	0
1.599597	67.9999	0.81	58	13.12	0.1774	5	3	0
1.554393	70.2629	10.73	773	206.09	0.2102	6	0	0
1.539126	71.0647	1.51	109	23.59	0.1704	5	0	1
1.461665	75.4629	21.79	1569	364.83	0.1832	5	2	1
1.362501	82.0671	8.82	635	164.28	0.2038	0	0	2
1.336110	84.0520	2.78	200	57.34	0.2259	6	1	1
1.318970	85.4012	0.84	61	15.16	0.1963	7	1	0
1.307763	86.3107	0.57	41	5.25	0.1005	2	0	2
1.284566	88.2667	15.14	1090	314.06	0.2270	5	4	1
1.259336	90.5156	0.78	56	12.89	0.1809	2	2	2
1.237177	92.6059	7.28	524	187.46	0.2818	3	1	2
1.224641	93.8405	2.59	186	58.23	0.2461	7	3	0
1.196765	96.7342	0.31	22	7.34	0.2593	7	0	1
1.176397	98.9914	0.90	65	18.51	0.2245	4	0	2
1.159129	101.0109	0.50	36	13.70	0.2990	7	2	1
1.140607	103.2965	1.89	136	47.07	0.2725	4	2	2
1.131017	104.5330	0.48	34	9.59	0.2200	8	2	0
1.099098	108.9443	1.45	105	38.35	0.2888	6	6	0
1.092870	109.8641	1.38	99	48.37	0.3832	5	1	2
1.084199	111.1804	1.18	85	30.68	0.2851	7	5	0
1.064805	114.2894	1.11	80	31.73	0.3127	8	1	1
1.050175	116.8041	0.52	37	11.61	0.2463	4	4	2
1.042813	118.1318	0.50	36	11.80	0.2591	8	4	0
1.037123	119.1891	0.33	24	6.60	0.2164	5	3	2

Sample S3439

Peaklist [Range 1 : 2Theta = 9.991 119.891 0.020 I_{max} = 9938]

D	2Theta	I(rel)	I(abs)	I(int)	FWHM	H	K	L
6.588147	15.6065	22.96	1971	284.61	0.1138	1	1	0
4.659926	22.1335	29.08	2497	402.53	0.1271	2	0	0
3.296009	31.4932	20.50	1760	265.80	0.1190	2	2	0
2.948780	35.3166	100.00	8587	1724.17	0.1582	3	1	0
2.614478	40.0130	10.46	898	134.11	0.1177	1	0	1
2.330883	45.1326	5.21	447	83.99	0.1480	4	0	0
2.280457	46.1877	36.29	3116	553.19	0.1399	2	1	1
2.085027	50.8086	16.86	1448	244.52	0.1331	4	2	0
1.875383	56.9741	5.05	434	93.21	0.1693	3	2	1
1.828597	58.5712	7.50	644	175.88	0.2153	5	1	0
1.739956	61.8724	23.06	1980	468.49	0.1864	4	1	1
1.649021	65.6988	1.33	114	45.23	0.3121	4	4	0
1.553880	70.2896	11.04	948	297.59	0.2473	6	0	0
1.538829	71.0805	1.41	121	37.28	0.2419	5	0	1
1.461211	75.4905	23.06	1980	520.96	0.2074	5	2	1
1.361774	82.1203	11.01	946	317.50	0.2645	0	0	2
1.336172	84.0472	2.25	194	40.88	0.1664	6	1	1
1.334021	84.2138	2.20	189	41.25	0.1723	1	1	2
1.284105	88.3066	15.67	1345	459.88	0.2694	5	4	1
1.236552	92.6665	9.45	811	343.72	0.3340	3	1	2
1.224149	93.8898	2.57	221	73.22	0.2611	7	3	0
1.157508	101.2058	1.16	99	153.31	1.2172	3	3	2
1.140226	103.3449	2.14	183	71.18	0.3058	4	2	2
1.098712	109.0007	1.66	142	48.93	0.2707	6	6	0
1.092295	109.9501	1.70	146	63.92	0.3457	5	1	2
1.083809	111.2407	1.20	103	47.56	0.3639	7	5	0
1.042269	118.2317	0.84	72	29.01	0.3178	8	4	0

Sample S3442

Peaklist [Range 1 : 2Theta = 9.965 119.905 0.020 I_{max} = 23268]

D	2Theta	I(rel)	I(abs)	I(int)	FWHM	H	K	L
6.595875	15.5881	20.15	4079	582.19	0.1125	1	1	0
4.662302	22.1220	27.81	5629	922.06	0.1291	2	0	0
3.296379	31.4896	19.87	4023	595.75	0.1167	2	2	0
2.949004	35.3139	100.00	20244	3923.17	0.1527	3	1	0
2.614808	40.0077	10.11	2046	287.68	0.1108	1	0	1
2.330857	45.1332	6.24	1263	223.94	0.1397	4	0	0
2.280563	46.1854	39.65	8027	1307.33	0.1284	2	1	1
2.084759	50.8156	18.42	3730	630.13	0.1331	4	2	0
2.048530	51.7802	90.55	18331	3429.70	0.1474	3	0	1
1.874776	56.9942	5.46	1106	310.67	0.2214	3	2	1
1.828486	58.5751	10.35	2094	524.93	0.1975	5	1	0
1.648293	65.7314	1.82	368	79.89	0.1711	4	4	0
1.598971	68.0302	1.37	277	47.40	0.1349	5	3	0
1.553782	70.2946	15.85	3209	935.97	0.2298	6	0	0
1.539606	71.0392	2.81	568	189.30	0.2626	5	0	1
1.461182	75.4922	35.11	7108	1637.97	0.1816	5	2	1
1.335345	84.1112	4.30	870	284.26	0.2576	1	1	2
1.318436	85.4441	1.39	282	58.67	0.1638	7	1	0
1.284065	88.3101	24.46	4951	1224.68	0.1949	5	4	1
1.224141	93.8905	3.81	772	214.95	0.2195	7	3	0
1.196611	96.7508	0.45	92	24.78	0.2127	7	0	1
1.158692	101.0634	0.75	152	54.31	0.2808	3	3	2
1.130491	104.6019	0.70	142	47.29	0.2618	8	2	0
1.098357	109.0527	2.92	591	247.68	0.3302	6	6	0
1.083719	111.2545	1.96	397	135.21	0.2682	7	5	0
1.064391	114.3584	2.18	442	180.56	0.3219	8	1	1
1.042470	118.1948	0.90	181	55.91	0.2430	8	4	0
1.037122	119.1893	1.01	205	81.16	0.3115	5	3	2

Sample H2216

Peaklist [Range 1 : 2Theta = 9.969 119.949 0.020 Imax = 13267]

D	2Theta	I(rel)	I(abs)	I(int)	FWHM	H	K	L
6.594366	15.5917	19.52	1865	289.24	0.1222	1	1	0
4.661932	22.1238	24.62	2352	488.99	0.1638	2	0	0
3.296359	31.4898	18.53	1771	289.08	0.1286	2	2	0
2.948451	35.3207	96.78	9247	1903.11	0.1622	3	1	0
2.614306	40.0157	10.70	1022	157.80	0.1217	1	0	1
2.330832	45.1337	5.73	548	107.49	0.1547	4	0	0
2.280258	46.1920	44.58	4260	769.90	0.1424	2	1	1
2.197089	48.0483	2.78	265	157.69	0.4683	3	3	0
2.084399	50.8250	20.19	1929	358.01	0.1462	4	2	0
2.048215	51.7887	100.00	9554	2018.29	0.1665	3	0	1
1.874652	56.9983	6.51	622	134.27	0.1701	3	2	1
1.827949	58.5940	10.98	1049	300.81	0.2259	5	1	0
1.739557	61.8882	34.64	3310	774.10	0.1843	4	1	1
1.553469	70.3109	18.62	1779	494.05	0.2188	6	0	0
1.460885	75.5102	39.47	3771	993.15	0.2076	5	2	1
1.361658	82.1288	20.44	1953	497.54	0.2008	0	0	2
1.335012	84.1369	3.83	365	102.44	0.2209	6	1	1
1.283845	88.3291	31.66	3025	914.40	0.2382	5	4	1
1.236294	92.6916	15.80	1509	517.95	0.2704	3	1	2
1.223995	93.9052	4.20	401	65.17	0.1280	7	3	0
1.098542	109.0256	3.04	290	108.96	0.2959	6	6	0
1.091841	110.0181	1.04	100	35.20	0.2783	5	1	2
1.063923	114.4366	2.06	197	25.93	0.1039	8	1	1
1.041764	118.3246	2.17	207	231.62	0.8798	8	4	0

Sample H2229

Peaklist [Range 1 : 2Theta = 9.947 119.867 0.020 Imax = 4737]

D	2Theta	I(rel)	I(abs)	I(int)	FWHM	H	K	L
6.589729	15.6027	19.93	747	133.06	0.1405	1	1	0
4.658242	22.1416	22.52	844	191.02	0.1784	2	0	0
3.293584	31.5170	16.42	615	122.61	0.1571	2	2	0
2.946166	35.3490	82.48	3090	773.83	0.1974	3	1	0
2.613005	40.0365	8.90	333	54.68	0.1293	1	0	1
2.328887	45.1735	6.60	247	74.15	0.2364	4	0	0
2.278842	46.2223	44.11	1652	379.72	0.1811	2	1	1
2.194762	48.1025	1.52	57	6.81	0.0941	3	3	0
2.082878	50.8647	18.90	708	169.33	0.1884	4	2	0
2.046807	51.8270	100.00	3746	1068.08	0.2247	3	0	1
1.873749	57.0283	7.67	287	71.04	0.1949	3	2	1
1.826401	58.6485	10.86	407	186.97	0.3623	5	1	0
1.738419	61.9332	36.49	1367	449.18	0.2590	4	1	1
1.646044	65.8326	1.76	66	23.64	0.2828	4	4	0
1.597207	68.1156	1.46	55	10.14	0.1458	5	3	0
1.552628	70.3546	17.33	649	306.16	0.3717	6	0	0
1.537821	71.1342	3.97	149	130.76	0.6924	5	0	1
1.459908	75.5696	46.04	1725	568.40	0.2597	5	2	1
1.360952	82.1806	24.31	910	330.29	0.2859	0	0	2
1.334144	84.2043	5.86	219	74.02	0.2659	6	1	1
1.316589	85.5926	1.32	49	25.40	0.4052	7	1	0
1.283096	88.3941	36.01	1349	672.99	0.3931	5	4	1
1.258115	90.6279	2.83	106	12.66	0.0942	2	2	2
1.235792	92.7404	21.21	795	323.11	0.3204	3	1	2
1.222951	94.0100	4.29	161	68.31	0.3347	7	3	0

Sample S3524:

Peaklist [Range 1 : 2Theta = 9.872 119.832 0.020 Imax = 9084]

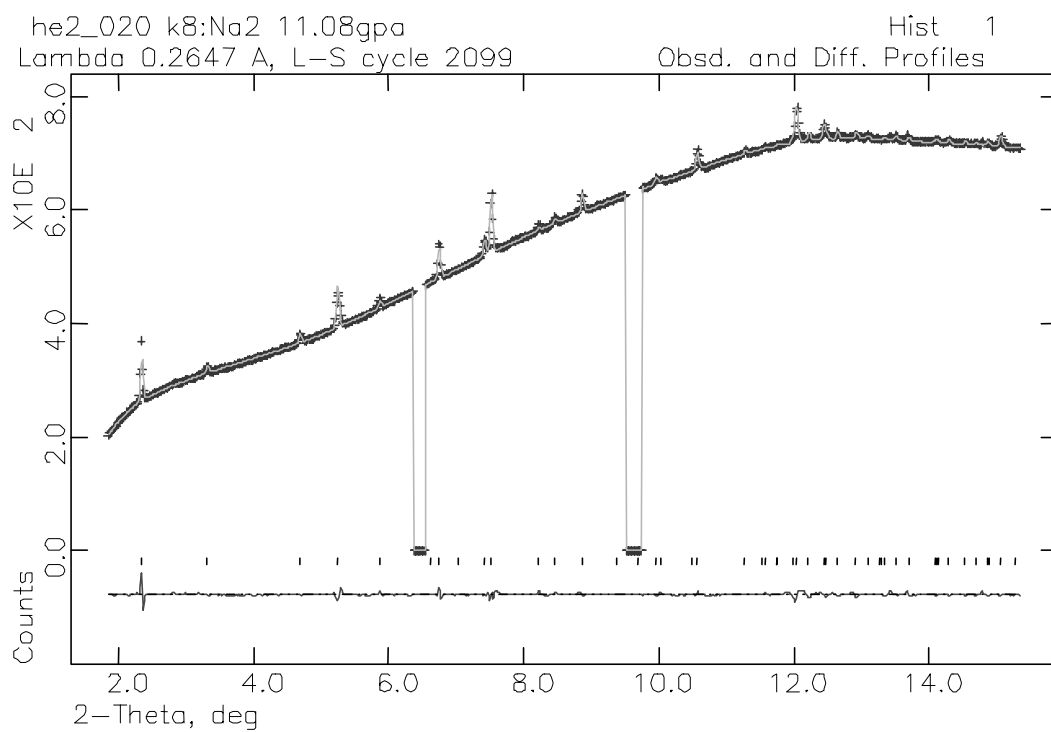
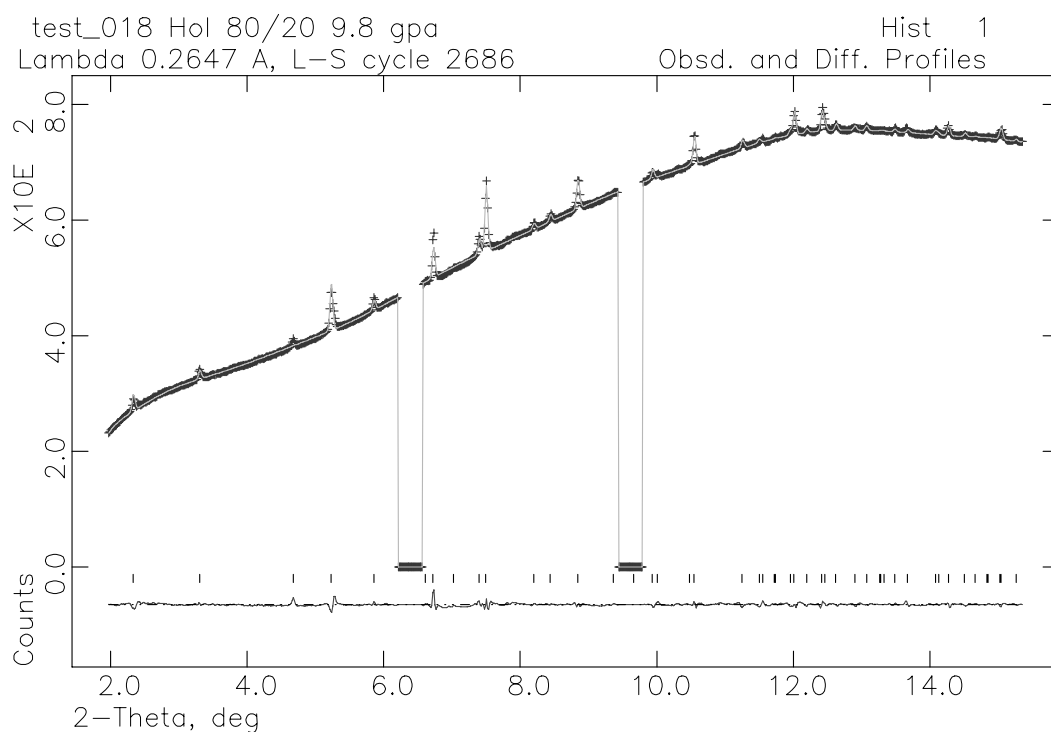
D	2Theta	I(rel)	I(abs)	I(int)	FWHM	H	K	L
4.662851	22.1194	29.34	2328	360.25	0.1219	2	0	0
3.292746	31.5252	18.91	1501	200.10	0.1051	2	2	0
2.944312	35.3720	100.00	7935	1155.72	0.1148	3	1	0
2.611465	40.0611	13.07	1037	128.82	0.0978	1	0	1
2.327391	45.2041	7.01	556	80.82	0.1146	4	0	0
2.277540	46.2503	44.14	3503	517.25	0.1164	2	1	1
2.082051	50.8864	15.78	1252	192.43	0.1211	4	2	0
2.045940	51.8506	91.42	7254	1232.40	0.1339	3	0	1
1.872299	57.0765	5.07	402	88.00	0.1725	3	2	1
1.826195	58.6557	7.55	599	125.69	0.1652	5	1	0
1.738005	61.9495	23.40	1857	333.26	0.1414	4	1	1
1.646503	65.8120	0.98	78	12.57	0.1272	4	4	0
1.597237	68.1142	0.47	37	3.37	0.0716	5	3	0
1.552150	70.3795	9.15	726	178.76	0.1940	6	0	0
1.537417	71.1557	1.53	121	22.96	0.1494	5	0	1
1.459815	75.5753	17.49	1388	295.90	0.1680	5	2	1
1.360993	82.1776	13.08	1038	244.11	0.1853	0	0	2
1.334090	84.2085	2.68	213	42.60	0.1576	6	1	1
1.317253	85.5391	0.54	43	6.79	0.1245	7	1	0
1.306439	86.4197	0.57	45	5.07	0.0889	2	0	2
1.282941	88.4075	11.88	943	236.38	0.1976	5	4	1
1.257927	90.6452	0.69	55	8.82	0.1266	2	2	2
1.235607	92.7584	6.92	549	164.06	0.2355	3	1	2
1.223057	93.9993	1.40	111	28.44	0.2022	7	3	0
1.174932	99.1588	0.73	58	19.15	0.2588	4	0	2
1.139163	103.4803	1.19	95	22.65	0.1887	4	2	2
1.097317	109.2052	0.70	55	20.12	0.2862	6	6	0
1.091257	110.1057	0.86	69	33.42	0.3839	5	1	2
1.082318	111.4717	0.57	45	34.42	0.6024	7	5	0

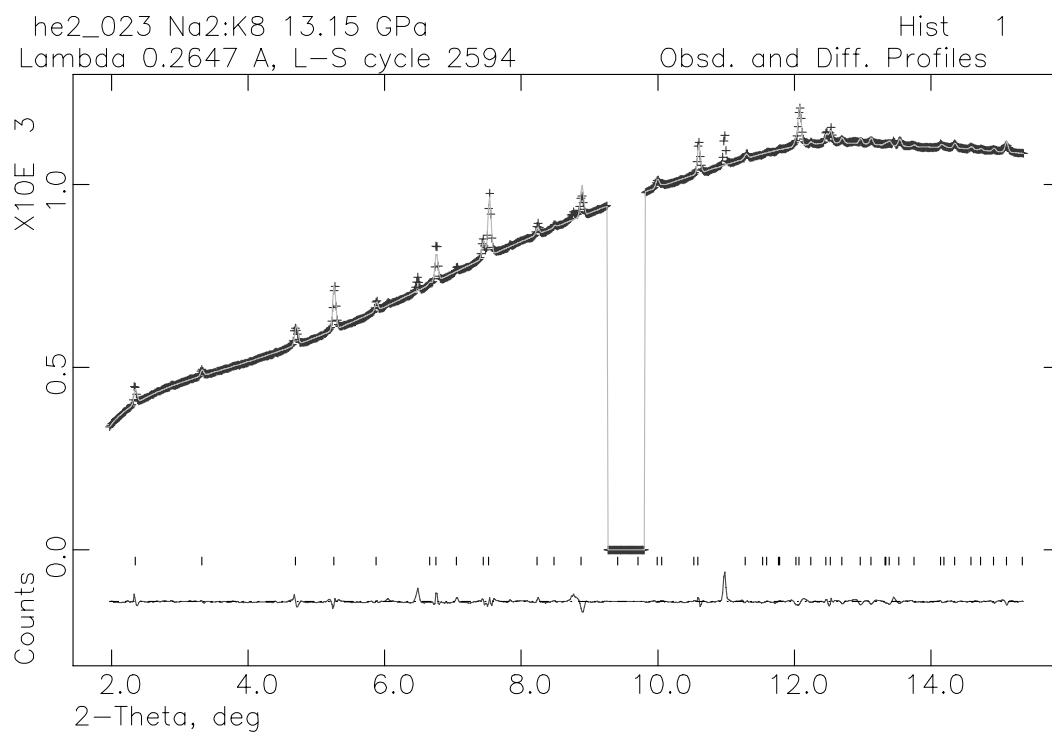
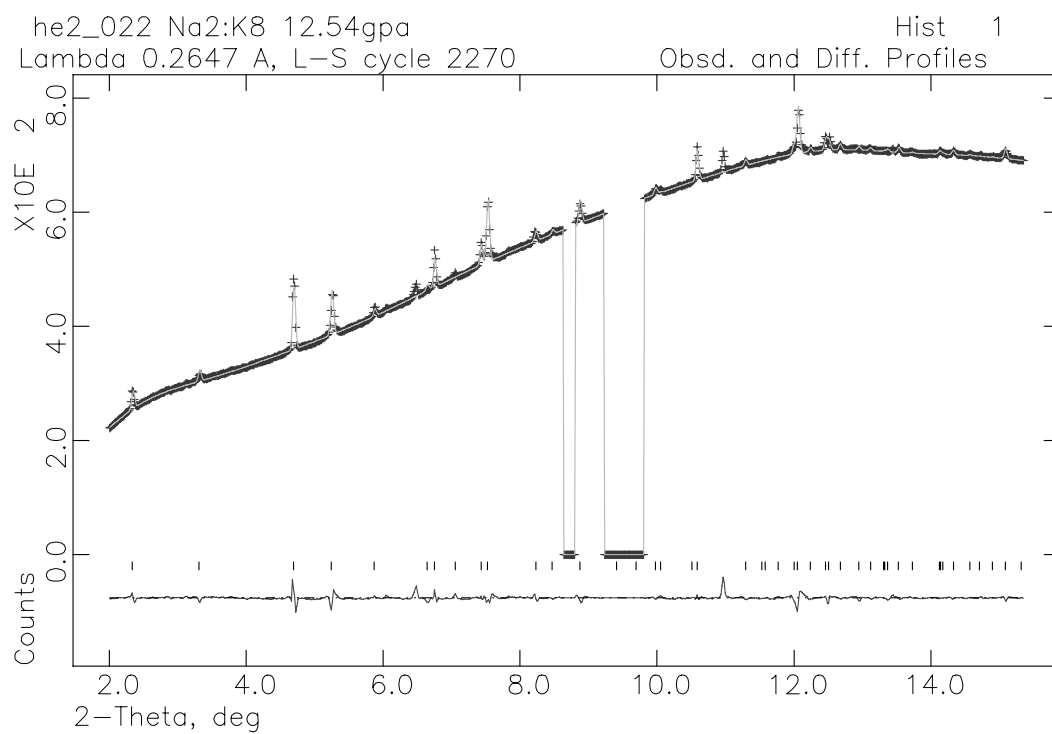
Sample H2305:

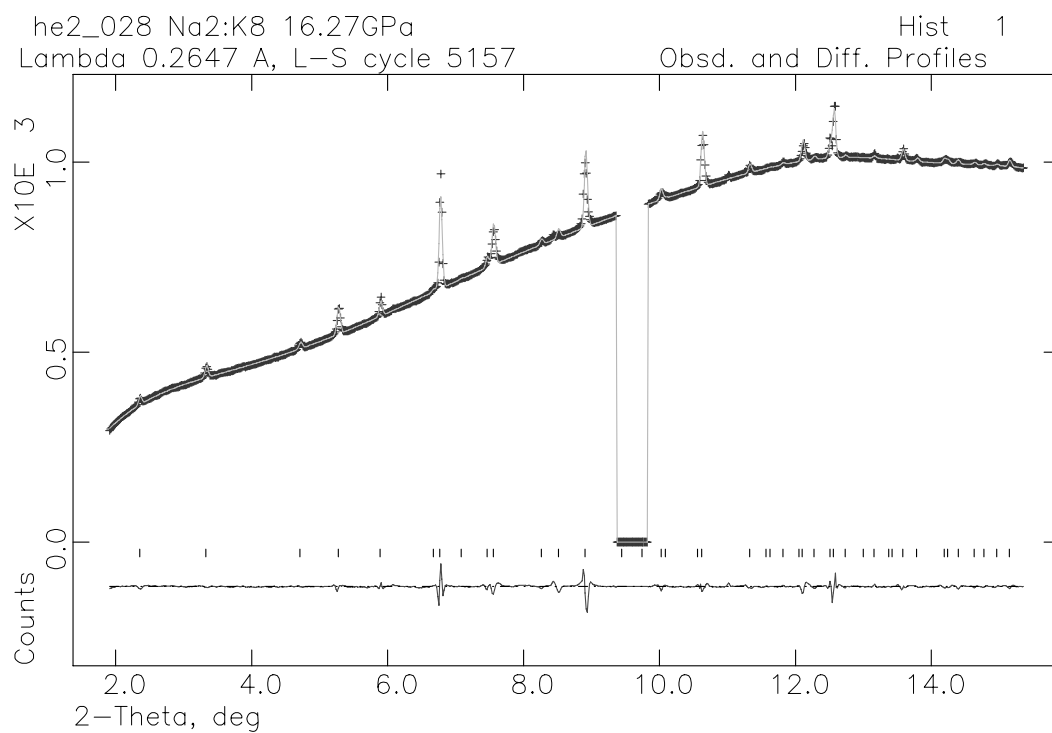
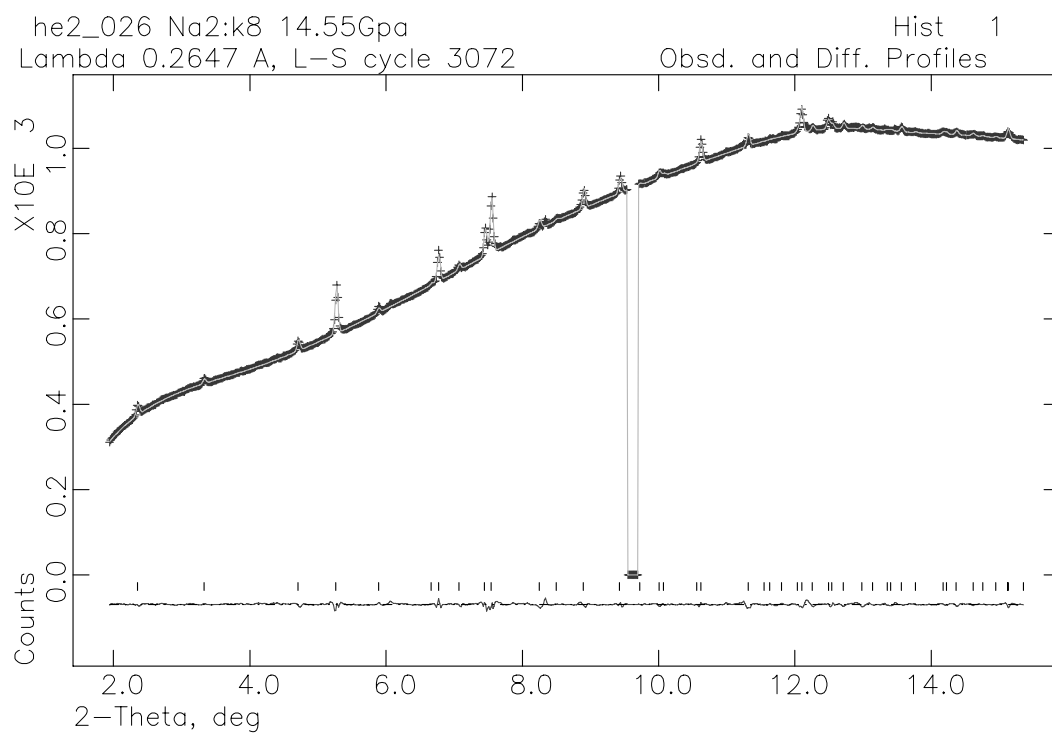
Peaklist [Range 1 : 2Theta = 9.993 119.893 0.010 I_{max} = 8061]

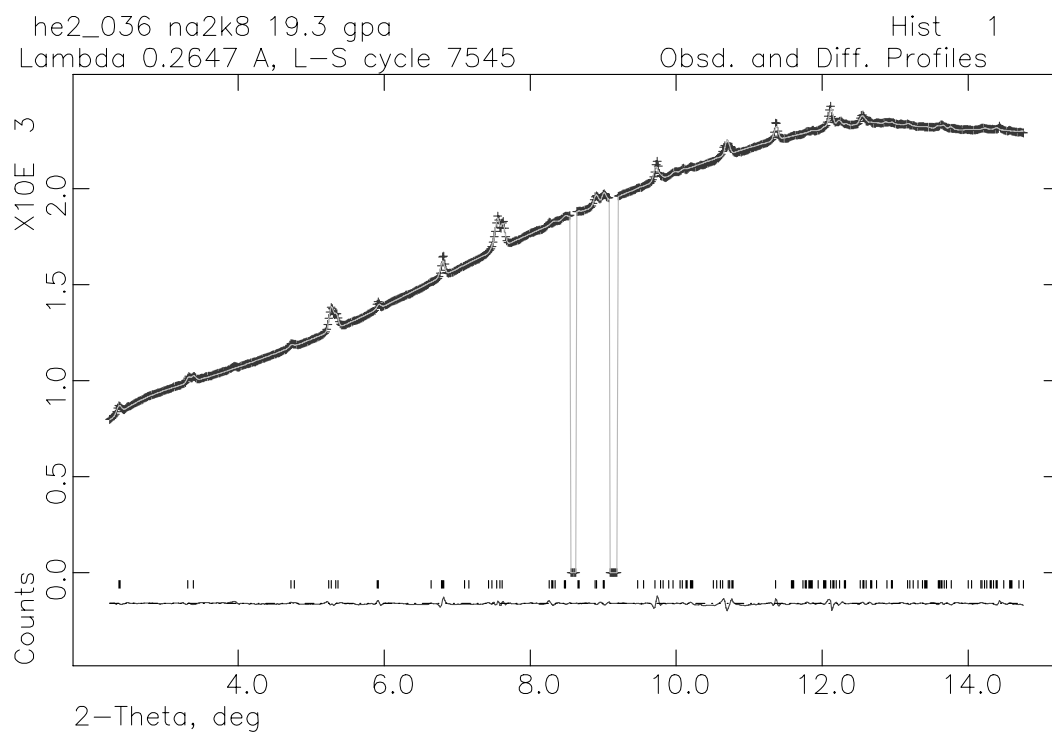
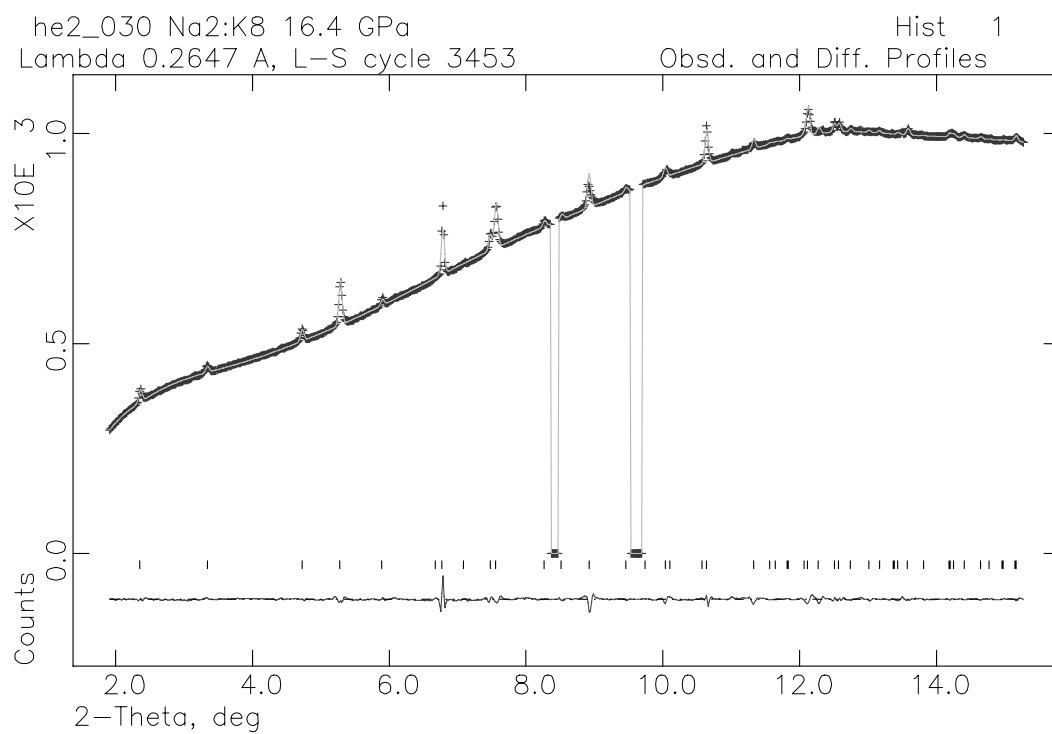
D	2Theta	I(rel)	I(abs)	I(int)	FWHM	H	K	L
6.572488	15.6439	43.34	2963	557.69	0.1483	1	1	0
4.647857	22.1917	42.27	2890	563.05	0.1536	2	0	0
3.287120	31.5806	14.94	1021	208.32	0.1607	2	2	0
2.940046	35.4250	100.00	6836	1287.19	0.1484	3	1	0
2.609982	40.0849	7.03	481	91.53	0.1500	1	0	1
2.324410	45.2653	7.88	539	124.45	0.1820	4	0	0
2.275775	46.2882	36.55	2499	490.91	0.1548	2	1	1
2.079194	50.9613	14.46	988	214.22	0.1708	4	2	0
2.044135	51.8998	82.26	5624	1246.60	0.1747	3	0	1
1.870816	57.1259	4.72	322	68.12	0.1665	3	2	1
1.823582	58.7480	8.55	584	161.68	0.2180	5	1	0
1.735920	62.0322	24.99	1709	416.02	0.1919	4	1	1
1.594500	68.2472	0.79	54	11.64	0.1703	5	3	0
1.549732	70.5056	10.25	701	237.32	0.2669	6	0	0
1.535532	71.2564	1.57	107	69.21	0.5077	5	0	1
1.457675	75.7058	21.41	1464	435.80	0.2346	5	2	1
1.359462	82.2902	12.33	843	263.25	0.2461	0	0	2
1.332482	84.3335	2.86	196	65.45	0.2636	6	1	1
1.314896	85.7293	1.07	73	20.45	0.2211	7	1	0
1.304972	86.5407	0.74	51	14.32	0.2231	2	0	2
1.280851	88.5895	15.98	1092	327.32	0.2361	5	4	1
1.234264	92.8893	8.41	575	196.11	0.2688	3	1	2
1.220778	94.2290	1.87	128	43.16	0.2660	7	3	0
1.155356	101.4660	1.91	130	209.91	1.2681	3	3	2
1.137799	103.6546	1.63	111	45.63	0.3234	4	2	2
1.096105	109.3837	1.12	77	46.19	0.4756	6	6	0
1.089934	110.3050	1.59	109	48.17	0.3483	5	1	2
1.080648	111.7321	1.16	79	30.00	0.2986	7	5	0
1.061954	114.7673	0.84	57	49.15	0.6746	8	1	1

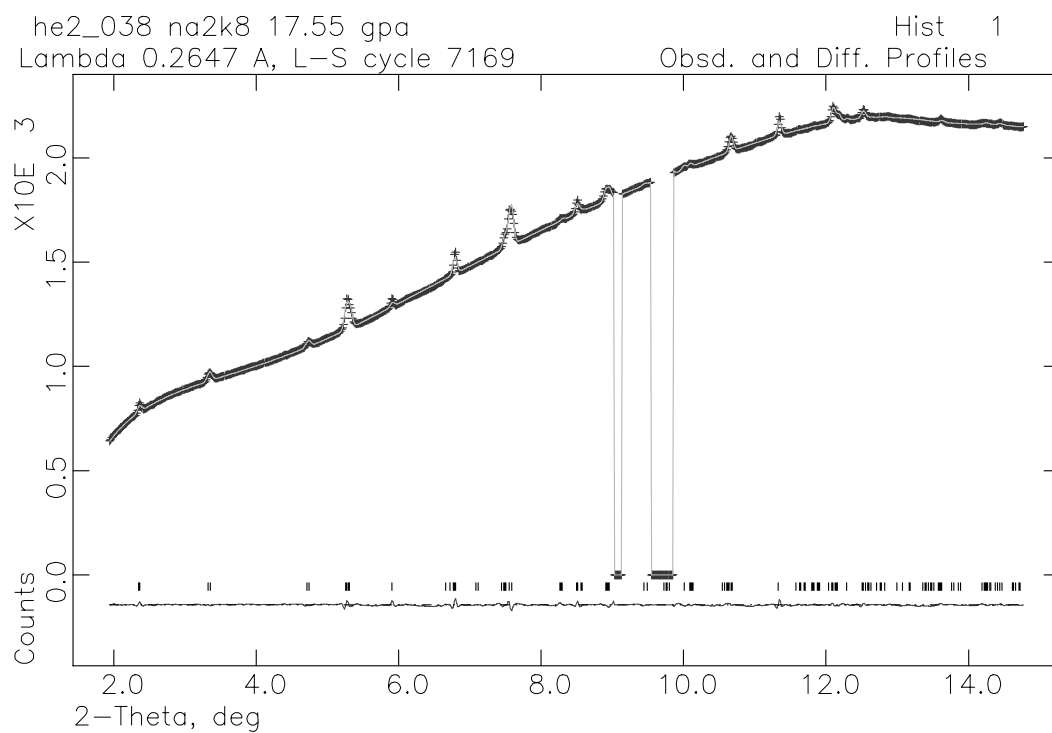
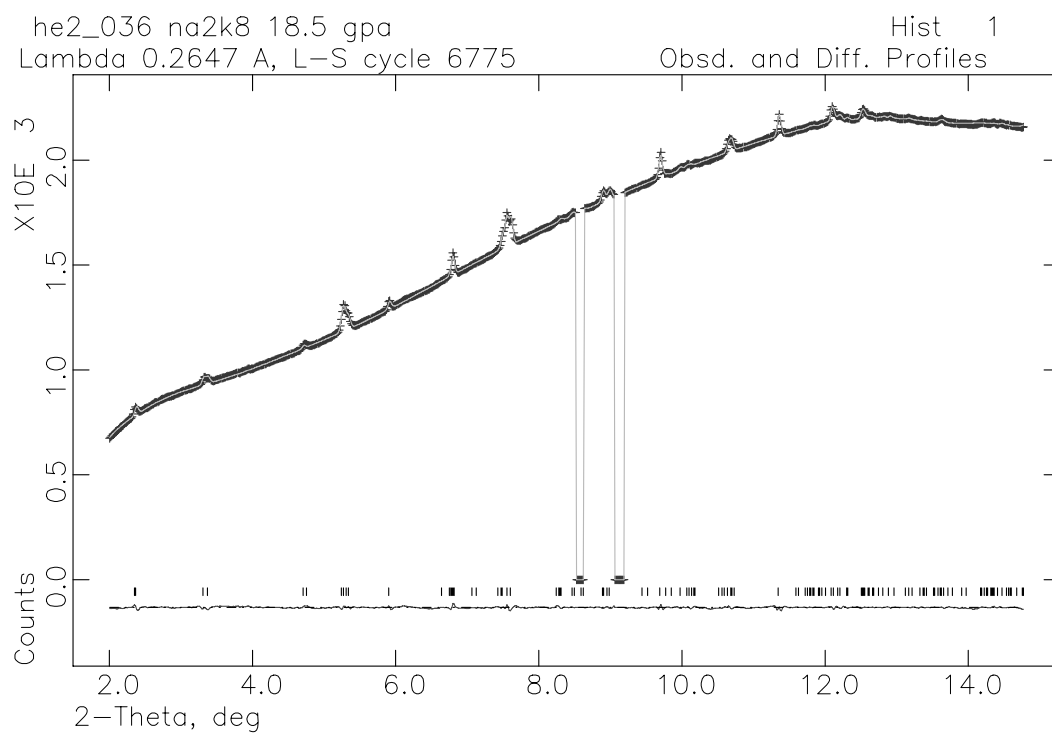
Appendix 2: Rietveld Refinement Patterns from high pressure experiment of $\text{K}_{0.8}\text{Na}_{0.2}\text{AlSi}_3\text{O}_8$ hollandite in helium

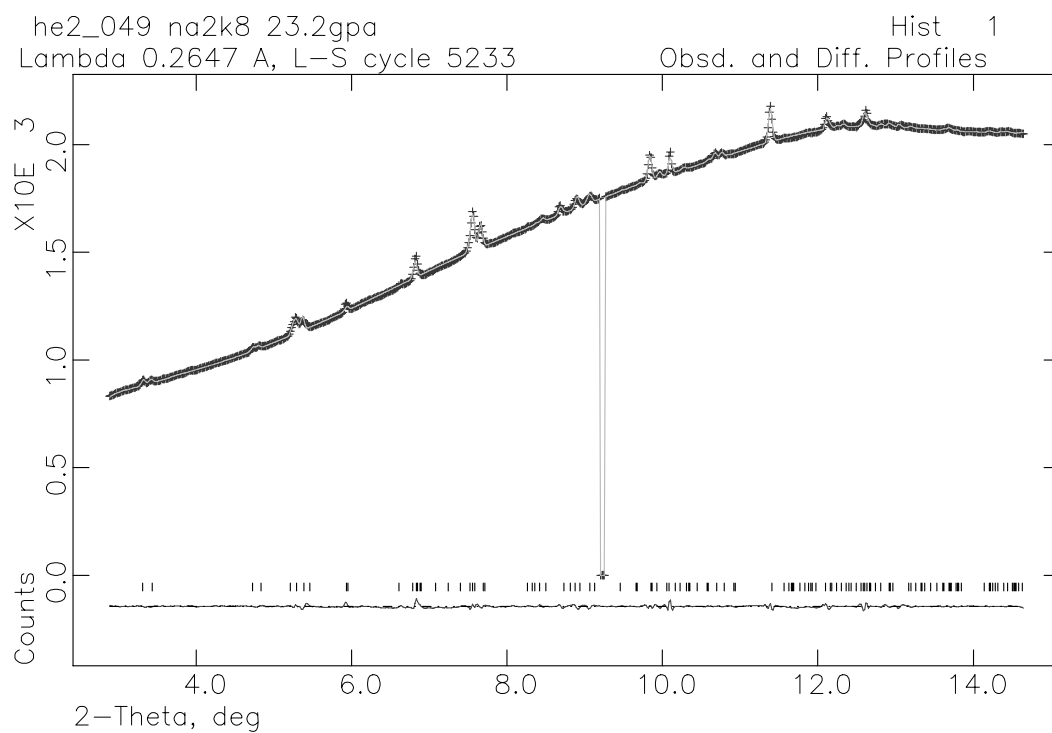
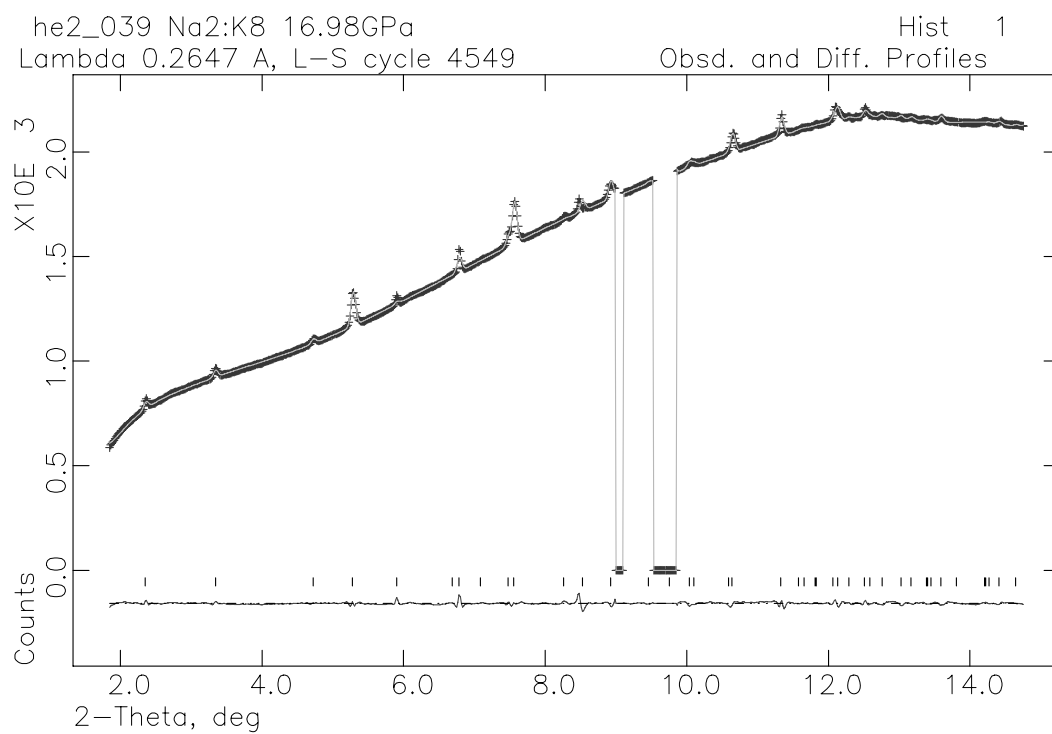


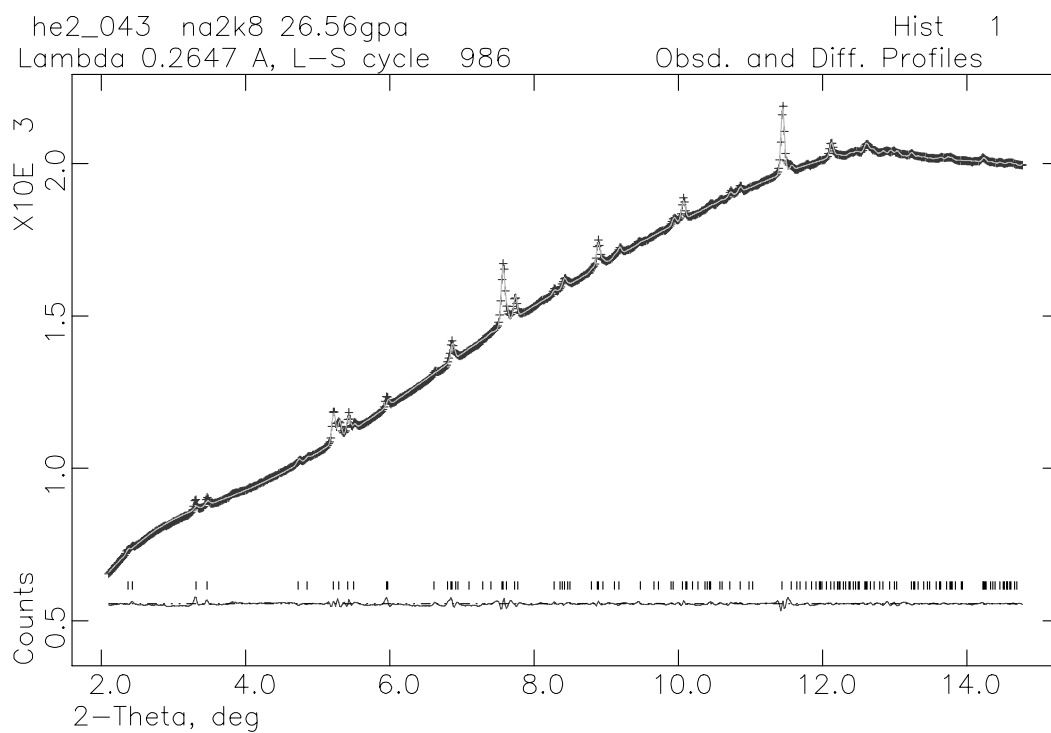
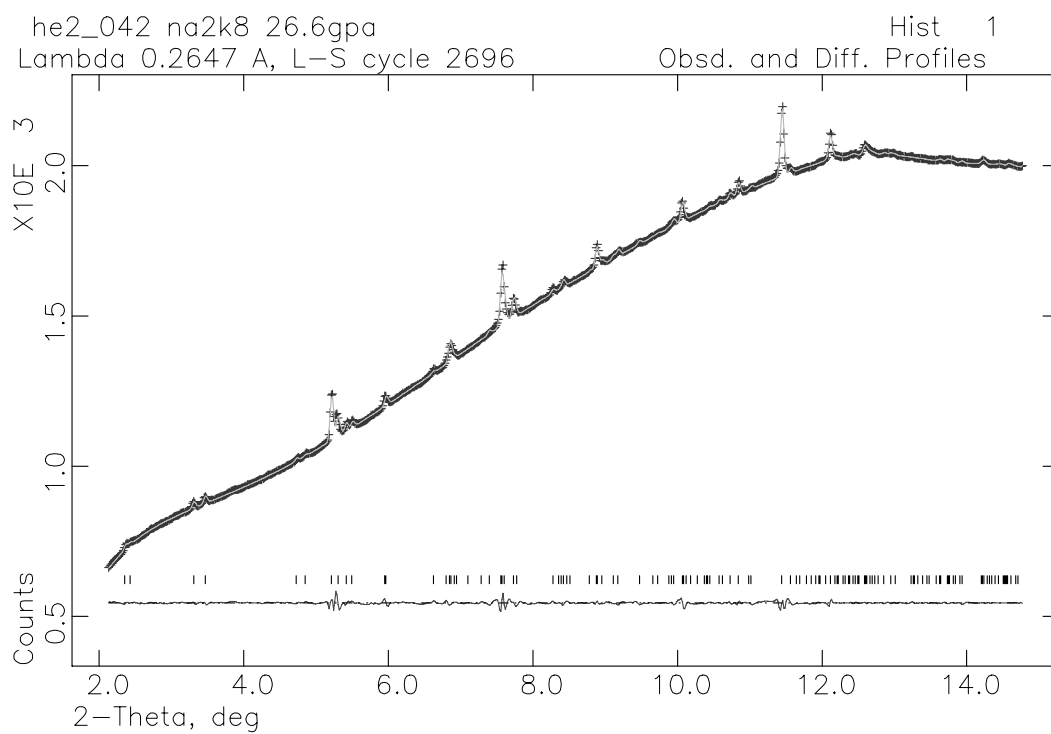


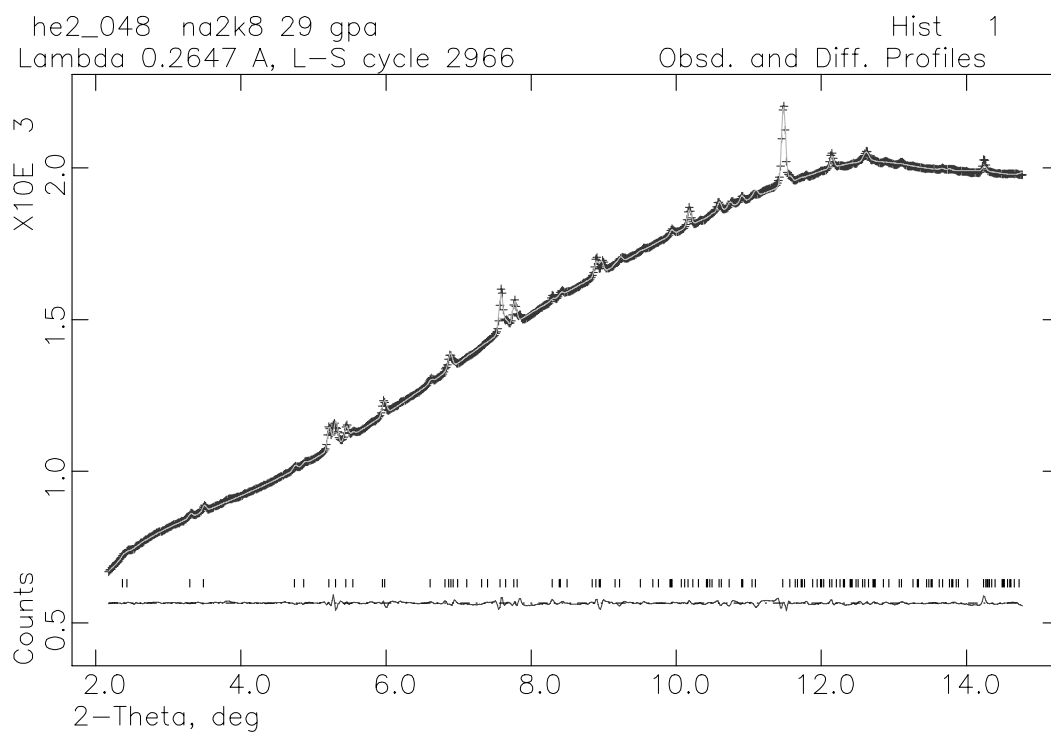
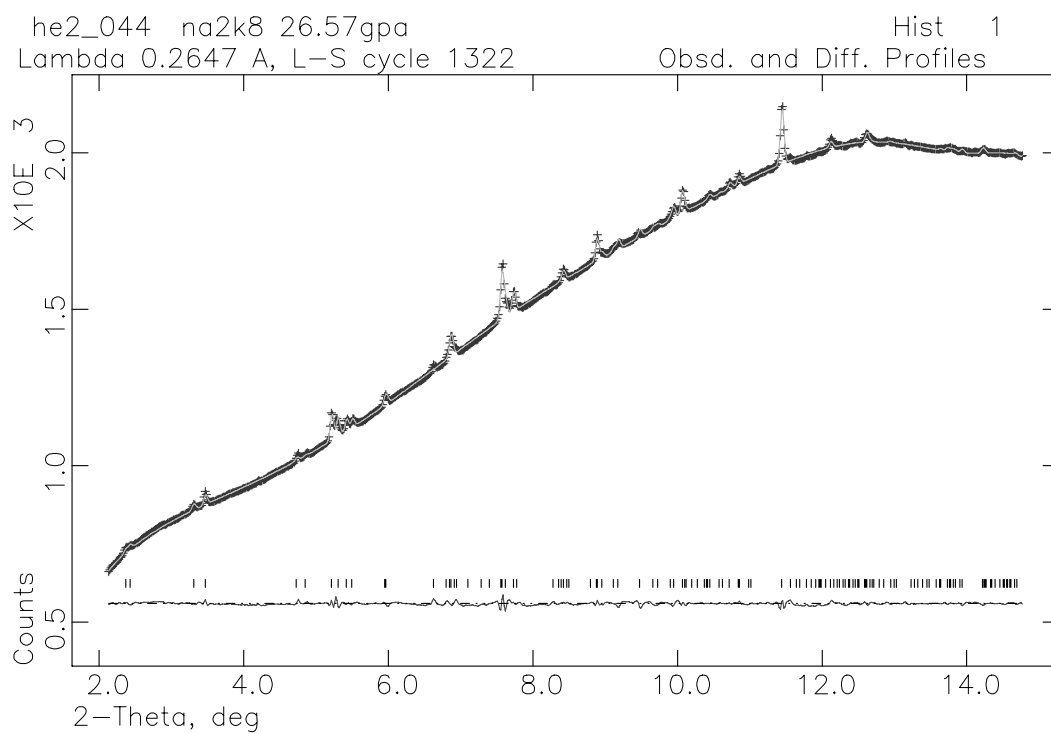


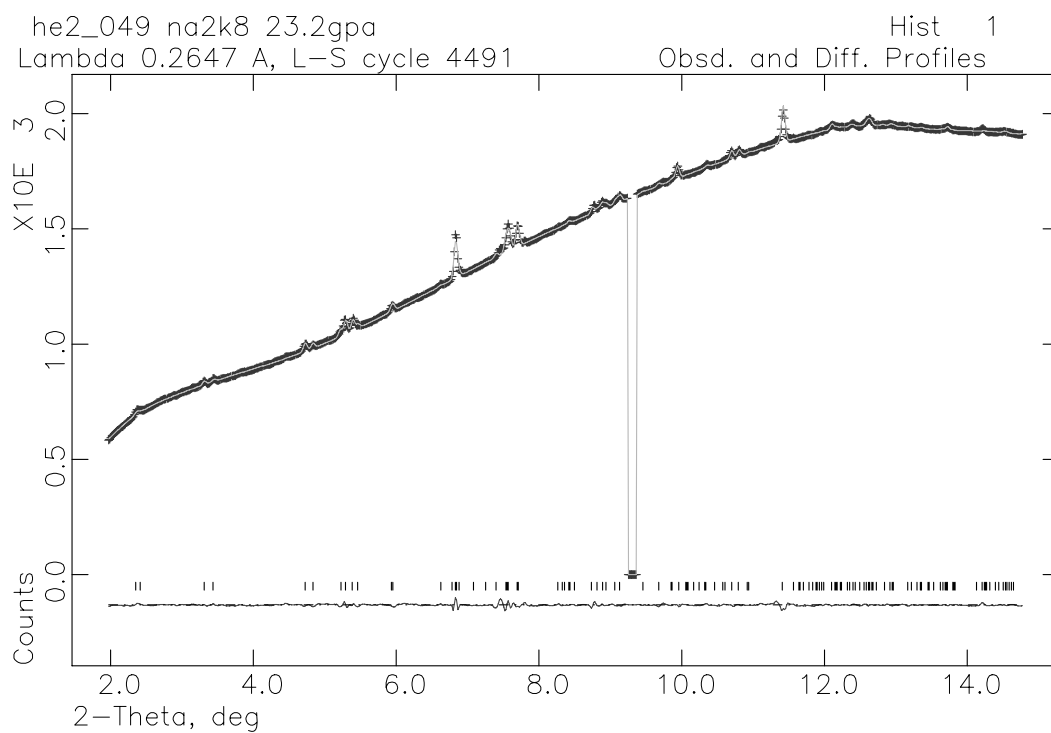
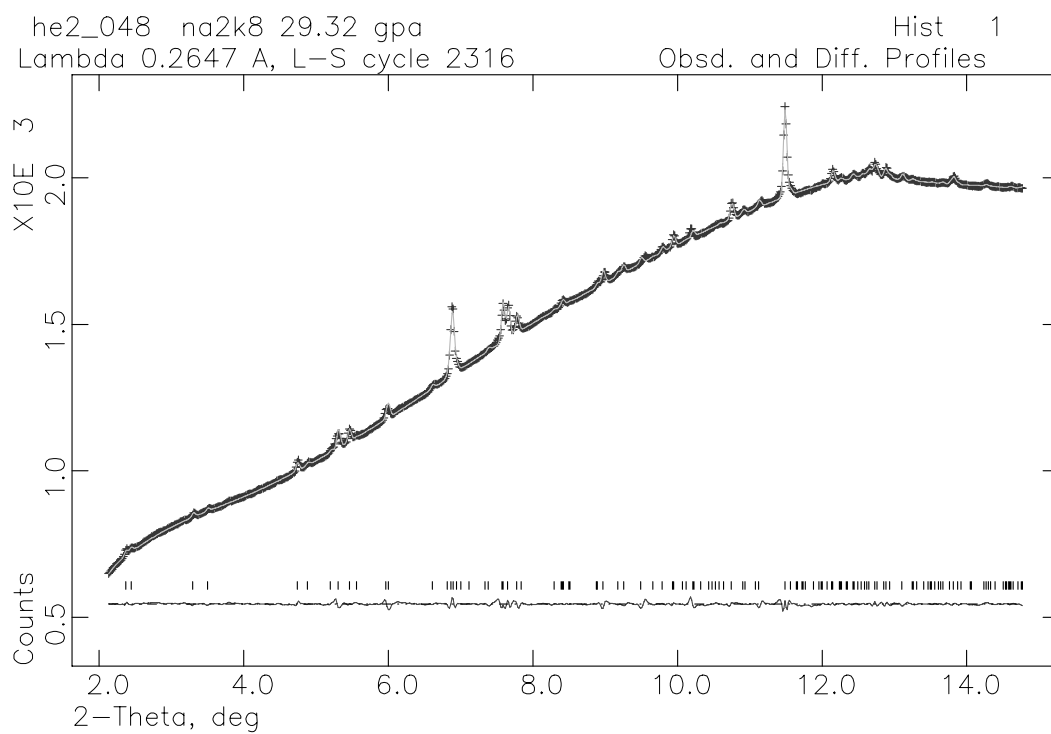


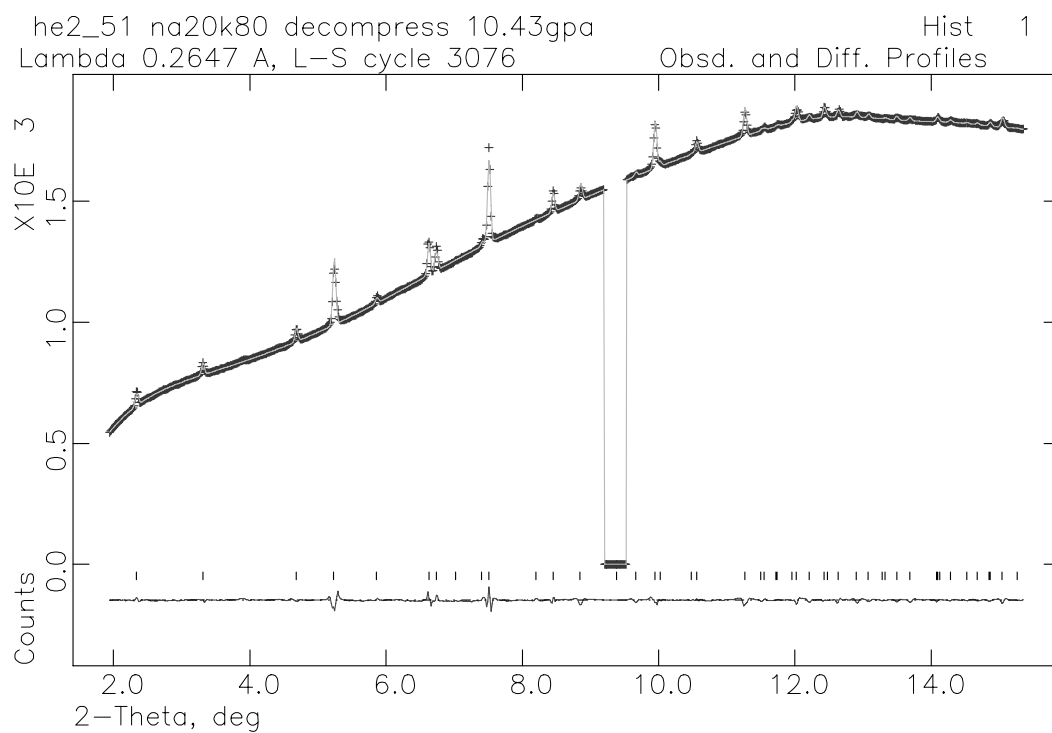
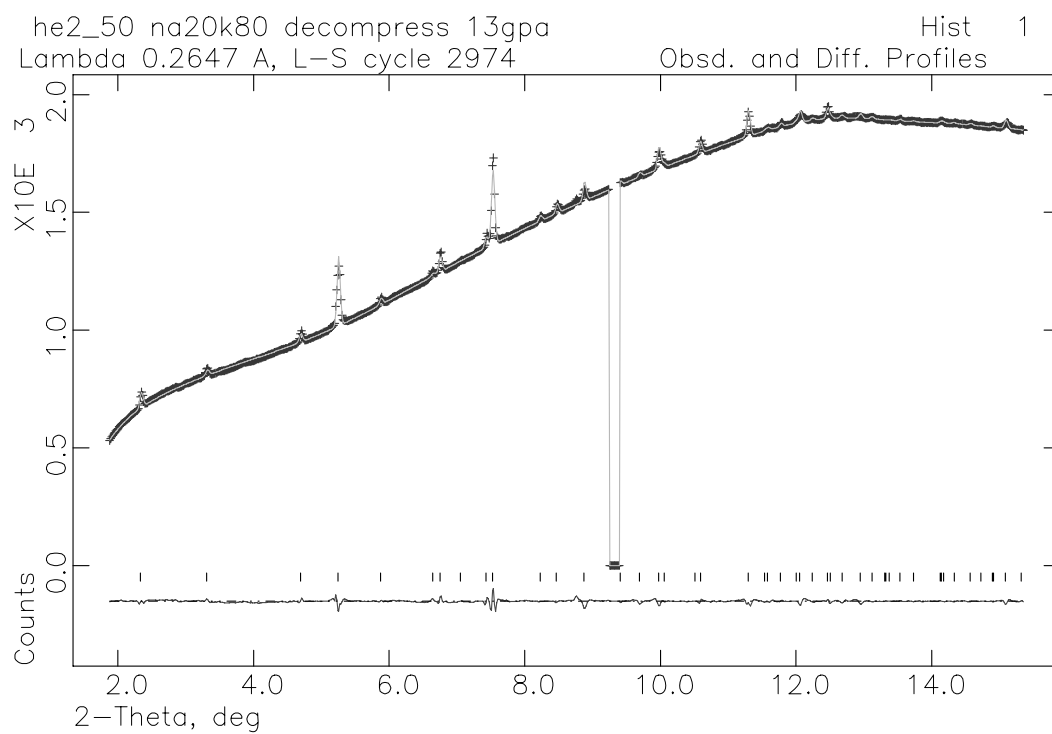


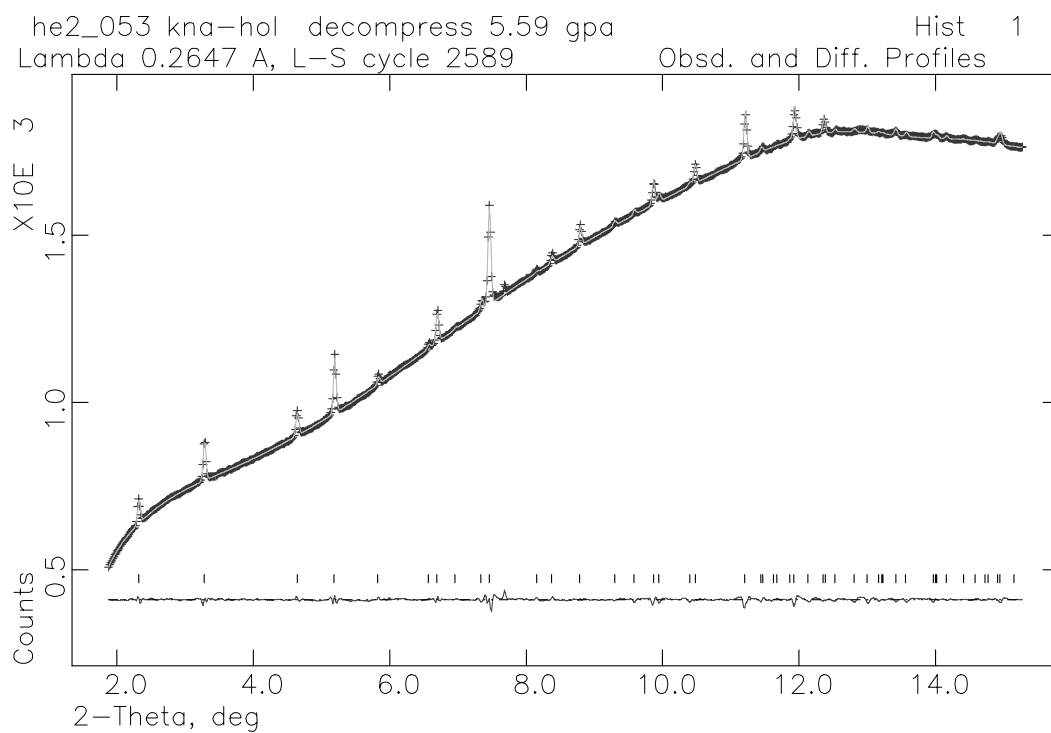
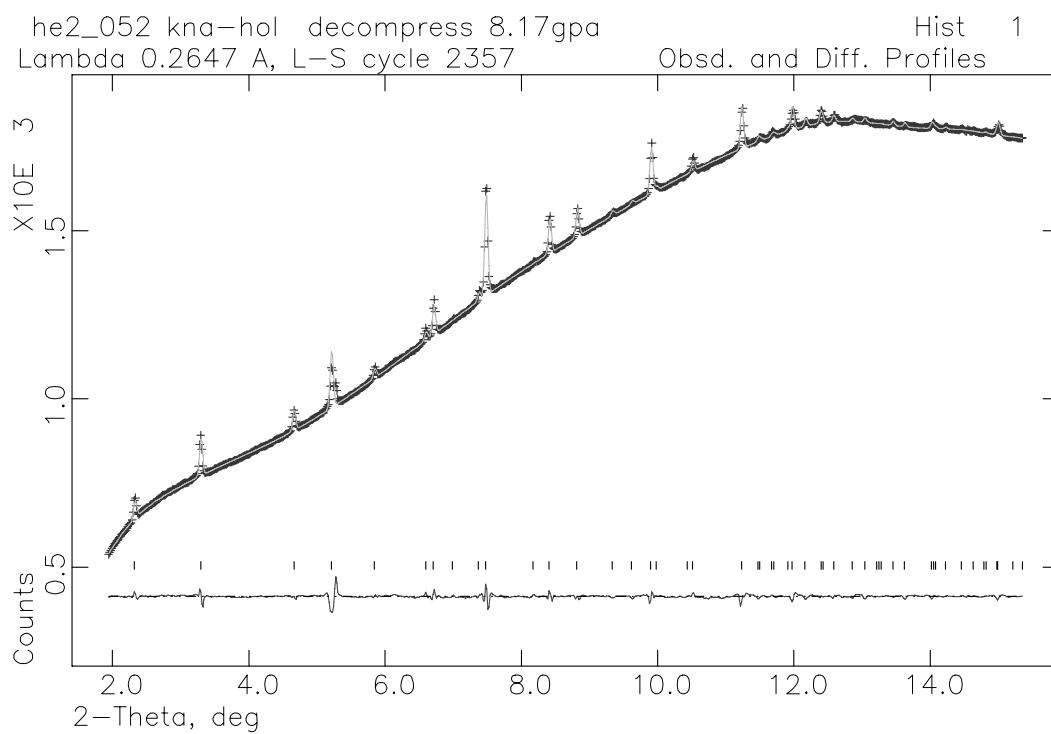


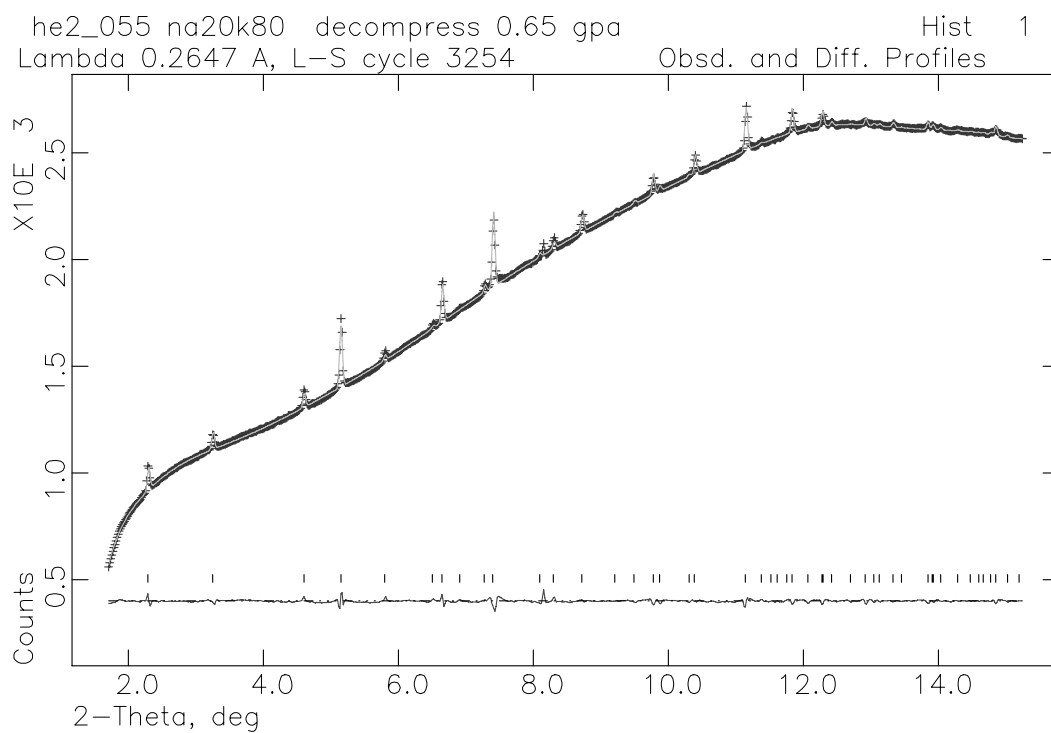
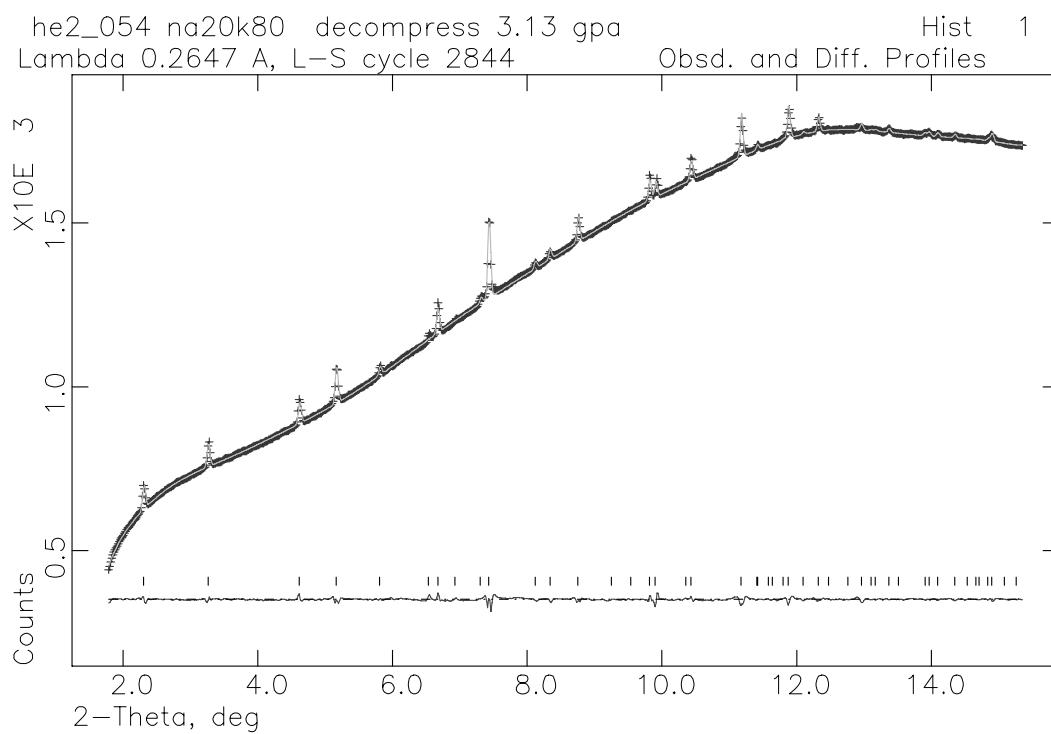












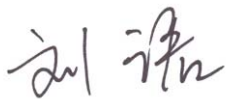
Erklärung

Hiermit erkläre ich, daß ich die vorliegende Arbeit selbständig verfaßt und keine anderen als die von mir angegebenen Quellen und Hilfsmittel benutzt habe.

Ferner erkläre ich, daß ich nicht anderweitig mit oder ohne Erfolg versucht habe, eine Dissertation einzureichen. Ich habe keine gleichartige Doktorprüfung an einer anderen Hochschule endgültig nicht bestanden.

Bayreuth, den 14 May, 2007

Jun Liu

A handwritten signature in black ink, appearing to be 'Jun Liu' in a stylized cursive script.